DEVELOPMENT AND APPLICATIONS OF REAL-SPACE

ELECTROSTATIC INTERACTION METHODS FOR

CHARGE-MULTIPOLES IN CONDENSED PHASE ENVIRONMENTS

A Dissertation

Submitted to the Graduate School

of the University of Notre Dame

in Partial Fulfillment of the Requirements

for the Degree of

Doctor of Philosophy

by

Madan Lamichhane,

_____

Kathie E. Newman, Director

_____

J. Daniel Gezelter, Director

Graduate Program in Physics

Notre Dame, Indiana

March 2016

DEVELOPMENT AND APPLICATIONS OF REAL-SPACE ELECTROSTATIC INTERACTION METHODS FOR CHARGE-MULTIPOLES IN CONDENSED PHASE ENVIRONMENTS

Abstract

by

Madan Lamichhane

$$a = a + b$$

CONTENTS

TABLES

CHAPTER 1

INTRODUCTION

In computer simulation of condensed phase molecular systems, molecules are commonly represented by atomic sites that interact via a parametrized force field. This force field aims to reproduce observable phenomena by incorporating the proper physics into the simulation. There are mainly two types of interaction; intramolecular and intermolecular which determines the static and dynamic properties of the molecular systems. An intramolecular interaction is the interaction within a single molecule including, bonding, bending, and torsional motion whereas an intermolecular interaction is the interaction between two or more molecules and includes van der Waals and electrostatic interactions. The computation of the electrostatic interaction is the most expensive portion of a molecular simulations. Due to this, there have been significant efforts to develop practical, efficient, and accurate methods for electrostatic interactions.

The Ewald method is one of the most well known and accurate methods but is computationally expensive, scaling as $O(N^2)$, where N is the total number of particles. The appropriate selection of a damping parameter and suitable algorithm can decrease computational cost to $O(N^{3/2})$.[67] Modified Ewald methods, using a particle mesh and fast Fourier transform (FFT), have decreased the cost to $O(N \log N)$. [15, 22, 53, 79] But these modified Ewald methods (particle mesh Ewald (PME) and particle-particle particle-mesh Ewald (PPPME)) are still com-

putationally expensive. In addition to this, the Ewald method requires an inherent periodicity which can be problematic in a number of protein/solvent and ionic solution environments. [23, 33, 34, 51, 72, 73, 92] To address these problems there is growing interest in the development of efficient real space electrostatic methods which scale linearly with the system size, O(N). Real space methods were originally proposed by Wolf *et al.* [95] and extended initially by Zahn *et al.*[18] then by Fennell and Gezelter. [23] These methods were only limited to charge-charge interactions between atomic sites. My research developed real-space electrostatic interaction methods for higher order multipoles (dipoles and quadrupoles) and implemented these methods as code into OpenMD, [28] an open source C++-based software. We also studied applications and performance of these methods in the various condensed phase environments. In addition our research also evaluated various static, dynamic, and dielectric properties for different molecular systems, using newly developed real space methods and compared our results with the well-known Ewald method.

This dissertation consists of five chapters. This introductory chapter initially outlines the background and motivation of the research. It also briefly discusses the basic principles of widely used molecular simulation methods: Molecular Dynamics (MD) and Monte Carlo (MC) simulations, where newly developed electrostatic methods are very useful. Similarly, this chapter describes periodic boundary conditions (PBC) and spherical truncation which are both widely incorporated in molecular simulations for computational efficiency. Additionally it also discusses the traditional Ewald as well as various modified Ewald-based methods, PPPME and PME. Finally it discusses the problems created due to the direct spherical truncation in real-space methods and presents various techniques implemented to

resolve these problems.

Chapter 2 presents the mathematical formulation of our newly developed real-space electrostatic methods: Gradient Shifted Force (GSF), Shifted Potential (SP), and Taylor Shifted force (TSF). The energy constants for different dipolar and quadrupolar crystals were evaluated using newly developed real-space methods and compared with analytical results.

The accuracy of the newly developed methods tested against Ewald in Chapter 3. Furthermore various static and dynamic properties evaluated from real space methods are also compared with traditional Ewald method. The study of total energy conservation, which is very important in MD simulations, is also presented in this chapter.

Chapter 4 describes Fluctuation, Perturbation, and Potential of Mean Force (PMF) methods for evaluating dielectric properties for dipolar and quadrupolar fluids. This chapter also explores the correction factor required to obtain actual dielectric properties using SP, GSF, and TSF methods. In addition, the dielectric properties such as susceptibility and dielectric constant, obtained using all three methods are compared with each other as well as with previous simulations.

Finally Chapter 5 summarizes, draws conclusions and discusses future directions and limitations of this research.

1.1   Molecular Dynamics (MD) Simulations

Molecular dynamics is a computer simulation method for studying static and dynamic properties of molecular systems. In this method, each atom or molecule interacts with all other molecules in the system and evolves dynamically following classical equation of motion. The numerical step-by-step process for MD is

outlined in figure 1.1.

In a MD simulation, all molecules are initialized by assigning their initial positions and velocities using appropriate boundary conditions. Molecules are usually initialized in such a way so that system does not take too long time to reach equilibrium. Before moving a molecule in the system, the computer must evaluate force and the potential energy contributed by intramolecular interactions as well as intermolecular interactions. The potential energy of the molecule in the system can be written as:

$$U(\mathbf{r}) = \overbrace{U_{bond} + U_{bend} + U_{torsion}}^{Intramolecular\ interactions} + \overbrace{U_{electrostatic} + U_{van\ der\ Waals}}^{Intermolecular\ interactions} + ... \qquad (1.1)$$

The force and torque acting on the molecule can be calculated using following equations:

$$\mathbf{F} = \nabla_r U(\mathbf{r}, \hat{u}) \qquad (1.2a)$$

$$\tau = \mathbf{r} \times \nabla_r U(\mathbf{r}, \hat{u}), \qquad (1.2b)$$

where $\hat{u}$ is the orientation of the molecule and the evaluation of force and torque depends on the direction of orientation for the point multipoles. The force and torque are required to propagate the dynamics to the molecule at a given time step. The same process can be repeated for every molecule in the system. Once every molecule in the system is moved forward a time-step, their positions and velocities are adjusted according to applied boundary conditions (i.e temperature, pressure, volume, etc are adjusted). After adjusting positions and velocities, we can recalculate the potential energy for each molecule and repeat same process

Initilization

$At: i = 0$

Give initial positions and *velocities*: r^i, v^i, θ^i, and w^i

Set accelerations and *time*: $a = 0$, $\alpha = 0$, and $t = 0$

Choose: Δt

Prediction

Move atoms: $r^p = r^i + v^i \Delta t + \dfrac{1}{2} a \Delta t^2$ & $\theta^p = r^i + w^i \Delta t + \dfrac{1}{2} \alpha \Delta t^2$

Update velocities $v^p = v^i + a \Delta t$ & $w^p = w^i + \alpha \Delta t$

Calculation

Energy: $U(\vec{r})$

Forces: $F = \nabla U(\vec{r}, \hat{u})$ and $\tau = \vec{r} \times \nabla U(\vec{r}, \hat{u})$

accelerations: $a = F/m$ & $\alpha = \tau/m$

Repeat

Correction

Move atoms: $r^{i+1} = r^p + f_1(a, \Delta t)$ & $\theta^{i+1} = \theta^p + f_2(\alpha, \Delta t)$

Update velocities: $v^{i+1} = v^p + g_1(a, \Delta t)$ & $w^{i+1} = w^p + g_2(\alpha, \Delta t)$

Boundary conditions

Adjust Temperature, Pressure, and *Volume as needed*

Output

Time step

$t = t + \Delta t$

$i = i + 1$

Figure 1.1. Schematic figure showing the step-by-step process in Molecular dynamics simulation.

until the simulation completes the allowed simulation time.

In MD simulations, the intermolecular interactions are the most expensive part of simulation. Among them, the van der Waals interactions are short-range interactions and are often described by Lennard-Jones (LJ) potential:

$$U_{LJ}(r) = 4\epsilon \left[\left(\frac{\sigma}{r}\right)^{12} - \left(\frac{\sigma}{r}\right)^{6} \right], \tag{1.3}$$

where σ is diameter of a molecule and ϵ determines well depth of the attractive potential. The $1/r^6$ in the equation 1.3 is short-ranged. The $1/r^{12}$ repulsive part of the LJ potential prevents two or more molecules from occupying the same position. The electrostatic interactions are considered long-range interactions e.g. charge-charge interactions between molecules can be described by Coulomb's law:

$$U_{electrostatic}(r) = \frac{1}{4\pi\epsilon_o} \frac{q_1 q_2}{r}. \tag{1.4}$$

Electrostatic interactions decay much slower with the distance. For charge-charge, they fall off as $\frac{1}{r}$. If the lowest order moment in the molecule is a dipole, the electrostatic interaction will falls off by $1/r^3$. Even if the lowest order moment in molecule is a quadrupole, the electrostatic interaction will decay by $1/r^5$ which is longer range than LJ interaction. Since the electrostatic interaction decays slowly, we need to consider a large number of molecules around it to capture physical behavior due to interactions. Consideration of interactions with large number of molecules is not computationally efficient. The most important challenge in the molecular dynamics communities have been to capture right electrostatic behavior of a molecule considering only its interaction with a small number of neighboring molecules. There have been many efforts to develop efficient and accurate algorithms to evaluate electrostatic interaction in molecular simulation, which will be

discussed in detail in section 1.3.

1.1.1 Peridic Boundary Condition (PBC)

Real liquid systems consist of very large number of molecules. But for computational efficiency, only a small number of particles ($\sim 10^3$) are usually considered in molecular simulations. On the other hand, if we want to study and predict bulk properties of the material using small number of molecules, a large fraction of molecules will be near the edge of the sample, contributing a huge surface effect. To eliminate surface effects, Periodic Boundary Conditions (PBC) have long been employed in various molecular simulations.[55] In PBC, the simulation box is replicated throughout the space to form an infinite lattice. In the course of simulation, if a molecule moves in the central box, its images in replicated boxes will also move in the similar fashion. Similarly when a molecule leaves the central box, one of its images will enter the box through opposite face to conserve total number of particle in a central box (see figure 1.2). Therefore the system acts like there is no wall at the boundary of the central box and eliminates the surface effect in the computation. If we want to evaluate potential energy of a molecule, we can consider its interactions with nearest molecules or images using the minimum image convention.[7] Even for minimum image convention, we need to calculate large number of pairwise distances at every time step. Consider a system of N molecules, the potential energy of ith molecule we need to find its distances r_{ij} with every j^{th} molecules or images in the system. Therefore in total we need to calculate $\frac{1}{2}N(N-1)$ number of distinct distances at every time-step, which can make the computation very expensive.
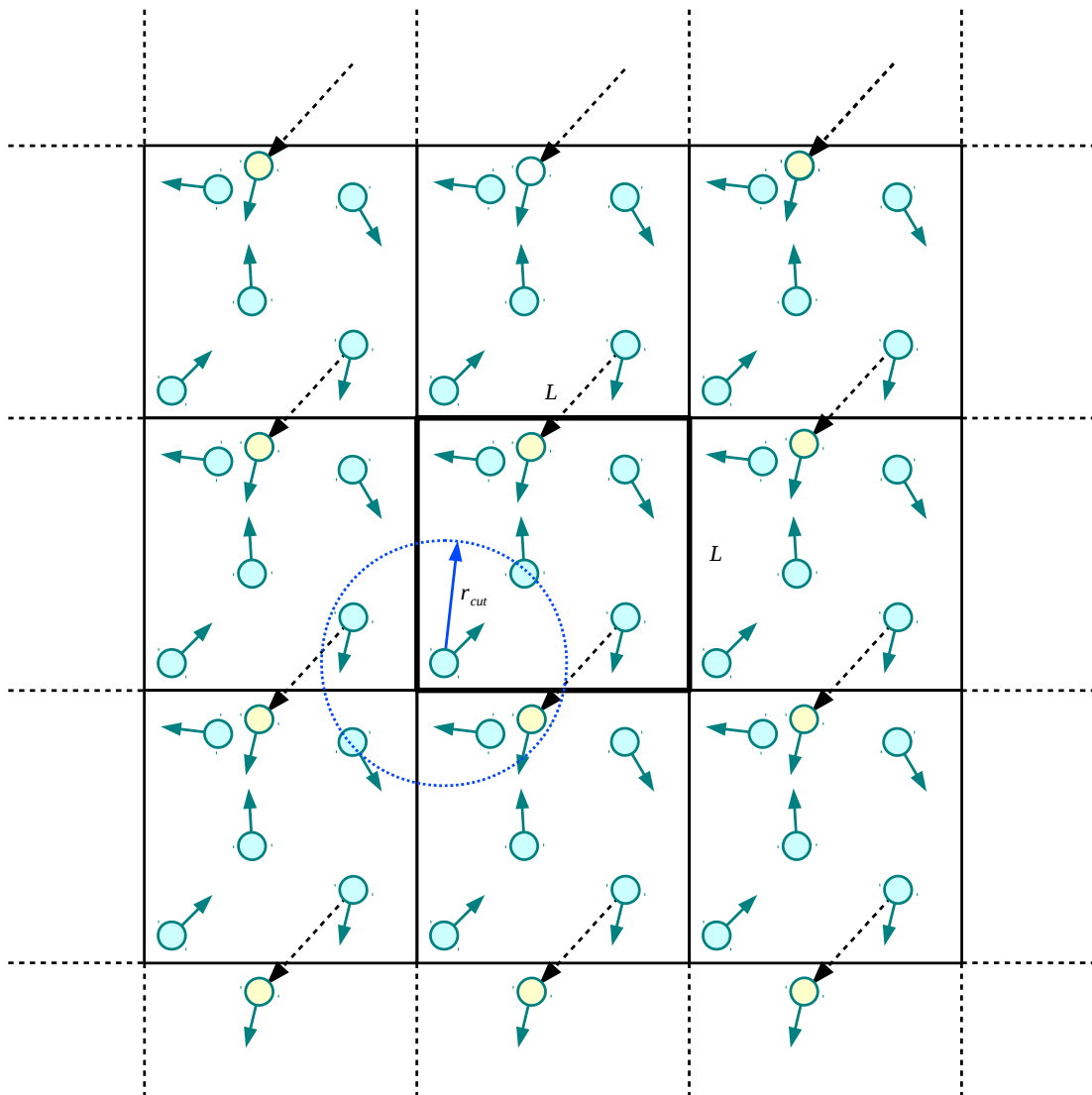
Figure 1.2. Periodic Boundary Condition for two dimensional (2D) molecular system. The central box is outlined using thicker line and replicated throughout the plane to form a 2D lattice. Usually in molecular simulations, the potential energy of the molecule is evaluated considering its interactions with the molecules or their images located in the spherical cutoff region as shown in blue dotted-circle.

1.1.2 Spherical truncation and Neighbor lists

If we assume the interaction between molecules is short-ranged, we can select small region around the molecule and consider that molecule only interacts with other molecules within that region. Often simulations use small cutoff regions around the molecule in order to make the MD simulation efficient. Beyond the cutoff region there is no interaction between the molecules. Consider a system of N molecules with box size L. If PBC is employed, r_{cut} should be less than $L/2$ in the molecular simulation. If $r_{cut} > L/2$, a molecule may interact with another molecule as well as its own image at the same time, which can lead to spurious correlations in molecular dynamics simulation. The spherical truncation implemented in PBC is shown in figure 1.2.

But evaluating all pair distances r_{ij} at every time step for determining whether or not a particular molecule is within cutoff region makes simulation computationally expensive. Therefore cutoff sphere r_{cut} is surrounded by the another larger sphere of radius r_{list} as shown in figure 1.3. At the beginning of the simulation a list of the molecules, the neighbour list, is constructed around each molecule. For a few time steps, only the molecules in the neighbour list are selected to check whether or not molecule is within the cutoff sphere. After a few time steps, the neighbour list is reconstructed by evaluating pair distances between every molecules. This reconstruction time is mainly determined by the dynamics of the molecules in the simulation.

1.2 Monte Carlo (MC) Simulation

We need to sample a large number of different configurations to study any physical and statistical properties of the system. These configurations must take into
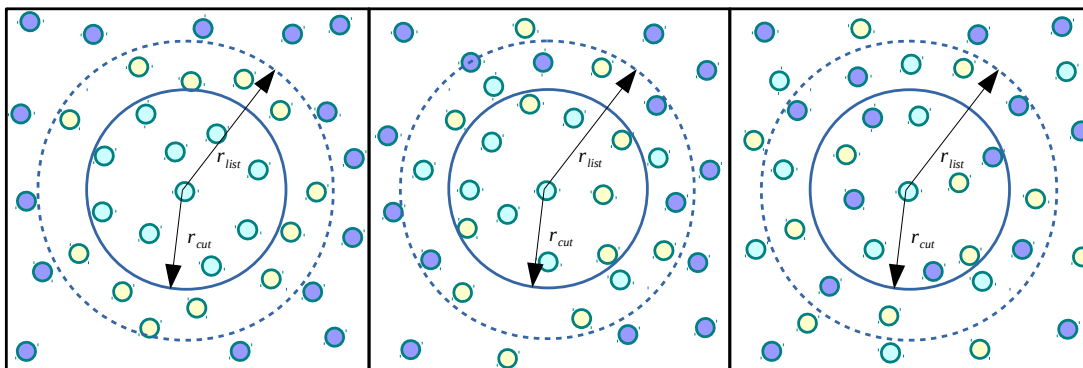
Figure 1.3. Region of neighbor list around the cutoff sphere. Molecules
in the cutoff region, neighbour list, and outer region are indicated by
green, yellow, and violet circles respectively. The neighbour list should
be reconstructed before molecules in the outer region starts to penetrate
the cutoff region.

account the ensemble being simulated. The Monte Carlo method uses probabilistic sampling of the system to generate representative configurations of the system. Each configuration depends only upon its predecessor but does not depend on the all the other configurations that were visited previously. For a canonical system, the probability of obtaining a given configuration is given by Boltzmann factor, $\exp(-\Delta E/k_B T)$. Metropolis *et.al* developed the selection criteria for acceptance of the subsequent configuration of the system. [57] According to their method, the new configuration of the system is accepted either $\Delta E < 0$ or $e^{-\frac{\Delta E}{k_B T}} > r$, where r is the random number between 0 and 1. The evaluation of the potential energy difference between subsequent configurations, ΔE, is very important in the MC simulation. For computational efficiency, this method also utilizes cutoff region r_{cut} as well as periodic boundary condition to calculate electrostatic interaction. Therefore developing an efficient and accurate electrostatic interaction method has always been subject of interest in the MC community.

1.3 Electrostatic Methods

Consider a system of N particles in a cubic box of length L replicated infinitely in 3D-space. The electrostatic potential energy for a particle with charge q_i and position r_i is given by

$$U_i = \sum_{n}' \sum_{j=1}^{N} \frac{q_i q_j}{|\mathbf{r}_i - \mathbf{r}_j + \mathbf{n}L|},$$
(1.5)

where q_j represents all other charges located at position $\mathbf{r}_j$ or in periodic replica and $\mathbf{n}$ is the cell-coordinate vector, $\mathbf{n}L = n_1 L\ \hat{x} + n_2 L\ \hat{y} + n_3 L\ \hat{z}$, where integers $n_1, n_2,$ and n_3 number cells along the x, y, and z directions and vary from 0 to ∞. The prime in the first sum indicates that $i = j$ should be ignored for the central box, i.e. $n = 0$. The factor $1/(4\pi\epsilon_o)$ has been dropped in the equation 1.5 for simplicity. The total potential energy of the system can be calculated as,

$$U = \sum_{\substack{i=1 \\ i \neq j}}^{N} U_i = \frac{1}{2} \sum_{n}' \sum_{i=1}^{N} \sum_{j=1}^{N} \frac{q_i q_j}{|\mathbf{r}_i - \mathbf{r}_j + \mathbf{n}L|},$$
(1.6)

where factor of 1/2 in the second part of the equation 1.6 is due to removal $i \neq j$ in the summation.

As we know the electrostatic interaction is a long-range interaction which is time consuming. On the other hand the potential energy evaluated using equation 1.5 converges conditionally to the correct value depending on the order of summation taken into account during calculation.[9] Therefore there have been many efforts to reduce computational cost and remove its conditionally convergent behavior.

1.3.1 Ewald Method

The Ewald method was originally proposed by Ewald in 1921 to evaluate electrostatic interactions in PBC. In this method, the electrostatic interaction can divided into two rapidly converging real and reciprocal space sums as well as a constant self-term. [90] Since $\mathrm{erf}(x) + \mathrm{erfc}(x) = 1$ we can write equation 1.6 as,

$$U = \frac{1}{2} \sum_{n}' \sum_{i=1}^{N} \sum_{j=1}^{N} q_i q_j \frac{\mathrm{erfc}(\alpha r_{ij,n}) + \mathrm{erf}(\alpha r_{ij,n})}{r_{ij,n}}. \tag{1.7}$$

The real-space term 1.8a in Ewald method is obtained by taking complementary error function term in the equation 1.7. Similarly reciprocal-space part 1.8b can be obtained by taking Fourier transform of the error function term in equation 1.7. The self-term present in the equation removes artificial interactions of the charge with its own images located in the periodic replicas.

$$U_{real} = \frac{1}{2} \sum_{i,j}^{N} \sum_{n}' q_i q_j \frac{\mathrm{erfc}(\alpha r_{ij,n})}{r_{ij,n}}, \tag{1.8a}$$

$$U_{reciprocal} = \frac{1}{2\pi V} \sum_{i,j}^{N} \sum_{\mathbf{m} \neq 0} \frac{\exp(-(\pi \mathbf{m}/\alpha)^2 + 2\pi i \mathbf{m} \cdot \mathbf{r}_{ij})}{\mathbf{m}^2}, \tag{1.8b}$$

$$U_{self} = -\frac{\alpha}{\sqrt{\pi}} \sum_{i=1}^{N} q_i^2, \tag{1.8c}$$

where V is the volume of the simulation box, $\mathbf{m}$ is a reciprocal-space vector, and α is a damping parameter which determines the rate of convergence in the real and reciprocal space.

Physically each point charge in the system can be assumed to be surrounded by a Gaussian distribution of equal magnitude but oppositely-signed charge (see

figure 1.4) with density,

$$\rho_i(r) = q_i \left(\frac{\alpha}{\sqrt{\pi}} \right)^3 \exp(-\alpha^2 r^2), \tag{1.9}$$

where α is a damping parameter determines the distribution of the charge, and r is the distance from the center of distribution. The imposed charge distribution around a charge screens the interactions between the charges making the effective interaction short ranged and therefore converges rapidly with distance. These Gaussian distributions are counteracted by other Gaussian distributions of charge having same magnitude but opposite sign as shown in figure 1.4. [90] The sum of potential energy due to second type of charge distributions converges in reciprocal space.

In the minimum image convention scheme, each particle can interact with its nearest particles or their image, the total number of interactions is $\frac{1}{2}N(N-1)$ in Ewald method. Therefore the algorithmic complexity for the Ewald method is $O(N^2)$. Recerz and Jacobs suggested that by choosing proper simulation parameters and minimum image convention schemes we can make reciprocal potential very small as compared to real-space potential so that can be ignored.[75] However this method is only applicable for a larger system but contribution of the reciprocal-space sum might not small for all systems, therefore is not recommended for general MD simulations. Perram *et al.* subdivided each simulation box into $m \times m \times m$ sub-boxes and selected damping parameter $\alpha = m\sqrt{-\log(\delta)}$, where δ is the relative error constant for neglecting the maximum term in the real-space sum, and using this technique they were able to reduce computational time to $O(N^{3/2})$.
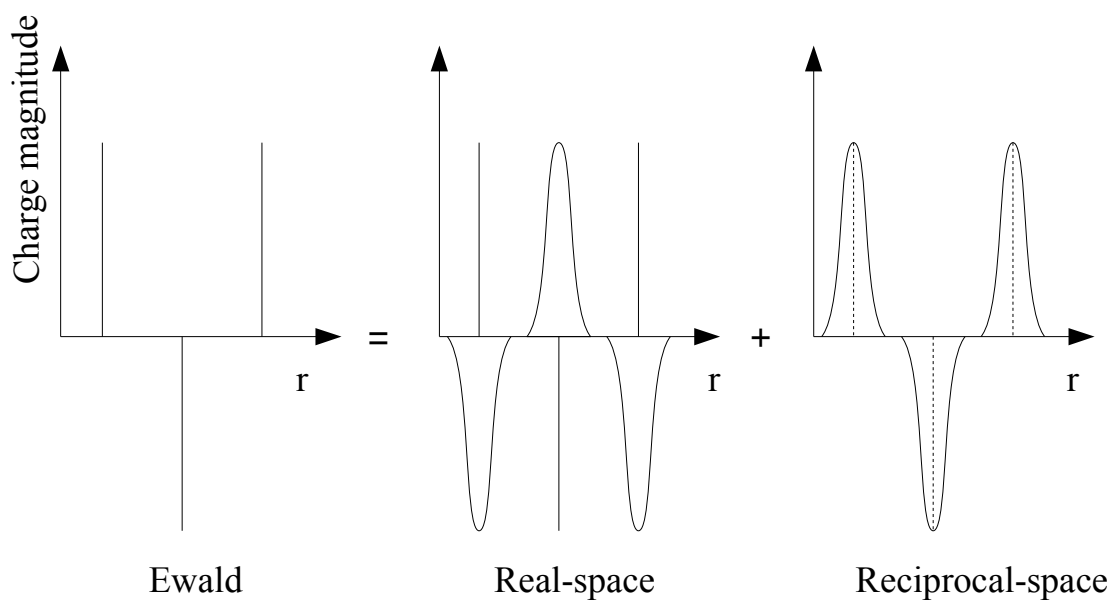
Figure 1.4. In the Ewald method each point charge is surrounded by a
Gaussian distribution of equal and oppositely-signed charge, evaluated
in real-space. These Gaussian distributions are compensated by the
opposite-singed Gaussian distribution of the charges calculated in
reciprocal-space

1.3.2   Fourier-based Ewald Methods

The Ewald method has been further modified using Fast Fourier transforms (FFT) to reduce complexity to $O(N \log(N))$. In these methods, charges are interpolated onto a 3D grid and the reciprocal sum is evaluated using FFTs. The particle-particle particle-mesh Ewald (PPPME) and particle-mesh Ewald (PME) methods are two widely-used Fourier-based Ewald methods.

1.3.2.1   Particle-Particle Particle-Mesh Ewald (PPPME)

The PPPME method was originally developed by Hockmney and Eastwood [31] and extended by Luty *et al.*.[52] and Rajagopal *et al.* [70] In this method, the electrostatic interaction is divided into short-ranged real-space and long-ranged reciprocal-space sums. The charges in the system are approximated as uniformly decreasing spherical charge density. The short-ranged potential within the cutoff radius $r < r_{cut}$ is calculated using electrostatic interactions between charge distributions. To calculate the long-ranged potential, first of all charges are assigned to the 3D grid as shown in figure 1.5 and transformed to the Fourier space for evaluating electrostatic potential. Since charges are assigned to the grid, it is very efficient to calculate electrostatic interactions in reciprocal space. Once the potential energy is evaluated, an inverse Fourier transformation is applied to calculate energy in real-space and it is numerically differentiated to get the force acting on the grid. Finally the electrostatic force (or energy) can be interpolated from the grid onto the particle locations to obtain actual force acting on the particle.

Although PPPME has complexity of $O(N \log N)$, for computational accuracy, we either need to refine the mesh or use better interpolation techniques, both of which are computational expensive. In addition to this, using numerical differ-
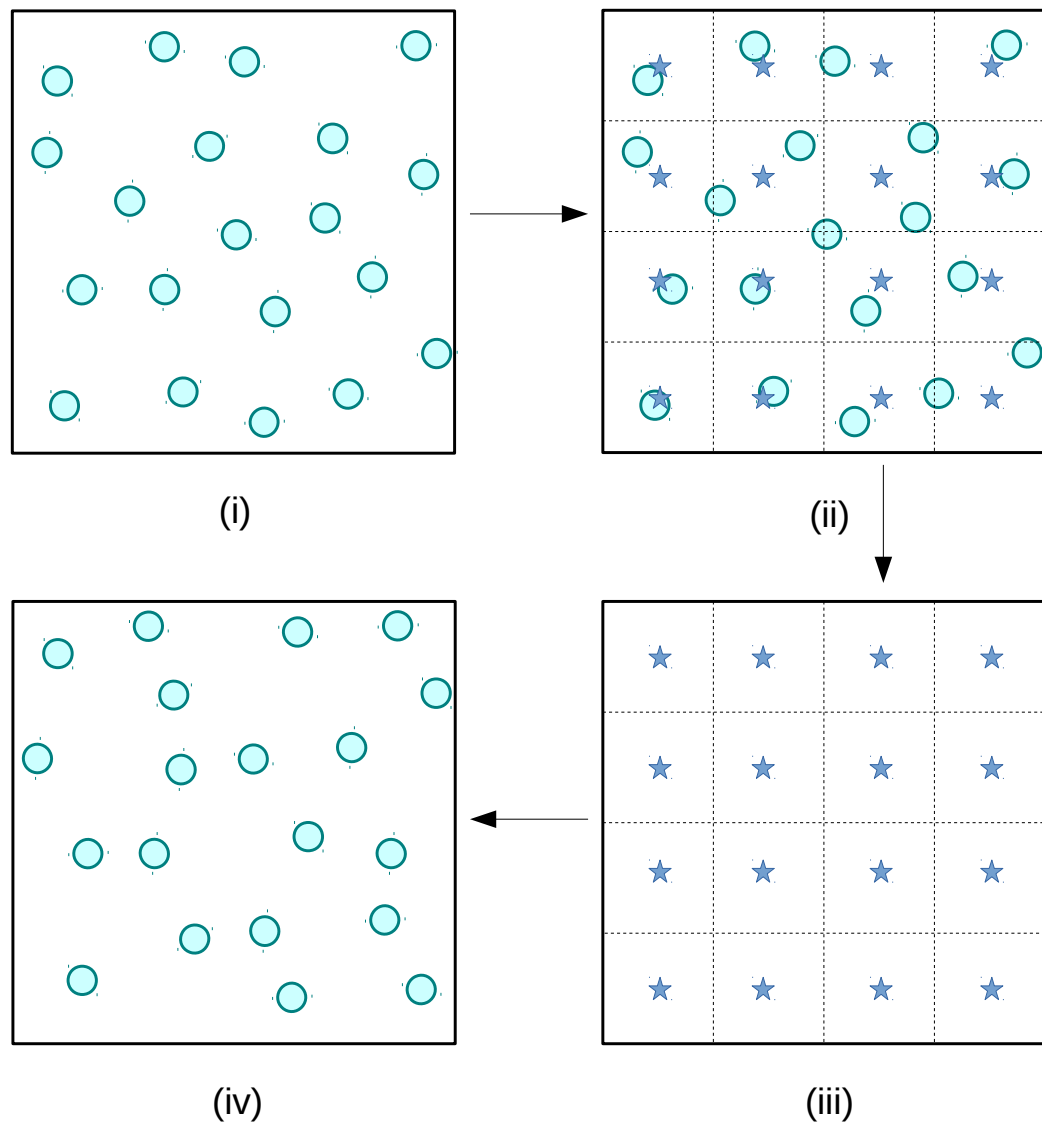
Figure 1.5. Schematic diagram for Fourier-based Ewald methods where green circle represents charge and blue star denotes grid point. In the figure, (i) a system of charges, (ii) charges mapped with grid points, (iii) force evaluated at the grid points, and (iv) force mapped back to the particles and their positions and velocities are updated.

entiation to calculate forces may introduce errors in the calculation. Therefore higher order differentiation schemes are often used in force calculations. In order to get optimal performance, all of the parameters; charge-distribution, interpolation technique, and differentiation schemes must be properly selected for a given system making parameter choices system specific. [90]

1.3.2.2 Particle-Mesh Ewald (PME)

This method is the modification of the PPPME method, in which the potential energy is divided into real-space and reciprocal-space sums. The charge is represented by the Gaussian distributions of charge. In this method, the real-space sum within the cutoff sphere is evaluated using actual electrostatic interactions between charges whereas the reciprocal sum is calculated in Fourier space using the idea of 3D grid as explained in the PPPME method. Unlike PPPME, this method evaluates force analytically, differentiating electrostatic energy at a given grid point reducing memory requirement significantly. This method also has $O(N\log N)$ algorithmic complexity and uses interpolation to map back electrostatic force from grid to the particle's location. Therefore users of this method need to discover optimal interpolation schemes to obtain excellent speed and accuracy for a simulation, making this method system dependent.

1.3.3 Real Space Methods

Before discussing the real space methods, the fundamental property of the electrostatic interactions in condensed phase environments should be considered. The electrostatic interaction between two charged particles decays as $1/r$. But molecular systems are usually composed of an equal number of positive and neg-

ative charges. Thus the range of interaction between a particular charge and rest of the charges in the system are different than the interaction between two bare charges. Consider a one dimensional (1D) crystal lattice composed of positive and negative charges. The potential energy of a particular ion can be considered as a sum of interactions with positive and negative ion pairs as shown in figure 3.1(a). Mathematically the potential energy for 1D crystal with alternating charges is given by a Madelung sum,

$$
\begin{aligned}
U^{Mad} &= -2q_iq_j \left(\frac{1}{a} - \frac{1}{2a} \right) - 2q_iq_j \left(\frac{1}{3a} - \frac{1}{4a} \right) - 2q_iq_j \left(\frac{1}{5a} - \frac{1}{6a} \right) + ... \\
&= - \left(\frac{2q_iq_j}{(1.414)^2 a} \right) - \left(\frac{2q_iq_j}{(3.464)^2 a} \right) - \left(\frac{2q_iq_j}{(5.477)^2 a} \right) + ...
\end{aligned}
\tag{1.10}
$$

If we consider all 3 terms in the equation 1.10 and compare their distances with the distance between central ion and group of ions as shown in figure 3.1(a), we clearly see that the interaction energy of a single ion with the pairs converges faster than $(1/r)$. Similarly, in a two dimensional (2D) lattice, the potential energy of an ion can be described as a sum of positive and negative four body groups as seen in figure 3.1(b). The interaction energy between an ion and group of four ions decays much faster than the charge-charge interaction. For a three-dimensional (3D) crystal, the potential energy of an ion can be considered as due to its interaction with the group of eight ions forming a cube. From this generalization, we can conclude that the electrostatic interaction energy for an ion in the crystalline system is a short-ranged as compared to charge-charge interaction. Therefore, even the relatively small systems should be able to represent bulk long-ranged interactions.

In order to reduce the computational expense of a molecular dynamics sim-
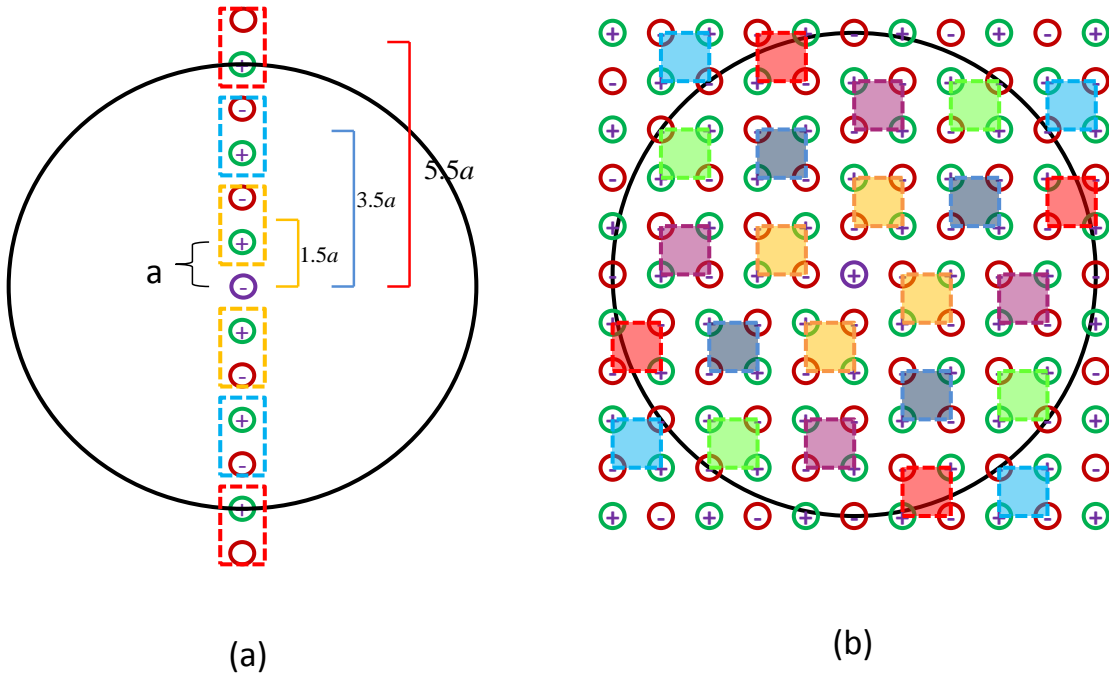
Figure 1.6. Schematic diagram showing grouping of ions in (a) 1D (b) 2D crystals. The interaction of the central ion with the group of ions decays faster than $1/r$. The direct spherical truncation breaks the ordering of the ions at the cut off sphere providing a net charge within the cutoff sphere. The breaking of the charge ordering increases with the crystal dimension resulting in a large net charge in the higher dimensional crystal.

ulation, interactions between particles are only considered if the particles exist within a cutoff distance r_c, of one another. We first consider how the energy of a system behaves if we truncate the interactions at the cutoff radius. Figure 1.7 shows (black line) that the electrostatic potential energy does not converge to the Madelung energy upon increasing the cutoff radius for the direct truncation. On the other hand the energy is found to be closer to the Madelung constant when the net charge within the cutoff radius is zero (figure 1.8). This oscillation in the potential energy is due to the breaking in charge ordering on the surface of the cutoff sphere which results in a net charge within the cutoff sphere. The size of the net charge is proportional to the dimension of the crystal. Although the interaction energy is short ranged, the direct truncation results in severe oscillation in energy for 3D crystal as shown in figure 1.7. Dipolar (or quadrupolar) crystals are also formed by ordering of the dipolar (or quadrupolar) molecules. Therefore similar oscillatory behaviour in the potential energy is due to the breaking of the ordering of dipoles (or quadrupoles) on the surface of the truncated sphere. Even in liquids there is local ordering of the molecules due to electrostatic interaction and similar oscillatory behaviour in the electrostatic potential has been seen in direct truncation approaches.

Wolf *et al* [95] proposed the idea of placing an image charge on the surface of cutoff sphere for every charge found within the sphere. The image charges should have opposite charge of those found within the sphere guaranteeing charge neutralization within the cutoff sphere.[95] This charge neutralization converges the potential energy to the correct Madelung energy as shown in figure 1.7 (orange line). In molecular dynamics (MD) simulations, the energy, force and torque should approach zero as the distance between molecules approaches the cutoff ra-
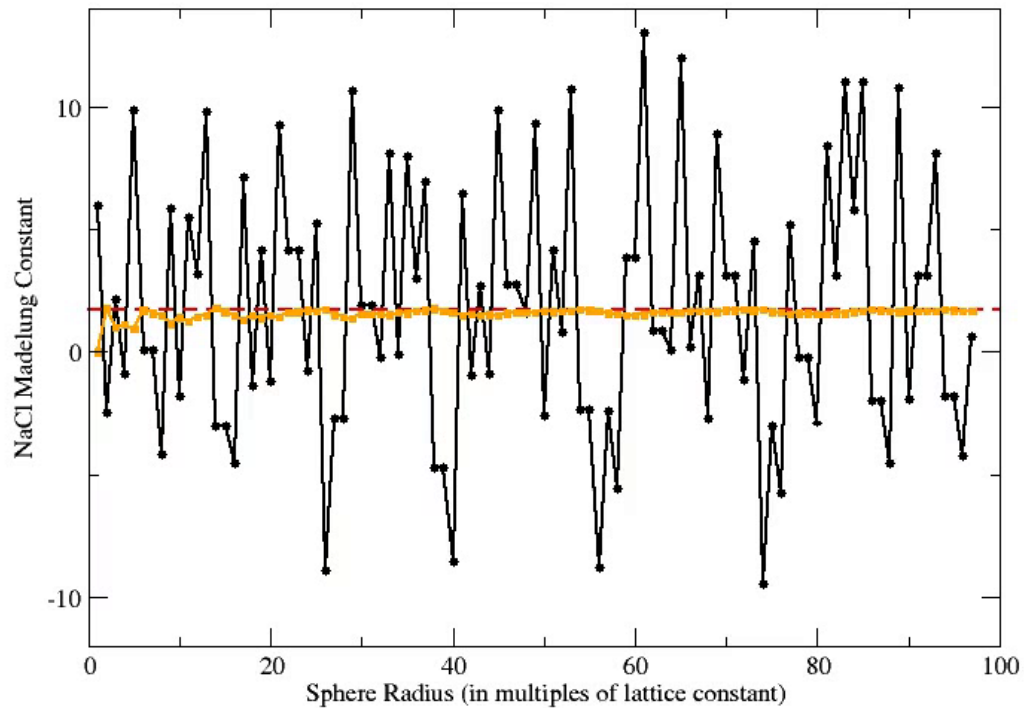
Figure 1.7. Convergence of the lattice energy constants for a 3D NaCl crystal as a function of cutoff radius for the direct (hard) cutoff method (black line). The orange line in the figure is for charge neutralized cutoff sphere (when image charge placed on the surface of the cutoff sphere). The red dotted line represents Madelung energy for NaCl crystal
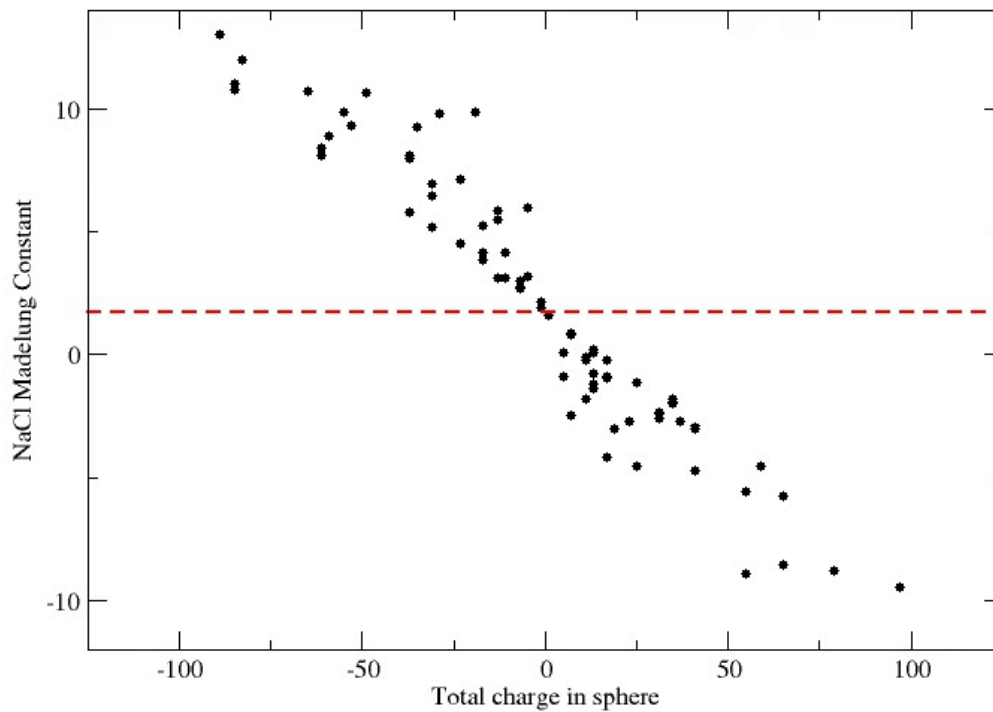
Figure 1.8. Convergence of the lattice energy constants for the NaCl crystal as a function of net charge within a cutoff sphere. The red dotted line represents Madelung energy for NaCl crystal

dius in order to conserve total energy. However Wolf's forces and torques derived from the potential do not go to zero at the cutoff radius, which makes it inappropriate to use in MD simulations. More recently, Zahn *et al.* and Fennell and Gezelter proposed the damped shifted force (DSF) potential, which incorporates Wolf's approach of image charges while ensuring the forces and torques approach zero at the cutoff radius.[18, 23] Fukuda has also recently been successful with the neutralization of higher order moments in a system of point charges.[25]

Real-space methods scale linearly with system size, are system-independent, and applicable a variety of condensed phase environments. Therefore we selected real-space methods for extending to higher-order charge-multipoles. In our research, we have generalized Wolf's shifted potential (SP) to the higher order electrostatic multipoles. We have also developed the gradient shifted force (GSF) and Taylor shifted force (TSF) potentials which are the natural extension of the damped shifted force (DSF) for higher order charge-multipoles. In the following chapter 2, I will discuss the development of the SP, GSF, and TSF methods and evaluate the energy constants for various dipolar and quadrupolar crystals using newly developed methods and compare with analytical results.[44]

CHAPTER 2

DEVELOPMENT OF METHODS

This chapter describes the detail mathematical development of the three real-space methods for computing electrostatic interactions between point multipoles. We generalize Wolf's Shfited-Potential (SP) for higher order charge multipoles (dipoles and quadrupoles). Additionally we extend Damped Shifted Force (DSF) method for dipoles and quadrupoles to develop Gradient Shifted Force (GSF) and Taylor Shifted Force (TSF) methods. Finally we evaluate lattice energy constant for different dipolar and quadrupolar crystals using newly developed real-space methods and compare with the analytically derived results.

2.1   Introduction

There has been increasing interest in real-space methods for calculating electrostatic interactions in computer simulations of condensed molecular systems [10–12, 17, 18, 23, 37, 42, 54, 74, 95] The simplest of these techniques was developed by Wolf *et al.* in their work towards an $\mathcal{O}(N)$ Coulombic sum.[95] For systems of point charges, Zahn *et al.* extended the Wolf approach by adding a force-shifting term to the enhanced damped Coulomb potential.[18, 42] Fennell and Gezelter showed that the simple damped shifted force (DSF) potential can give nearly quantitative agreement with smooth particle mesh Ewald (SPME)[22]

configurational energy differences as well as atomic force and molecular torque vectors.[23]

The computational efficiency and the accuracy of the DSF method are surprisingly good, particularly for systems with uniform charge density. Additionally, dielectric constants obtained using DSF and similar methods where the force vanishes at r_c are essentially quantitative.[37] The DSF and other related methods have now been widely investigated,[30] and DSF is now used routinely in a diverse set of chemical environments.[20, 24, 41, 48, 56, 78, 89] DSF electrostatics provides a compromise between the computational speed of real-space cutoffs and the accuracy of fully-periodic Ewald treatments.

One common feature of many coarse-graining approaches, which treat entire molecular subsystems as a single rigid body, is simplification of the electrostatic interactions between these bodies so that fewer site-site interactions are required to compute configurational energies. To do this, the interactions between coarse-grained sites are typically taken to be point multipoles.[29, 65, 66]

Water, in particular, has been modeled recently with point multipoles up to octupolar order.[14, 86–88] For maximum efficiency, these models require the use of an approximate multipole expansion as the exact multipole expansion can become quite expensive (particularly when handled via the Ewald sum).[35] Point multipoles and multipole polarizability have also been utilized in the AMOEBA water model and related force fields.[68, 71, 77]

Higher-order multipoles present a peculiar issue for molecular dynamics. Multipolar interactions are inherently short-ranged, and should not need the relatively expensive Ewald treatment. However, real-space cutoff methods are normally applied in an orientation-blind fashion so multipoles which leave and then re-enter

a cutoff sphere in a different orientation can cause energy discontinuities.

This chapter outlines an extension of the original DSF electrostatic kernel to point multipoles. We describe three distinct real-space interaction models for higher-order multipoles based on truncated Taylor expansions that are carried out at the cutoff radius. We are calling these models **Taylor-shifted** (TSF), **gradient-shifted** (GSF) and **shifted potential** (SP) electrostatics. Because of differences in the initial assumptions, the two methods yield related, but distinct expressions for energies, forces, and torques.

In this chapter we outline the new methodology and give functional forms for the energies, forces, and torques up to quadrupole-quadrupole order. We also compare the new methods to analytic energy constants for periodic arrays of point multipoles. In the following chapter, we provide numerical comparisons to Ewald-based electrostatics in common simulation environments.

2.2   Methodology

An efficient real-space electrostatic method involves the use of a pair-wise functional form,

$$U = \sum_i \sum_{j>i} U_{\text{pair}}(\mathbf{r}_{ij}, \mathsf{A}_i, \mathsf{B}_j) + \sum_i U_i^{\text{self}} \tag{2.1}$$

that is short-ranged and easily truncated at a cutoff radius,

$$U_{\text{pair}}(\mathbf{r}_{ij}, \mathsf{A}_i, \mathsf{B}_j) = \begin{cases} U_{\text{approx}}(\mathbf{r}_{ij}, \mathsf{A}_i, \mathsf{B}_j) & |\mathbf{r}_{ij}| \leq r_c \\ 0 & |\mathbf{r}_{ij}| > r_c, \end{cases} \tag{2.2}$$

along with an easily computed self-interaction term ($\sum_i U_i^{\text{self}}$) which scales linearly with the number of particles. Here A_i and B_j represent orientational coordinates of the two sites (expressed as rotation matrices), and $\mathbf{r}_{ij}$ is the vector between the two sites. The computational efficiency, energy conservation, and even some physical properties of a simulation can depend dramatically on how the U_{approx} function behaves at the cutoff radius. The goal of any approximation method should be to mimic the real behavior of the electrostatic interactions as closely as possible without sacrificing the near-linear scaling of a cutoff method.

2.2.1 Self-neutralization, damping, and force-shifting

The DSF and Wolf methods operate by neutralizing the total charge contained within the cutoff sphere surrounding each particle. This is accomplished by shifting the potential functions to generate image charges on the surface of the cutoff sphere for each pair interaction computed within r_c. Damping using a complementary error function is applied to the potential to accelerate convergence. The interaction for a pair of charges (C_i and C_j) in the DSF method,

$$
U_{\text{DSF}}(r_{ij}) = C_i C_j \left[\frac{\text{erfc}\left(\alpha r_{ij}\right)}{r_{ij}} - \frac{\text{erfc}\left(\alpha r_c\right)}{r_c} + \left(\frac{\text{erfc}\left(\alpha r_c\right)}{r_c^2} + \frac{2\alpha}{\pi^{1/2}} \frac{\exp\left(-\alpha^2 r_c^2\right)}{r_c} \right) \left(r_{ij} - r_c\right) \right]
$$

where α is the adjustable damping parameter. Note that in this potential and in all electrostatic quantities that follow, the standard $1/4\pi\epsilon_0$ has been omitted for clarity.

To insure net charge neutrality within each cutoff sphere, an additional "self" term is added to the potential. This term is constant (as long as the charges and cutoff radius do not change), and exists outside the normal pair-loop for molecular simulations. It can be thought of as a contribution from a charge opposite in sign,

but equal in magnitude, to the central charge, which has been spread out over the surface of the cutoff sphere. A portion of the self term is identical to the self term in the Ewald summation, and comes from the utilization of the complimentary error function for electrostatic damping.[16, 95] There have also been recent efforts to extend the Wolf self-neutralization method to zero out the dipole and higher order multipoles contained within the cutoff sphere.[25–27]

In this work, we extend the idea of self-neutralization for the point multipoles by insuring net charge-neutrality and net-zero moments within each cutoff sphere. In Figure 2.1, point dipole $\mathbf{D}_i$ at the center site i is interacting with point dipole $\mathbf{D}_j$ and point quadrupole Q_k. The self-neutralization scheme for point multipoles involves projecting opposing multipoles for sites j and k on the surface of the cutoff sphere. There are also significant modifications made to make the forces and torques go smoothly to zero at the cutoff distance.

As in the point-charge approach, there is an additional contribution from self-neutralization of site i. The self term for multipoles is described in section 2.2.9.

2.2.2 The multipole expansion

Consider two discrete rigid collections of point charges, denoted as objects a and b. In the following, we assume that the two objects interact via electrostatics only and describe those interactions in terms of a standard multipole expansion. Putting the origin of the coordinate system at the center of mass of a, we use vectors $\mathbf{r}_k$ to denote the positions of all charges q_k in a. Then the electrostatic potential of object a at $\mathbf{r}$ is given by

$$\phi_a(\mathbf{r}) = \sum_{k \text{ in } a} \frac{q_k}{|\mathbf{r} - \mathbf{r}_k|}.$$

(2.3)
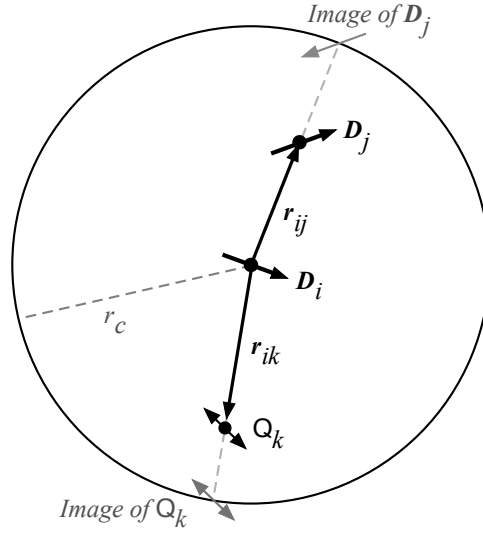
Figure 2.1. Reversed multipoles are projected onto the surface of the cutoff sphere. The forces, torques, and potential are then smoothly shifted to zero as the sites leave the cutoff region.

The Taylor expansion in r can be written using an implied summation notation. Here Greek indices are used to indicate space coordinates (x, y, z) and the subscripts k and j are reserved for labeling specific sites for charges in a and b respectively. The Taylor expansion,

$$\frac{1}{|\mathbf{r} - \mathbf{r}_k|} = \left(1 - r_{k\alpha} \frac{\partial}{\partial r_\alpha} + \frac{1}{2} r_{k\alpha} r_{k\beta} \frac{\partial^2}{\partial r_\alpha \partial r_\beta} + \dots \right) \frac{1}{r}, \tag{2.4}$$

can then be used to express the electrostatic potential on a in terms of multipole operators,

$$\phi_a(\mathbf{r}) = M_a \frac{1}{r} \tag{2.5}$$

where

$$M_a = C_a - D_{a\alpha} \frac{\partial}{\partial r_\alpha} + Q_{a\alpha\beta} \frac{\partial^2}{\partial r_\alpha \partial r_\beta} + \dots \tag{2.6}$$

29

Here, the point charge, dipole, and quadrupole for object a are given by C_a, $\mathbf{D}_a$, and $\mathbf{Q}_a$, respectively. These are the primitive multipoles which can be expressed as a distribution of charges,

$$C_a = \sum_{k \text{ in } a} q_k, \tag{2.7}$$

$$D_{a\alpha} = \sum_{k \text{ in } a} q_k r_{k\alpha}, \tag{2.8}$$

$$Q_{a\alpha\beta} = \frac{1}{2} \sum_{k \text{ in } a} q_k r_{k\alpha} r_{k\beta}. \tag{2.9}$$

Note that the definition of the primitive quadrupole here differs from the standard traceless form, and contains an additional Taylor-series based factor of $1/2$. We are essentially treating the mass distribution with higher priority; the moment of inertia tensor, $\mathbf{I}$, is diagonalized to obtain body-fixed axes, and the charge distribution may result in a quadrupole tensor that is not necessarily diagonal in the body frame. Additional reasons for utilizing the primitive quadrupole are discussed in section 2.2.3.

It is convenient to locate charges q_j relative to the center of mass of b. Then with $\mathbf{r}$ pointing from the center of mass of a to the center of mass of b ($\mathbf{r} = \mathbf{r}_b - \mathbf{r}_a$), the interaction energy is given by

$$U_{ab}(r) = M_a \sum_{j \text{ in } b} \frac{q_j}{|\mathbf{r} + \mathbf{r}_j|}. \tag{2.10}$$

This can also be expanded as a Taylor series in r. Using a notation similar to before to define the multipoles in object b,

$$M_b = C_b + D_{b\alpha} \frac{\partial}{\partial r_\alpha} + Q_{b\alpha\beta} \frac{\partial^2}{\partial r_\alpha \partial r_\beta} + \dots \tag{2.11}$$

we arrive at the multipole expression for the total interaction energy.

$$U_{ab}(r) = M_a M_b \frac{1}{r}. \tag{2.12}$$

This form has the benefit of separating out the energies of interaction into con-
tributions from the charge, dipole, and quadrupole of a interacting with the same
types of multipoles in b.

2.2.3 Damped Coulomb interactions

In the standard multipole expansion, one typically uses the bare Coulomb
potential, with radial dependence $1/r$, as shown in Eq. (2.12). It is also quite
common to use a damped Coulomb interaction, which results from replacing point
charges with Gaussian distributions of charge with width α. In damped multipole
electrostatics, the kernel $(1/r)$ of the expansion is replaced with the function:

$$B_0(r) = \frac{\text{erfc}(\alpha r)}{r} = \frac{2}{\sqrt{\pi} r} \int_{\alpha r}^{\infty} e^{-s^2} ds. \tag{2.13}$$

We develop equations below using the function $f(r)$ to represent either $1/r$ or
$B_0(r)$, and all of the techniques can be applied to bare or damped Coulomb kernels
(or any other function) as long as derivatives of these functions are known. Smith's
convenient functions $B_l(r)$, which are used for derivatives of the damped kernel,
are summarized in Appendix A. (N.B. there is one important distinction between
the two kernels, which is the behavior of $\nabla^2 \frac{1}{r}$ compared with $\nabla^2 B_0(r)$. The former
is zero everywhere except for a delta function evaluated at the origin. The latter
also has delta function behavior, but is non-zero for $r \neq 0$. Thus the standard
justification for using a traceless quadrupole tensor fails for the damped case.)

The main goal of this work is to smoothly cut off the interaction energy as well as forces and torques as $r \to r_c$. To describe how this goal may be met, we use two examples, charge-charge and charge-dipole, using the bare Coulomb kernel, $f(r) = 1/r$, to explain the idea.

2.2.4 Shifted-force methods

In the shifted-force approximation, the interaction energy for two charges C_a and C_b separated by a distance r is written:

$$U_{C_a C_b}(r) = C_a C_b \left(\frac{1}{r} - \frac{1}{r_c} + (r - r_c)\frac{1}{r_c^2} \right). \tag{2.14}$$

Two shifting terms appear in this equations, one from the neutralization procedure $(-1/r_c)$, and one that causes the first derivative to vanish at the cutoff radius.

Since one derivative of the interaction energy is needed for the force, the minimal perturbation is a term linear in $(r - r_c)$ in the interaction energy, that is:

$$\frac{d}{dr} \left(\frac{1}{r} - \frac{1}{r_c} + (r - r_c)\frac{1}{r_c^2} \right) = \left(-\frac{1}{r^2} + \frac{1}{r_c^2} \right). \tag{2.15}$$

which clearly vanishes as the r approaches the cutoff radius. There are a number of ways to generalize this derivative shift for higher-order multipoles. Below, we present two methods, one based on higher-order Taylor series for r near r_c, and the other based on linear shift of the kernel gradients at the cutoff itself.

2.2.5 Taylor-shifted force (TSF) electrostatics

In the Taylor-shifted force (TSF) method, the procedure that we follow is based on a Taylor expansion containing the same number of derivatives required for

each force term to vanish at the cutoff. For example, the quadrupole-quadrupole interaction energy requires four derivatives of the kernel, and the force requires one additional derivative. For quadrupole-quadrupole interactions, we therefore require shifted energy expressions that include up to $(r - r_c)^5$ so that all energies, forces, and torques are zero as $r \to r_c$. In each case, we subtract off a function $f_n^{\text{shift}}(r)$ from the kernel $f(r) = 1/r$. The subscript n indicates the number of derivatives to be taken when deriving a given multipole energy. We choose a function with guaranteed smooth derivatives – a truncated Taylor series of the function $f(r)$, e.g.,

$$f_n^{\text{shift}}(r) = \sum_{m=0}^{n+1} \frac{(r - r_c)^m}{m!} f^{(m)}(r_c). \tag{2.16}$$

The combination of $f(r)$ with the shifted function is denoted $f_n(r) = f(r) - f_n^{\text{shift}}(r)$. Thus, for $f(r) = 1/r$, we find

$$f_1(r) = \frac{1}{r} - \frac{1}{r_c} + (r - r_c)\frac{1}{r_c^2} - \frac{(r - r_c)^2}{r_c^3}. \tag{2.17}$$

Continuing with the example of a charge a interacting with a dipole b, we write

$$U_{C_a \mathbf{D}_b}(r) = C_a D_{b\alpha} \frac{\partial f_1(r)}{\partial r_\alpha} = C_a D_{b\alpha} \frac{r_\alpha}{r} \frac{\partial f_1(r)}{\partial r}. \tag{2.18}$$

The force that dipole b exerts on charge a is

$$F_{C_a \mathbf{D}_b \beta} = C_a D_{b\alpha} \left[\frac{\delta_{\alpha\beta}}{r} \frac{\partial}{\partial r} + \frac{r_\alpha r_\beta}{r^2} \left(-\frac{1}{r} \frac{\partial}{\partial r} + \frac{\partial^2}{\partial r^2} \right) \right] f_1(r). \tag{2.19}$$

For undamped coulombic interactions, $f(r) = 1/r$, we find

$$F_{C_a \mathbf{D}_b \beta} = \frac{C_a D_{b\beta}}{r} \left[-\frac{1}{r^2} + \frac{1}{r_c^2} - \frac{2(r - r_c)}{r_c^3} \right] + C_a D_{b\alpha} r_\alpha r_\beta \left[\frac{3}{r^5} - \frac{3}{r^3 r_c^2} \right]. \tag{2.20}$$

33

This expansion shows the expected $1/r^3$ dependence of the force.

In general, we can write

$$U^{\mathrm{TSF}} = (\text{prefactor})(\text{derivatives})f_n(r) \qquad (2.21)$$

with $n = 0$ for charge-charge, $n = 1$ for charge-dipole, $n = 2$ for charge-quadrupole and dipole-dipole, $n = 3$ for dipole-quadrupole, and $n = 4$ for quadrupole-quadrupole. For example, in quadrupole-quadrupole interactions for which the prefactor is $Q_{a\alpha\beta}Q_{b\gamma\delta}$, the derivatives are $\partial^4/\partial r_\alpha \partial r_\beta \partial r_\gamma \partial r_\delta$, with implied summation combining the space indices. Appendix A.2 contains details on the radial functions.

In the formulas presented in the tables below, the placeholder function $f(r)$ is used to represent the electrostatic kernel (either damped or undamped). The main functions that go into the force and torque terms, $g_n(r), h_n(r), s_n(r),$ and $t_n(r)$ are successive derivatives of the shifted electrostatic kernel, $f_n(r)$ of the same index n. The algebra required to evaluate energies, forces and torques is somewhat tedious, so only the final forms are presented in tables 2.2 and 2.3. One of the principal findings of our work is that the individual orientational contributions to the various multipole-multipole interactions must be treated with distinct radial functions, but each of these contributions is independently force shifted at the cutoff radius.

2.2.6 Gradient-shifted force (GSF) electrostatics

The second, and conceptually simpler approach to force-shifting maintains only the linear $(r - r_c)$ term in the truncated Taylor expansion, and has a similar

interaction energy for all multipole orders:

$$U^{\text{GSF}} = \sum [U(\mathbf{r}, \mathsf{A}, \mathsf{B}) - U(r_c\hat{\mathbf{r}}, \mathsf{A}, \mathsf{B}) - (r - r_c)\hat{\mathbf{r}} \cdot \nabla U(r_c\hat{\mathbf{r}}, \mathsf{A}, \mathsf{B})] \qquad (2.22)$$

where $\hat{\mathbf{r}}$ is the unit vector pointing between the two multipoles, and the sum describes a separate force-shifting that is applied to each orientational contribution to the energy. Both the potential and the gradient for force shifting are evaluated for an image multipole projected onto the surface of the cutoff sphere (see fig 2.1). The image multipole retains the orientation (rotation matrix B) of the interacting multipole. No higher order terms $(r - r_c)^n$ appear. The primary difference between the TSF and GSF methods is the stage at which the Taylor Series is applied; in the Taylor-shifted approach, it is applied to the kernel itself. In the Gradient-shifted approach, it is applied to individual radial interaction terms in the multipole expansion. Energies from this method thus have the general form:

$$U = \sum (\text{angular factor})(\text{radial factor}). \qquad (2.23)$$

Functional forms for both methods (TSF and GSF) can both be summarized using the form of Eq. 2.23). The basic forms for the energy, force, and torque expressions are tabulated for both shifting approaches below – for each separate orientational contribution, only the radial factors differ between the two methods.

2.2.7 Generalization of the Wolf shifted potential (SP)

It is also possible to formulate an extension of the Wolf approach for multipoles by simply projecting the image multipole onto the surface of the cutoff sphere, and including the interactions with the central multipole and the image. This

effectively shifts the pair potential to zero at the cutoff radius,

$$U^{\text{SP}} = \sum \left[U(\mathbf{r}, \mathsf{A}, \mathsf{B}) - U(r_c \hat{\mathbf{r}}, \mathsf{A}, \mathsf{B}) \right] \tag{2.24}$$

independent of the orientations of the two multipoles. The sum again describes separate potential shifting that is applied to each orientational contribution to the energy.

The shifted potential (SP) method is a simple truncation of the GSF method for each orientational contribution, leaving out the $(r - r_c)$ terms that multiply the gradient. Functional forms for the shifted-potential (SP) method can also be summarized using the form of Eq. 2.23. The energy, force, and torque expressions are tabulated below for all three methods. As in the GSF and TSF methods, for each separate orientational contribution, only the radial factors differ between the SP, GSF, and TSF methods.

2.2.8 Body and space axes

Although objects a and b rotate during a molecular dynamics (MD) simulation, their multipole tensors remain fixed in body-frame coordinates. While deriving force and torque expressions, it is therefore convenient to write the energies, forces, and torques in intermediate forms involving the vectors of the rotation matrices. We denote body axes for objects a and b using unit vectors $\hat{\mathbf{A}}_m$ and $\hat{\mathbf{B}}_m$, respectively, with the index $m = (123)$. In a typical simulation, the initial axes are obtained by diagonalizing the moment of inertia tensors for the objects. (N.B., the body axes are generally *not* the same as those for which the quadrupole moment is diagonal.) The rotation matrices are then propagated during the simulation.

The rotation matrices A and B can be expressed using these unit vectors:

$$\mathsf{A} = \begin{pmatrix} \hat{\mathbf{A}}_1 \\ \hat{\mathbf{A}}_2 \\ \hat{\mathbf{A}}_3 \end{pmatrix}, \qquad \mathsf{B} = \begin{pmatrix} \hat{\mathbf{B}}_1 \\ \hat{\mathbf{B}}_2 \\ \hat{\mathbf{B}}_3 \end{pmatrix} \tag{2.25}$$

These matrices convert from space-fixed (xyz) to body-fixed (123) coordinates.

Allen and Germano,[8] following earlier work by Price *et al.*,[69] showed that if the interaction energies are written explicitly in terms of $\hat{\mathbf{r}}$ and the body axes $(\hat{\mathbf{A}}_m, \hat{\mathbf{B}}_n)$:

$$U(r, \{\hat{\mathbf{A}}_m \cdot \hat{\mathbf{r}}\}, \{\hat{\mathbf{B}}_n \cdot \hat{\mathbf{r}}\}, \{\hat{\mathbf{A}}_m \cdot \hat{\mathbf{B}}_n\}). \tag{2.26}$$

the forces come out relatively cleanly,

$$\mathbf{F}_a = -\mathbf{F}_b = \nabla U = \frac{\partial U}{\partial \mathbf{r}} = \frac{\partial U}{\partial r}\hat{\mathbf{r}} + \sum_m \left[\frac{\partial U}{\partial(\hat{\mathbf{A}}_m \cdot \hat{\mathbf{r}})} \frac{\partial(\hat{\mathbf{A}}_m \cdot \hat{\mathbf{r}})}{\partial \mathbf{r}} + \frac{\partial U}{\partial(\hat{\mathbf{B}}_m \cdot \hat{\mathbf{r}})} \frac{\partial(\hat{\mathbf{B}}_m \cdot \hat{\mathbf{r}})}{\partial \mathbf{r}} \right].$$
$$\tag{2.27}$$

The torques can also be found in a relatively similar manner,

$$\tau_a = \sum_m \frac{\partial U}{\partial(\hat{\mathbf{A}}_m \cdot \hat{\mathbf{r}})}(\hat{\mathbf{r}} \times \hat{\mathbf{A}}_m) - \sum_{mn} \frac{\partial U}{\partial(\hat{\mathbf{A}}_m \cdot \hat{\mathbf{B}}_n)}(\hat{\mathbf{A}}_m \times \hat{\mathbf{B}}_n) \tag{2.28}$$

$$\tau_b = \sum_m \frac{\partial U}{\partial(\hat{\mathbf{B}}_m \cdot \hat{\mathbf{r}})}(\hat{\mathbf{r}} \times \hat{\mathbf{B}}_m) + \sum_{mn} \frac{\partial U}{\partial(\hat{\mathbf{A}}_m \cdot \hat{\mathbf{B}}_n)}(\hat{\mathbf{A}}_m \times \hat{\mathbf{B}}_n). \tag{2.29}$$

Note that our definition of $\mathbf{r} = \mathbf{r}_b - \mathbf{r}_a$ is opposite in sign to that of Allen and Germano.[8] We also made use of the identities,

$$\frac{\partial(\hat{\mathbf{A}}_m \cdot \hat{\mathbf{r}})}{\partial \mathbf{r}} = \frac{1}{r} \left(\hat{\mathbf{A}}_m - (\hat{\mathbf{A}}_m \cdot \hat{\mathbf{r}})\hat{\mathbf{r}} \right) \tag{2.30}$$

$$\frac{\partial(\hat{\mathbf{B}}_m \cdot \hat{\mathbf{r}})}{\partial \mathbf{r}} = \frac{1}{r} \left(\hat{\mathbf{B}}_m - (\hat{\mathbf{B}}_m \cdot \hat{\mathbf{r}})\hat{\mathbf{r}} \right). \tag{2.31}$$

Many of the multipole contractions required can be written in one of three equivalent forms using the unit vectors $\hat{\mathbf{r}}$, $\hat{\mathbf{A}}_m$, and $\hat{\mathbf{B}}_n$. In the torque expressions, it is useful to have the angular-dependent terms available in all three fashions, e.g. for the dipole-dipole contraction:

$$\mathbf{D}_a \cdot \mathbf{D}_b = D_{a\alpha} D_{b\alpha} = \sum_{mn} D_{am} \hat{\mathbf{A}}_m \cdot \hat{\mathbf{B}}_n D_{bn}. \qquad (2.32)$$

The first two forms are written using space coordinates. The first form is standard in the chemistry literature, while the second is expressed using implied summation notation. The third form shows explicit sums over body indices and the dot products now indicate contractions using space indices.

In computing our force and torque expressions, we carried out most of the work in body coordinates, and have transformed the expressions back to space-frame coordinates, which are reported below. Interested readers may consult the supplemental information for the paper I [**?**] for the intermediate body-frame expressions.[1]

2.2.9 The Self-Interaction

In addition to cutoff-sphere neutralization, the Wolf summation [95] and the damped shifted force (DSF) extension [23] also include self-interactions that are handled separately from the pairwise interactions between sites. The self-term is normally calculated via a single loop over all sites in the system, and is relatively cheap to evaluate. The self-interaction has contributions from two sources.

First, the neutralization procedure within the cutoff radius requires a contribution from a charge opposite in sign, but equal in magnitude, to the central charge, which has been spread out over the surface of the cutoff sphere. For a system of

TABLE 2.1: Self-interaction contributions for site (a) that has a charge (C_a), dipole $(\mathbf{D}_a)$, and quadrupole $(\mathbf{Q}_a)$

Multipole order	Summed Quantity	Self-neutralization	Reciprocal
Charge	C_a^2	$-f(r_c)$	$-\frac{\alpha}{\sqrt{\pi}}$
Dipole	$|\mathbf{D}_a|^2$	$\frac{1}{3}\left(h(r_c) + \frac{2g(r_c)}{r_c}\right)$	$-\frac{2\alpha^3}{3\sqrt{\pi}}$
Quadrupole	$2\mathbf{Q}_a : \mathbf{Q}_a + \mathrm{Tr}(\mathbf{Q}_a)^2$	$-\frac{1}{15}\left(t(r_c) + \frac{4s(r_c)}{r_c}\right)$	$-\frac{4\alpha^5}{5\sqrt{\pi}}$
Charge-Quadrupole	$-2C_a\mathrm{Tr}(\mathbf{Q}_a)$	$\frac{1}{3}\left(h(r_c) + \frac{2g(r_c)}{r_c}\right)$	$-\frac{2\alpha^3}{3\sqrt{\pi}}$

undamped charges, the total self-term is

$$U_{\text{self}} = -\frac{1}{r_c}\sum_{a=1}^{N} C_a^2. \tag{2.33}$$

The extension of DSF electrostatics to point multipoles requires treatment of the self-neutralization *and* reciprocal contributions to the self-interaction for higher order multipoles. In this section we give formulae for these interactions up to quadrupolar order.

The self-neutralization term is computed by taking the *non-shifted* kernel for each interaction, placing a multipole of equal magnitude (but opposite in polarization) on the surface of the cutoff sphere, and averaging over the surface of the cutoff sphere. Because the self term is carried out as a single sum over sites, the reciprocal-space portion is identical to half of the self-term obtained by Smith, and also by Aguado and Madden for the application of the Ewald sum to multipoles.[6, 82, 83] For a given site which possesses a charge, dipole, and quadrupole, both types of contribution are given in table 2.1.

For sites which simultaneously contain charges and quadrupoles, the self-interaction includes a cross-interaction between these two multipole orders. Symmetry prevents the charge-dipole and dipole-quadrupole interactions from con-

tributing to the self-interaction. The functions that go into the self-neutralization terms, $g(r), h(r), s(r),$ and $t(r)$ are successive derivatives of the electrostatic kernel, $f(r)$ (either the undamped $1/r$ or the damped $B_0(r) = \text{erfc}(\alpha r)/r$ function) that have been evaluated at the cutoff distance. For undamped interactions, $f(r_c) = 1/r_c$, $g(r_c) = -1/r_c^2$, and so on. For damped interactions, $f(r_c) = B_0(r_c)$, $g(r_c) = B_0'(r_c)$, and so on. Appendix A.1 contains recursion relations that allow rapid evaluation of these derivatives.

2.3   Interaction energies, forces, and torques

The main result of this chapter is a set of expressions for the energies, forces and torques (up to quadrupole-quadrupole order) that work for the Taylor-shifted, gradient-shifted, and shifted potential approximations. These expressions were derived using a set of generic radial functions. Without using the shifting approximations mentioned above, some of these radial functions would be identical, and the expressions coalesce into the familiar forms for unmodified multipole-multipole interactions. Table 2.2 maps between the generic functions and the radial functions derived for the three methods. The energy equations are written in terms of lab-frame representations of the dipoles, quadrupoles, and the unit vector connecting the two objects,

$$U_{C_aC_b}(r) = C_aC_b v_{01}(r) \tag{2.34}$$

$$U_{C_a\mathbf{D}_b}(r) = C_a\left(\mathbf{D}_b \cdot \hat{\mathbf{r}}\right) v_{11}(r) \tag{2.35}$$

$$U_{C_a\mathbf{Q}_b}(r) = C_a\left[\mathrm{Tr}\mathbf{Q}_b v_{21}(r) + (\hat{\mathbf{r}} \cdot \mathbf{Q}_b \cdot \hat{\mathbf{r}})\, v_{22}(r)\right] \tag{2.36}$$

$$U_{\mathbf{D}_a\mathbf{D}_b}(r) = -\left[\left(\mathbf{D}_a \cdot \mathbf{D}_b\right) v_{21}(r) + \left(\mathbf{D}_a \cdot \hat{\mathbf{r}}\right)\left(\mathbf{D}_b \cdot \hat{\mathbf{r}}\right) v_{22}(r)\right] \tag{2.37}$$

$$U_{\mathbf{D}_a\mathbf{Q}_b}(r) = -\left[\mathrm{Tr}\mathbf{Q}_b\left(\mathbf{D}_a \cdot \hat{\mathbf{r}}\right) + 2(\mathbf{D}_a \cdot \mathbf{Q}_b \cdot \hat{\mathbf{r}})\right] v_{31}(r)$$
$$- \left(\mathbf{D}_a \cdot \hat{\mathbf{r}}\right)\left(\hat{\mathbf{r}} \cdot \mathbf{Q}_b \cdot \hat{\mathbf{r}}\right) v_{32}(r) \tag{2.38}$$

$$U_{\mathbf{Q}_a\mathbf{Q}_b}(r) = \left[\mathrm{Tr}\mathbf{Q}_a\,\mathrm{Tr}\mathbf{Q}_b + 2\mathbf{Q}_a : \mathbf{Q}_b\right] v_{41}(r)$$
$$+ \left[\mathrm{Tr}\mathbf{Q}_a\left(\hat{\mathbf{r}} \cdot \mathbf{Q}_b \cdot \hat{\mathbf{r}}\right) + \mathrm{Tr}\mathbf{Q}_b\left(\hat{\mathbf{r}} \cdot \mathbf{Q}_a \cdot \hat{\mathbf{r}}\right) + 4(\hat{\mathbf{r}} \cdot \mathbf{Q}_a \cdot \mathbf{Q}_b \cdot \hat{\mathbf{r}})\right] v_{42}(r)$$
$$+ \left(\hat{\mathbf{r}} \cdot \mathbf{Q}_a \cdot \hat{\mathbf{r}}\right)\left(\hat{\mathbf{r}} \cdot \mathbf{Q}_b \cdot \hat{\mathbf{r}}\right) v_{43}(r). \tag{2.39}$$

Note that the energies of multipoles on site b interacting with those on site a can be obtained by swapping indices along with the sign of the intersite vector, $\hat{\mathbf{r}}$.

2.3.1   Forces

The force on object a, $\mathbf{F}_a$, due to object b is the negative of the force on b due to a. For a simple charge-charge interaction, these forces will point along the $\pm\hat{\mathbf{r}}$ directions, where $\mathbf{r} = \mathbf{r}_b - \mathbf{r}_a$. Thus

$$F_{a\alpha} = \hat{r}_\alpha \frac{\partial U_{C_aC_b}}{\partial r} \quad \text{and} \quad F_{b\alpha} = -\hat{r}_\alpha \frac{\partial U_{C_aC_b}}{\partial r}. \tag{2.40}$$

TABLE 2.2: Radial functions used in the energy and torque equations. The $f, g, h, s, t,$ and u functions used in this table are defined in Appendices A.2 and A.3. The gradient shifted (GSF) functions include the shifted potential (SP) contributions (*cf.* Eqs. 2.22 and 2.24).

Generic	Bare Coulomb	Taylor-Shifted (TSF)	Shifted Potential (SP)	Gradient-Shifted (GSF)
$v_{01}(r)$	$\frac{1}{r}$	$f_0(r)$	$f(r) - f(r_c)$	$SP - (r - r_c)g(r_c)$
$v_{11}(r)$	$-\frac{1}{r^2}$	$g_1(r)$	$g(r) - g(r_c)$	$SP - (r - r_c)h(r_c)$
$v_{21}(r)$	$-\frac{1}{r^3}$	$\frac{g_2(r)}{r}$	$\frac{g(r)}{r} - \frac{g(r_c)}{r_c}$	$SP - (r - r_c)\left(-\frac{g(r_c)}{r_c^2} + \frac{h(r_c)}{r_c}\right)$
$v_{22}(r)$	$\frac{3}{r^3}$	$\left(-\frac{g_2(r)}{r} + h_2(r)\right)$	$\left(-\frac{g(r)}{r} + h(r)\right) - \left(-\frac{g(r_c)}{r_c} + h(r_c)\right)$	$SP - (r - r_c)\left(\frac{g(r_c)}{r_c^2} - \frac{h(r_c)}{r_c} + s(r_c)\right)$
$v_{31}(r)$	$\frac{3}{r^4}$	$\left(-\frac{g_3(r)}{r^2} + \frac{h_3(r)}{r}\right)$	$\left(-\frac{g(r)}{r^2} + \frac{h(r)}{r}\right) - \left(-\frac{g(r_c)}{r_c^2} + \frac{h(r_c)}{r_c}\right)$	$SP - (r - r_c)\left(\frac{2g(r_c)}{r_c^3} - \frac{2h(r_c)}{r_c^2} + \frac{s(r_c)}{r_c}\right)$
$v_{32}(r)$	$-\frac{15}{r^4}$	$\left(\frac{3g_3(r)}{r^2} - \frac{3h_3(r)}{r} + s_3(r)\right)$	$\left(\frac{3g(r)}{r^2} - \frac{3h(r)}{r} + s(r)\right) - \left(\frac{3g(r_c)}{r_c^2} - \frac{3h(r_c)}{r_c} + s(r_c)\right)$	$SP - (r - r_c)\left(-\frac{6g(r_c)}{r_c^3} + \frac{6h(r_c)}{r_c^2} - \frac{3s(r_c)}{r_c} + t(r_c)\right)$
$v_{41}(r)$	$\frac{3}{r^5}$	$\left(-\frac{g_4(r)}{r^3} + \frac{h_4(r)}{r^2}\right)$	$\left(-\frac{g(r)}{r^3} + \frac{h(r)}{r^2}\right) - \left(-\frac{g(r_c)}{r_c^3} + \frac{h(r_c)}{r_c^2}\right)$	$SP - (r - r_c)\left(\frac{3g(r_c)}{r_c^4} - \frac{3h(r_c)}{r_c^3} + \frac{s(r_c)}{r_c^2}\right)$
$v_{42}(r)$	$-\frac{15}{r^5}$	$\left(\frac{3g_4(r)}{r^3} - \frac{3h_4(r)}{r^2} + \frac{s_4(r)}{r}\right)$	$\left(\frac{3g(r)}{r^3} - \frac{3h(r)}{r^2} + \frac{s(r)}{r}\right) - \left(\frac{3g(r_c)}{r_c^3} - \frac{3h(r_c)}{r_c^2} + \frac{s(r_c)}{r_c}\right)$	$SP-(r - r_c)\left(-\frac{9g(r_c)}{r_c^4} + \frac{9h(r_c)}{r_c^3} - \frac{4s(r_c)}{r_c^2} + \frac{t(r_c)}{r_c}\right)$
$v_{43}(r)$	$\frac{105}{r^5}$	$\left(-\frac{15g_4(r)}{r^3} + \frac{15h_4(r)}{r^2} - \frac{6s_4(r)}{r} + t_4(r)\right)$	$\left(-\frac{15g(r)}{r^3} + \frac{15h(r)}{r^2} - \frac{6s(r)}{r} + t(r)\right)$ $- \left(-\frac{15g(r_c)}{r_c^3} + \frac{15h(r_c)}{r_c^2} - \frac{6s(r_c)}{r_c} + t(r_c)\right)$	$SP - (r - r_c)\left(\frac{45g(r_c)}{r_c^4} - \frac{45h(r_c)}{r_c^3} + \frac{21s(r_c)}{r_c^2} - \frac{6t(r_c)}{r_c} + u(r_c)\right)$

TABLE 2.3: Radial functions used in the force equations. Gradient shifted (GSF) functions are constructed using the shifted potential (SP) functions. Some of these functions are simple modifications of the functions found in table 2.2

Function	Definition	Taylor-Shifted (TSF)	Shifted Potential (SP)	Gradient-Shifted (GSF)
$w_a(r)$	$\frac{dv_{01}}{dr}$	$g_0(r)$	$g(r)$	SP $-g(r_c)$
$w_b(r)$	$\frac{dv_{11}}{dr} - \frac{v_{11}(r)}{r}$	$\left(-\frac{g_1(r)}{r} + h_1(r)\right)$	$h(r) - \frac{v_{11}(r)}{r}$	SP $-h(r_c)$
$w_c(r)$	$\frac{v_{11}(r)}{r}$	$\frac{g_1(r)}{r}$	$\frac{v_{11}(r)}{r}$	$\frac{v_{11}(r)}{r}$
$w_d(r)$	$\frac{dv_{21}}{dr}$	$\left(-\frac{g_2(r)}{r^2} + \frac{h_2(r)}{r}\right)$	$\left(-\frac{g(r)}{r^2} + \frac{h(r)}{r}\right)$	SP $-\left(-\frac{g(r_c)}{r_c^2} + \frac{h(r_c)}{r_c}\right)$
$w_e(r)$	$\frac{v_{22}(r)}{r}$	$\left(-\frac{g_2(r)}{r^2} + \frac{h_2(r)}{r}\right)$	$\frac{v_{22}(r)}{r}$	$\frac{v_{22}(r)}{r}$
$w_f(r)$	$\frac{dv_{22}}{dr} - \frac{2v_{22}(r)}{r}$	$\left(\frac{3g_2(r)}{r^2} - \frac{3h_2(r)}{r} + s_2(r)\right)$	$\left(\frac{g(r)}{r^2} - \frac{h(r)}{r} + s(r)\right) - \frac{2v_{22}(r)}{r}$	SP $-\left(\frac{g(r_c)}{r_c^2} - \frac{h(r_c)}{r_c} + s(r_c)\right)$
$w_g(r)$	$\frac{v_{31}(r)}{r}$	$\left(-\frac{g_3(r)}{r^3} + \frac{h_3(r)}{r^2}\right)$	$\frac{v_{31}(r)}{r}$	$\frac{v_{31}(r)}{r}$
$w_h(r)$	$\frac{dv_{31}}{dr} - \frac{v_{31}(r)}{r}$	$\left(\frac{3g_3(r)}{r^3} - \frac{3h_3(r)}{r^2} + \frac{s_3(r)}{r}\right)$	$\left(\frac{2g(r)}{r^3} - \frac{2h(r)}{r^2} + \frac{s(r)}{r}\right) - \frac{v_{31}(r)}{r}$	SP $-\left(\frac{2g(r_c)}{r_c^3} - \frac{2h(r_c)}{r_c^2} + \frac{s(r_c)}{r_c}\right)$
$w_i(r)$	$\frac{v_{32}(r)}{r}$	$\left(\frac{3g_3(r)}{r^3} - \frac{3h_3(r)}{r^2} + \frac{s_3(r)}{r}\right)$	$\frac{v_{32}(r)}{r}$	$\frac{v_{32}(r)}{r}$
$w_j(r)$	$\frac{dv_{32}}{dr} - \frac{3v_{32}}{r}$	$\left(\frac{-15g_3(r)}{r^3} + \frac{15h_3(r)}{r^2} - \frac{6s_3(r)}{r} + t_3(r)\right)$	$\left(\frac{-6g(r)}{r^3} + \frac{6h(r)}{r^2} - \frac{3s(r)}{r} + t(r)\right) - \frac{3v_{32}}{r}$	SP $-\left(\frac{-6g(r_c)}{r_c^3} + \frac{6h(r_c)}{r_c^2} - \frac{3s(r_c)}{r_c} + t(r_c)\right)$
$w_k(r)$	$\frac{dv_{41}}{dr}$	$\left(\frac{3g_4(r)}{r^4} - \frac{3h_4(r)}{r^3} + \frac{s_4(r)}{r^2}\right)$	$\left(\frac{3g(r)}{r^4} - \frac{3h(r)}{r^3} + \frac{s(r)}{r^2}\right)$	SP $-\left(\frac{3g(r_c)}{r_c^4} - \frac{3h(r_c)}{r_c^3} + \frac{s(r_c)}{r_c^2}\right)$
$w_l(r)$	$\frac{dv_{42}}{dr} - \frac{2v_{42}(r)}{r}$	$\left(-\frac{15g_4(r)}{r^4} + \frac{15h_4(r)}{r^3} - \frac{6s_4(r)}{r^2} + \frac{t_4(r)}{r}\right)$	$\left(-\frac{9g(r)}{r^4} + \frac{9h(r)}{r^3} - \frac{4s(r)}{r^2} + \frac{t(r)}{r}\right) - \frac{2v_{42}(r)}{r}$	SP $-\left(-\frac{9g(r_c)}{r_c^4} + \frac{9h(r_c)}{r_c^3} - \frac{4s(r_c)}{r_c^2} + \frac{t(r_c)}{r_c}\right)$
$w_m(r)$	$\frac{dv_{43}}{dr} - \frac{4v_{43}(r)}{r}$	$\left(\frac{105g_4(r)}{r^4} - \frac{105h_4(r)}{r^3} + \frac{45s_4(r)}{r^2} - \frac{10t_4(r)}{r} + u_4(r)\right)$	$\left(\frac{45g(r)}{r^4} - \frac{45h(r)}{r^3} + \frac{21s(r)}{r^2} - \frac{6t(r)}{r} + u(r)\right) - \frac{4v_{43}(r)}{r}$	SP $-\left(\frac{45g(r_c)}{r_c^4} - \frac{45h(r_c)}{r_c^3} + \frac{21s(r_c)}{r_c^2} - \frac{6t(r_c)}{r_c} + u(r_c)\right)$
$w_n(r)$	$\frac{v_{42}(r)}{r}$	$\left(\frac{3g_4(r)}{r^4} - \frac{3h_4(r)}{r^3} + \frac{s_4(r)}{r^2}\right)$	$\frac{v_{42}(r)}{r}$	$\frac{v_{42}(r)}{r}$
$w_o(r)$	$\frac{v_{43}(r)}{r}$	$\left(-\frac{15g_4(r)}{r^4} + \frac{15h_4(r)}{r^3} - \frac{6s_4(r)}{r^2} + \frac{t_4(r)}{r}\right)$	$\frac{v_{43}(r)}{r}$	$\frac{v_{43}(r)}{r}$

We list below the force equations written in terms of lab-frame coordinates. The radial functions used in the three methods are listed in Table 2.3

$$\mathbf{F}_{aC_aC_b} = C_a C_b w_a(r)\hat{\mathbf{r}} \tag{2.41}$$

$$\mathbf{F}_{aC_a\mathbf{D}_b} = C_a \left[(\hat{\mathbf{r}} \cdot \mathbf{D}_b)\, w_b(r)\hat{\mathbf{r}} + \mathbf{D}_b w_c(r) \right] \tag{2.42}$$

$$\mathbf{F}_{aC_a\mathbf{Q}_b} = C_a \left[\mathrm{Tr}\mathbf{Q}_b w_d(r)\hat{\mathbf{r}} + 2\mathbf{Q}_b \cdot \hat{\mathbf{r}} w_e(r) + (\hat{\mathbf{r}} \cdot \mathbf{Q}_b \cdot \hat{\mathbf{r}})\, w_f(r)\hat{\mathbf{r}} \right] \tag{2.43}$$

$$\mathbf{F}_{a\mathbf{D}_a\mathbf{D}_b} = -\mathbf{D}_a \cdot \mathbf{D}_b w_d(r)\hat{\mathbf{r}} + \left(\mathbf{D}_a \left(\mathbf{D}_b \cdot \hat{\mathbf{r}} \right) + \mathbf{D}_b \left(\mathbf{D}_a \cdot \hat{\mathbf{r}} \right) \right) w_e(r)$$
$$- (\hat{\mathbf{r}} \cdot \mathbf{D}_a)(\hat{\mathbf{r}} \cdot \mathbf{D}_b)\, w_f(r)\hat{\mathbf{r}} \tag{2.44}$$

$$\mathbf{F}_{a\mathbf{D}_a\mathbf{Q}_b} = -\left[\mathrm{Tr}\mathbf{Q}_b\mathbf{D}_a + 2\mathbf{D}_a \cdot \mathbf{Q}_b \right] w_g(r) - \left[\mathrm{Tr}\mathbf{Q}_b(\hat{\mathbf{r}} \cdot \mathbf{D}_a) + 2(\mathbf{D}_a \cdot \mathbf{Q}_b \cdot \hat{\mathbf{r}}) \right] w_h(r)\hat{\mathbf{r}}$$
$$- \left[\mathbf{D}_a(\hat{\mathbf{r}} \cdot \mathbf{Q}_b \cdot \hat{\mathbf{r}}) + 2(\hat{\mathbf{r}} \cdot \mathbf{D}_a)(\hat{\mathbf{r}} \cdot \mathbf{Q}_b) \right] w_i(r) - (\hat{\mathbf{r}} \cdot \mathbf{D}_a)(\hat{\mathbf{r}} \cdot \mathbf{Q}_b \cdot \hat{\mathbf{r}})w_j(r)\hat{\mathbf{r}}$$
$$\tag{2.45}$$

$$\mathbf{F}_{a\mathbf{Q}_a\mathbf{Q}_b} = \left[\mathrm{Tr}\mathbf{Q}_a\mathrm{Tr}\mathbf{Q}_b + 2\mathbf{Q}_a : \mathbf{Q}_b \right] w_k(r)\hat{\mathbf{r}}$$
$$+ \left[2\mathrm{Tr}\mathbf{Q}_b(\hat{\mathbf{r}} \cdot \mathbf{Q}_a) + 2\mathrm{Tr}\mathbf{Q}_a(\hat{\mathbf{r}} \cdot \mathbf{Q}_b) + 4(\mathbf{Q}_a \cdot \mathbf{Q}_b \cdot \hat{\mathbf{r}}) + 4(\hat{\mathbf{r}} \cdot \mathbf{Q}_a \cdot \mathbf{Q}_b) \right] w_n(r)$$
$$+ \left[\mathrm{Tr}\mathbf{Q}_a(\hat{\mathbf{r}} \cdot \mathbf{Q}_b \cdot \hat{\mathbf{r}}) + \mathrm{Tr}\mathbf{Q}_b(\hat{\mathbf{r}} \cdot \mathbf{Q}_a \cdot \hat{\mathbf{r}}) + 4(\hat{\mathbf{r}} \cdot \mathbf{Q}_a \cdot \mathbf{Q}_b \cdot \hat{\mathbf{r}}) \right] w_l(r)\hat{\mathbf{r}}$$
$$+ \left[+2(\hat{\mathbf{r}} \cdot \mathbf{Q}_a)(\hat{\mathbf{r}} \cdot \mathbf{Q}_b \cdot \hat{\mathbf{r}}) + 2(\hat{\mathbf{r}} \cdot \mathbf{Q}_a \cdot \hat{\mathbf{r}})(\hat{\mathbf{r}} \cdot \mathbf{Q}_b) \right] w_o(r)$$
$$+ (\hat{\mathbf{r}} \cdot \mathbf{Q}_a \cdot \hat{\mathbf{r}})(\hat{\mathbf{r}} \cdot \mathbf{Q}_b \cdot \hat{\mathbf{r}})w_m(r)\hat{\mathbf{r}}$$
$$\tag{2.46}$$

Note that the forces for higher multipoles on site a interacting with those of lower order on site b can be obtained by swapping indices in the expressions above.

2.3.2 Torques

The torques for the three methods are given in space-frame coordinates:

$$\tau_{bC_a\mathbf{D}_b} = C_a(\hat{\mathbf{r}} \times \mathbf{D}_b)v_{11}(r) \tag{2.47}$$

$$\tau_{bC_a\mathbf{Q}_b} = 2C_a\hat{\mathbf{r}} \times (\mathbf{Q}_b \cdot \hat{\mathbf{r}})v_{22}(r) \tag{2.48}$$

$$\tau_{a\mathbf{D}_a\mathbf{D}_b} = \mathbf{D}_a \times \mathbf{D}_b v_{21}(r) - (\hat{\mathbf{r}} \times \mathbf{D}_a)(\hat{\mathbf{r}} \cdot \mathbf{D}_b)v_{22}(r) \tag{2.49}$$

$$\tau_{a\mathbf{D}_a\mathbf{Q}_b} = \left[-\mathrm{Tr}\mathbf{Q}_b(\hat{\mathbf{r}} \times \mathbf{D}_a) + 2\mathbf{D}_a \times (\mathbf{Q}_b \cdot \hat{\mathbf{r}})\right]v_{31}(r) - (\hat{\mathbf{r}} \times \mathbf{D}_a)(\hat{\mathbf{r}} \cdot \mathbf{Q}_b \cdot \hat{\mathbf{r}})v_{32}(r) \tag{2.50}$$

$$\tau_{b\mathbf{D}_a\mathbf{Q}_b} = \left[+2(\mathbf{D}_a \cdot \mathbf{Q}_b) \times \hat{\mathbf{r}} - 2\mathbf{D}_a \times (\mathbf{Q}_b \cdot \hat{\mathbf{r}})\right]v_{31}(r) + (\hat{\mathbf{r}} \cdot \mathbf{D}_a)(\hat{\mathbf{r}} \cdot \mathbf{Q}_b) \times \hat{\mathbf{r}}v_{32}(r) \tag{2.51}$$

$$\begin{aligned}
\tau_{a\mathbf{Q}_a\mathbf{Q}_b} = &- 4\mathbf{Q}_a \times \mathbf{Q}_b v_{41}(r) \\
&+ \left[-2\mathrm{Tr}\mathbf{Q}_b(\hat{\mathbf{r}} \cdot \mathbf{Q}_a) \times \hat{\mathbf{r}} + 4\hat{\mathbf{r}} \times (\mathbf{Q}_a \cdot \mathbf{Q}_b \cdot \hat{\mathbf{r}}) - 4(\hat{\mathbf{r}} \cdot \mathbf{Q}_a) \times (\mathbf{Q}_b \cdot \hat{\mathbf{r}})\right]v_{42}(r) \\
&+ 2\hat{\mathbf{r}} \times (\mathbf{Q}_a \cdot \hat{\mathbf{r}})(\hat{\mathbf{r}} \cdot \mathbf{Q}_b \cdot \hat{\mathbf{r}})v_{43}(r)
\end{aligned} \tag{2.52}$$

$$\begin{aligned}
\tau_{b\mathbf{Q}_a\mathbf{Q}_b} = &4\mathbf{Q}_a \times \mathbf{Q}_b v_{41}(r) \\
&+ \left[-2\mathrm{Tr}\mathbf{Q}_a(\hat{\mathbf{r}} \cdot \mathbf{Q}_b) \times \hat{\mathbf{r}} - 4(\hat{\mathbf{r}} \cdot \mathbf{Q}_a \cdot \mathbf{Q}_b) \times \hat{\mathbf{r}} + 4(\hat{\mathbf{r}} \cdot \mathbf{Q}_a) \times (\mathbf{Q}_b \cdot \hat{\mathbf{r}})\right]v_{42}(r) \\
&+ 2(\hat{\mathbf{r}} \cdot \mathbf{Q}_a \cdot \hat{\mathbf{r}})\hat{\mathbf{r}} \times (\mathbf{Q}_b \cdot \hat{\mathbf{r}})v_{43}(r)
\end{aligned} \tag{2.53}$$

Here, we have defined the matrix cross product in an identical form as in Ref. [83]:

$$[\mathsf{A} \times \mathsf{B}]_\alpha = \sum_\beta [\mathsf{A}_{\alpha+1,\beta}\mathsf{B}_{\alpha+2,\beta} - \mathsf{A}_{\alpha+2,\beta}\mathsf{B}_{\alpha+1,\beta}] \tag{2.54}$$

where $\alpha + 1$ and $\alpha + 2$ are regarded as cyclic permuations of the matrix indices.

All of the radial functions required for torques are identical with the radial

functions previously computed for the interaction energies. These are tabulated for all three methods in table 2.2. The torques for higher multipoles on site a interacting with those of lower order on site b can be obtained by swapping indices in the expressions above.

2.4 Comparison to known multipolar energies

To understand how these new real-space multipole methods behave in computer simulations, it is vital to test against established methods for computing electrostatic interactions in periodic systems, and to evaluate the size and sources of any errors that arise from the real-space cutoffs. In this chapter we test SP, TSF, and GSF electrostatics against analytical methods for computing the energies of ordered multipolar arrays. In the following chapter, we test the new methods against the multipolar Ewald sum for computing the energies, forces and torques for a wide range of typical condensed-phase (disordered) systems.

Because long-range electrostatic effects can be significant in crystalline materials, ordered multipolar arrays present one of the biggest challenges for real-space cutoff methods. The dipolar analogues to the Madelung constants were first worked out by Sauer, who computed the energies of ordered dipole arrays of zero magnetization and obtained a number of these constants.[76] This theory was developed more completely by Luttinger and Tisza[49, 50] who tabulated energy constants for the Sauer arrays and other periodic structures.

To test the new electrostatic methods, we have constructed very large, $N = 16,000$ (bcc) arrays of dipoles in the orientations described in Ref. [49]. These structures include "A" lattices with nearest neighbor chains of antiparallel dipoles, as well as "B" lattices with nearest neighbor strings of antiparallel dipoles if the

dipoles are contained in a plane perpendicular to the dipole direction that passes through the dipole. We have also studied the minimum energy structure for the BCC lattice that was found by Luttinger & Tisza. The total electrostatic energy density for any of the arrays is given by:

$$E = CN^2\mu^2 \tag{2.55}$$

where C is the energy constant (equivalent to the Madelung constant), N is the number of dipoles per unit volume, and μ is the strength of the dipole. Energy constants (converged to 1 part in 10^9) are given in the supplemental information.[1]

For the purposes of testing the energy expressions and the self-neutralization schemes, the primary quantity of interest is the analytic energy constant for the perfect arrays. Convergence to these constants are shown as a function of the cutoff radius, r_c, for three different values of the damping coefficient, α in Fig.2.2. We have simultaneously tested a hard cutoff (where the kernel is simply truncated at the cutoff radius) in addition to the three new methods.

The hard cutoff exhibits oscillations around the analytic energy constants, and converges to incorrect energies when the complementary error function damping kernel is used. The shifted potential (SP) converges to the correct energy smoothly by $r_c = 4.5a$ even for the undamped case. This indicates that the shifting and the correction provided by the self term are required for obtaining accurate energies. The Taylor-shifted force (TSF) approximation appears to perturb the potential too much inside the cutoff region to provide accurate measures of the energy constants. GSF is a compromise, converging to the correct energies within $r_c = 6a$.

Quadrupolar analogues to the Madelung constants were first worked out by
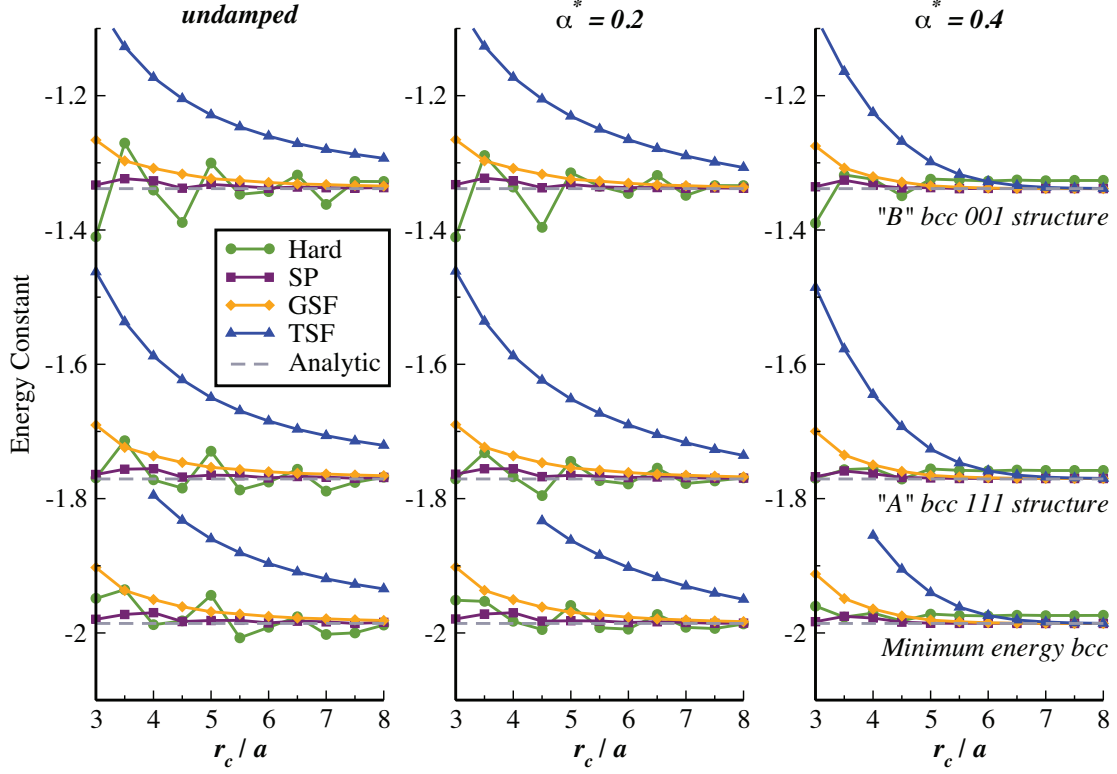
Figure 2.2. Convergence of the lattice energy constants as a function of cutoff radius (normalized by the lattice constant, a) for the new real-space methods. Three dipolar crystal structures were sampled, and the analytic energy constants for the three lattices are indicated with grey dashed lines. The left panel shows results for the undamped kernel $(1/r)$, while the damped kernel, $B_0(r)$ was used in the center and right panels.

Nagai and Nakamura who computed the energies of selected quadrupole arrays based on extensions to the Luttinger and Tisza approach.[58, 59]

In analogy to the dipolar arrays, the total electrostatic energy for the quadrupolar arrays is:

$$E = CN \frac{3\bar{Q}^2}{4a^5} \tag{2.56}$$

where a is the lattice parameter, and $\bar{Q}$ is the effective quadrupole moment,

$$\bar{Q}^2 = 2 \left(3\mathbf{Q} : \mathbf{Q} - (\mathrm{Tr}\mathbf{Q})^2 \right) \tag{2.57}$$

for the primitive quadrupole as defined in Eq. B.3. (For the traceless quadrupole tensor, $\Theta = 3\mathbf{Q} - \mathrm{Tr}\mathbf{Q}$, the effective moment, $\bar{Q}^2 = \frac{2}{3}\Theta : \Theta$.)

To test the new electrostatic methods for quadrupoles, we have constructed very large, $N = 8{,}000$ (sc), 16,000 (bcc), and 32,000 (fcc) arrays of linear quadrupoles in the orientations described in Ref. [58]. We have compared the energy constants for these low-energy configurations for linear quadrupoles. Convergence to these constants are shown as a function of the cutoff radius, r_c, for three different values of the damping parameter, α in Fig. 2.3.

Again, we find that the hard cutoff exhibits oscillations around the analytic energy constants. The shifted potential (SP) approximation converges to the correct energy smoothly by $r_c = 3a$ even for the undamped case. The Taylor-shifted force (TSF) approximation again appears to perturb the potential too much inside the cutoff region to provide accurate measures of the energy constants. GSF again provides a compromise between the two methods – energies are converged by $r_c = 4.5a$, and the approximation is not as perturbative at short range as TSF.

It is also useful to understand the behavior of the lattice energy constants
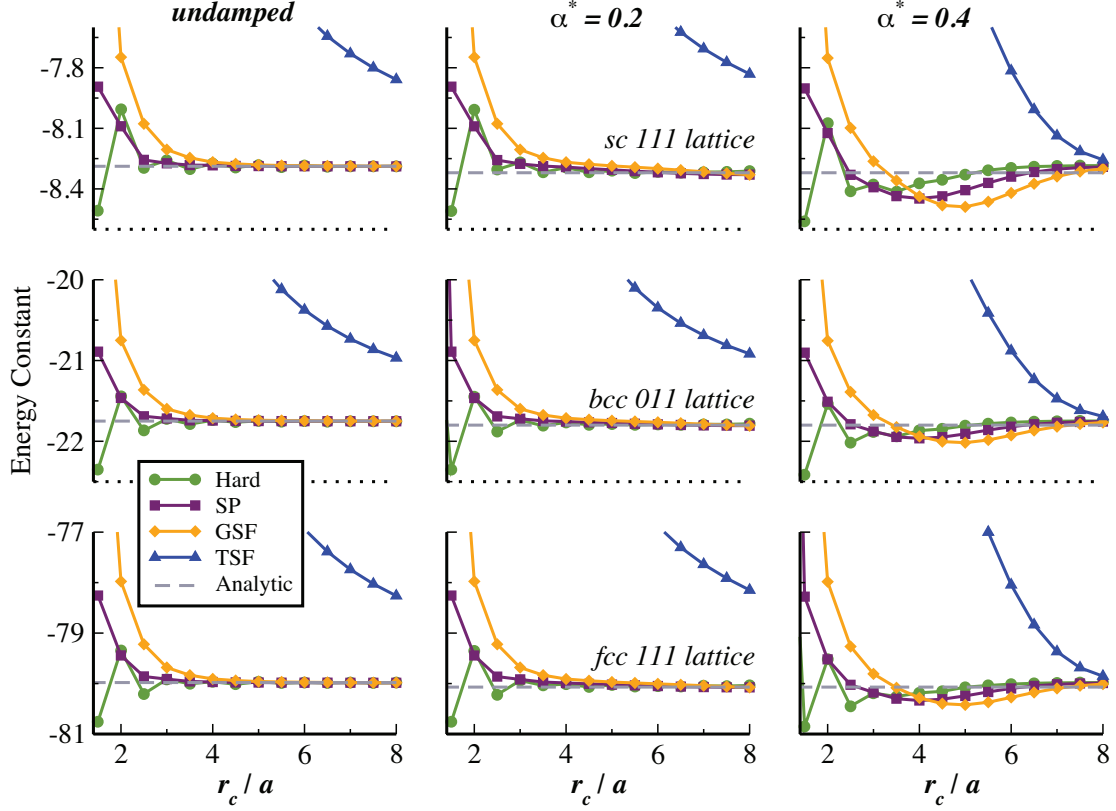
Figure 2.3. Convergence of the lattice energy constants as a function of cutoff radius (normalized by the lattice constant, a) for the new real-space methods. Three quadrupolar crystal structures were sampled, and the analytic energy constants for the three lattices are indicated with grey dashed lines. The left panel shows results for the undamped kernel $(1/r)$, while the damped kernel, $B_0(r)$ was used in the center and right panels. Note that for quadrupoles, $\alpha^* = 0.4$ overdamps contributions from repulsive orientations in the perfect crystal.

for different values of the reduced damping parameter ($\alpha^* = \alpha a$) for the real-space methods. All of the methods (except for TSF) have excellent behavior for the undamped or weakly-damped cases. Overdamping can cause problems in perfect crystals for the quadrupoles in particular (*cf.* the right panel in Fig. 2.3). In the perfect crystals, only a few orientations are being sampled. E.g. in the simple cubic (SC) lattice of linear quadrupoles aligned in the 111 direction, the nearest-neighbor quadrupoles only sample 3 distinct orientations relative to the vector between the sites. The damping alters the radial function for the direct quadrupolar contraction, $v_{41}(r)$, differently than the radial functions for the terms involving the product of the separation vector with the quadrupoles, $v_{42}(r)$ and $v_{43}(r)$. Because these terms are altered by different amounts by the complementary error function damping, the effect of damping is non-spherical for multipoles, and the balance between attractive and repulsive interactions in the crystal is therefore altered significantly in overdamped situations.

In the chapter 3, we discuss how large values of α can perturb the force and torque vectors, but weakly-damped electrostatics appear to generate reasonable values for the total electrostatic energies under both the SP and GSF approximations. We also discuss the effects that α can have on convergence to the average electrostatic energies in liquids (which sample a much wider range of local orientations).

2.5 Summary

We have presented three efficient real-space methods for computing the interactions between point multipoles. One of these (SP) is a multipolar generalization of Wolf's method that smoothly shifts electrostatic energies to zero at the cutoff

radius. Two of these methods (GSF and TSF) also smoothly truncate the forces and torques (in addition to the energies) at the cutoff radius, making them attractive for both molecular dynamics and Monte Carlo simulations. We find that the Gradient-Shifted Force (GSF) and the Shifted-Potential (SP) methods converge rapidly to the correct lattice energies for ordered dipolar and quadrupolar arrays, while the Taylor-Shifted Force (TSF) is too severe an approximation to provide convergence to lattice energies within reasonable cutoff radii.

Although the TSF method appears to perform poorly for the analytical energy constants, the structure of the radial functions used in the force and torque expressions in the other two methods would not have been revealed without first developing the TSF approach. TSF also generates a set of electrostatic kernels that have multiple derivatives that vanish at the cutoff radius, a property that is valuable in estimating dielectric constants using the conducting boundary fluctuation formula.[37]

In most cases, GSF can obtain nearly quantitative agreement with the lattice energy constants with reasonably small cutoff radii. The only exception we have observed is for crystals which exhibit a bulk macroscopic dipole moment (e.g. Luttinger & Tisza's Z_1 lattice). In this particular case, the multipole neutralization scheme can interfere with the correct computation of the energies. We note that the energies for these arrangements are typically much larger than for crystals with net-zero moments, so this is not expected to be an issue in most simulations.

Relatively weak damping is sufficient to converge to the analytical energy constants within moderately short cutoff distances. Because overdamping can present additional issues with higher order multipoles, our results indicate that the damping coefficient should be taken as small as possible, and that the *undamped* GSF

and SP methods may be the best choice in crystalline systems.

The techniques used here to derive the force, torque and energy expressions can be extended to higher order multipoles, although some of the objects (e.g. the matrix cross product in Eq. B.10) will need to be generalized for higher-rank tensors. We also note that the definitions of the multipoles used here are in a primitive form, and these need some care when comparing with experiment or other computational techniques.

In large systems, these new methods can be made to scale approximately linearly with system size, and detailed comparisons with the Ewald sum for a wide range of chemical environments follows in the chapter 3.

CHAPTER 3

COMPARISONS WITH THE EWALD SUM

We have briefly discussed the short-ranged nature of the electrostatic interaction in the crystalline environment. In this chapter we discuss this property in more detail and extend this idea for the case of liquid simulation. We also compare energies, forces and torques calculated using real-space methods with the result obtained from the Ewald sum. Additionally we derive different static and dynamic properties using newly developed real-space method and compare result with the Ewald sum. Finally we test the conservation of total energy in the molecular dynamics simulation using various real-space as well as Ewald method.

3.1 Introduction

As I mentioned earlier Wolf *et al.*[95] proposed a real space $O(N)$ method for calculating electrostatic interactions between point charges. They argued that the effective Coulomb interaction in most condensed phase systems is effectively short ranged.[93, 94] For an ordered lattice (e.g., when computing the Madelung constant of an ionic solid), the material can be considered as a set of ions interacting with neutral dipolar or quadrupolar "molecules" giving an effective distance dependence for the electrostatic interactions of r^{-5} (see figure 3.1). If one views the NaCl crystal as a simple cubic (SC) structure with an octupolar (NaCl)4 basis, the

electrostatic energy per ion converges more rapidly to the Madelung energy than the dipolar approximation.[93] To find the correct Madelung constant, Lacman suggested that the NaCl structure could be constructed in a way that the finite crystal terminates with complete (NaCl)4 molecules.[?] The central ion sees what is effectively a set of octupoles at large distances. These facts suggest that the Madelung constants are relatively short ranged for perfect ionic crystals.[95] For this reason, careful application of Wolf's method can provide accurate estimates of Madelung constants using relatively short cutoff radii.

Direct truncation of interactions at a cutoff radius creates numerical errors. Wolf *et al.* suggest that truncation errors are due to net charge remaining inside the cutoff sphere.[95] To neutralize this charge they proposed placing an image charge on the surface of the cutoff sphere for every real charge inside the cutoff sphere. These charges are present for the evaluation of both the pair interaction energy and the force, although the force expression maintains a discontinuity at the cutoff sphere. In the original Wolf formulation, the total energy for the charge and image were not equal to the integral of the force expression, and as a result, the total energy would not be conserved in molecular dynamics (MD) simulations.[18] Zahn *et al.*, and Fennell and Gezelter later proposed shifted force variants of the Wolf method with commensurate force and energy expressions that do not exhibit this problem.[23?] Related real-space methods were also proposed by Chen *et al.* [11, 12, 17, 74] and by Wu and Brooks.[96] Recently, Fukuda has successfully used additional neutralization of higher order moments for systems of point charges.[25]

One can make a similar effective range argument for crystals of point *multipoles*. The Luttinger and Tisza treatment of energy constants for dipolar lattices utilizes 24 basis vectors that contain dipoles at the eight corners of a unit cube.[49]
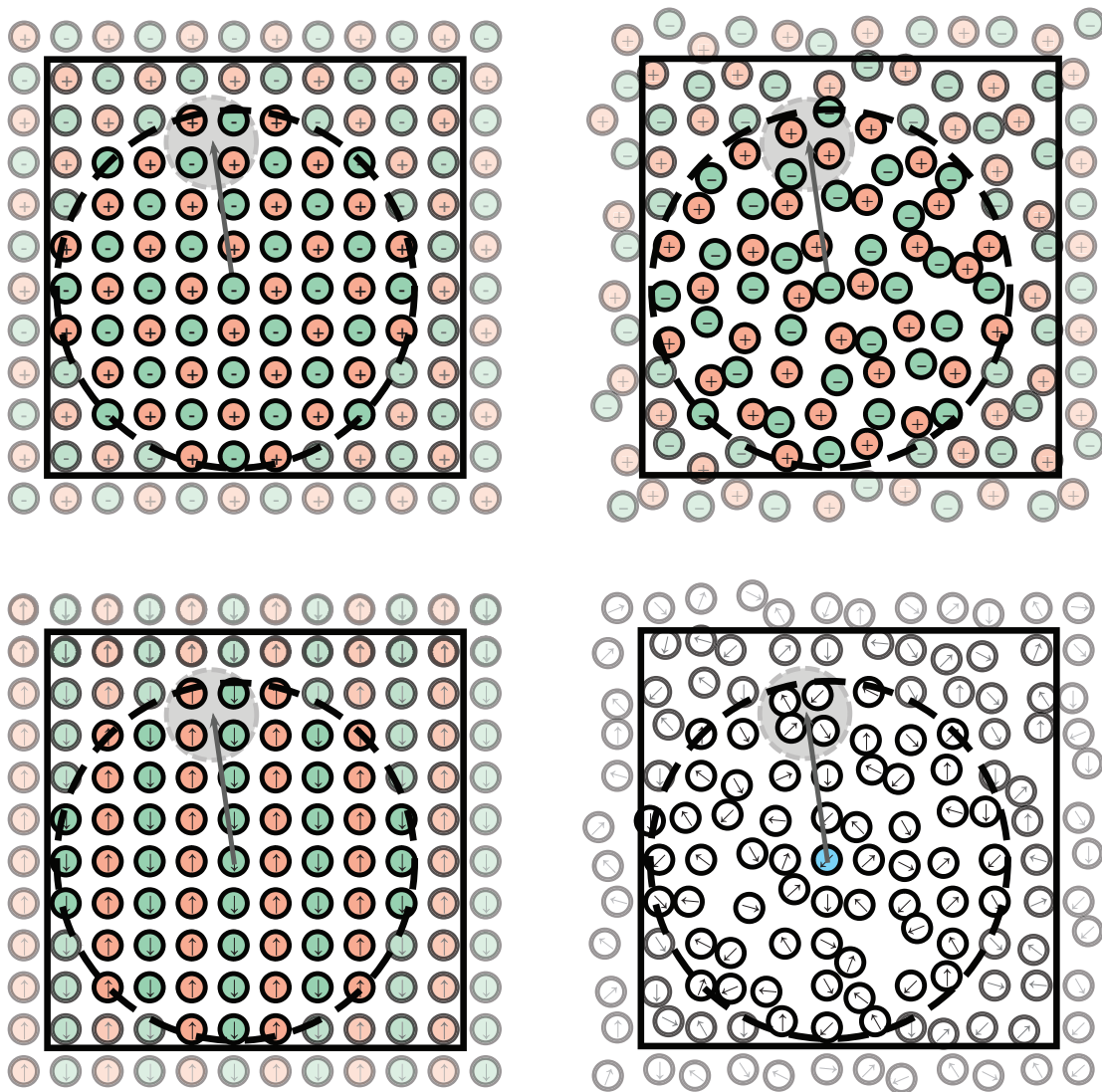
Figure 3.1. Top: Ionic systems exhibit local clustering of dissimilar charges (in the smaller grey circle), so interactions are effectively charge-multipole at longer distances. With hard cutoffs, motion of individual charges in and out of the cutoff sphere can break the effective multipolar ordering. Bottom: dipolar crystals and fluids have a similar effective *quadrupolar* ordering (in the smaller grey circles), and orientational averaging helps to reduce the effective range of the interactions in the fluid. Placement of reversed image multipoles on the surface of the cutoff sphere recovers the effective higher-order multipole behavior.

Only three of these basis vectors, $X_1, Y_1,$ and Z_1, retain net dipole moments, while the rest have zero net dipole and retain contributions only from higher order multipoles. The lowest-energy crystalline structures are built out of basis vectors that have only residual quadrupolar moments (e.g. the Z_5 array). In these low energy structures, the effective interaction between a dipole at the center of a crystal and a group of eight dipoles farther away is significantly shorter ranged than the r^{-3} that one would expect for raw dipole-dipole interactions. Only in crystals which retain a bulk dipole moment (e.g. ferroelectrics) does the analogy with the ionic crystal break down – ferroelectric dipolar crystals can exist, while ionic crystals with net charge in each unit cell would be unstable.

In ionic crystals, real-space truncation can break the effective multipolar arrangements (see Fig. 3.1), causing significant swings in the electrostatic energy as individual ions move back and forth across the boundary. This is why the image charges are necessary for the Wolf sum to exhibit rapid convergence. Similarly, the real-space truncation of point multipole interactions breaks higher order multipole arrangements, and image multipoles are required for real-space treatments of electrostatic energies.

The shorter effective range of electrostatic interactions is not limited to perfect crystals, but can also apply in disordered fluids. Even at elevated temperatures, there is local charge balance in an ionic liquid, where each positive ion has surroundings dominated by negative ions and vice versa. The reversed-charge images on the cutoff sphere that are integral to the Wolf and damped shifted force (DSF) approaches retain the effective multipolar interactions as the charges traverse the cutoff boundary.

In multipolar fluids (see Fig. 3.1) there is significant orientational averaging

57

that additionally reduces the effect of long-range multipolar interactions. The image multipoles that are introduced in the Taylor shifted force (TSF), gradient shifted force (GSF), and shifted potential (SP) methods mimic this effect and reduce the effective range of the multipolar interactions as interacting molecules traverse each other's cutoff boundaries.

Forces and torques acting on atomic sites are fundamental in driving dynamics in molecular simulations, and the DSF energy kernel provides consistent energies and forces on charged atoms within the cutoff sphere. Both the energy and the force go smoothly to zero as an atom approaches the cutoff radius. The comparisons of the accuracy these quantities between the DSF kernel and SPME was surprisingly good.[23] As a result, the DSF method has seen increasing use in molecular systems with relatively uniform charge densities. [20, 24, 48, 56, 78, 89?]

3.2 Methodology

To understand how the real-space multipole methods behave in computer simulations, it is vital to test against established methods for computing electrostatic interactions in periodic systems, and to evaluate the size and sources of any errors that arise from the real-space cutoffs. In the chapter 2 of this series, we compared the dipolar and quadrupolar energy expressions against analytic expressions for ordered dipolar and quadrupolar arrays.[49, 58, 59, 76] In this work, we used the multipolar Ewald sum as a reference method for comparing energies, forces, and torques for molecular models that mimic disordered and ordered condensed-phase systems. The parameters used in the test cases are given in table 3.1.

The systems consist of pure multipolar solids (both dipole and quadrupole),

TABLE 3.1: The parameters used in the systems used to evaluate the new real-space methods. The most comprehensive test was a liquid composed of 2000 soft DQ liquid molecules with 48 dissolved ions (24 Na+ and 24 Cl- ions). This test exercises all orders of the multipolar interactions developed in the chapter 2.

Test system	LJ parameters		C	Electrostatic moments				mass	I_{xx}	I_{yy}	I_{zz}
	σ (Å)	ϵ (kcal/mol)	(e)	D (debye)	Q_{xx}	Q_{yy} (debye Å)	Q_{zz}	(amu)		(amu Å^2)	
Soft Dipolar fluid	3.051	0.152		2.35				18.0153	1.77	0.6145	1.155
Soft Dipolar solid	2.837	1.0		2.35				10^4	17.6	17.6	0
Soft Quadrupolar fluid	3.051	0.152			-1	-1	-2.5	18.0153	1.77	0.6145	1.155
Soft Quadrupolar solid	2.837	1.0			-1	-1	-2.5	10^4	17.6	17.6	0
Soft DQ liquid	3.051	0.152		2.35	-1.35	0	-0.68	18.0153	1.77	0.6145	1.155
Na+	2.579	0.118	+1					22.99			
Cl-	4.445	0.1	-1					35.4527			

pure multipolar liquids (both dipole and quadrupole), a fluid composed of sites containing both dipoles and quadrupoles simultaneously, and a final test case that includes ions with point charges in addition to the multipolar fluid. The solid-phase parameters were chosen so that the systems can explore some orientational freedom for the multipolar sites, while maintaining relatively strict translational order. The soft DQ liquid model used here based loosely on the SSDQO water model,[14, 86, 87] but is not itself a particularly accurate water model. However, the soft DQ model does test dipole-dipole, dipole-quadrupole, and quadrupole-quadrupole interactions at roughly the same magnitudes. The last test case, a soft DQ liquid with dissolved ions, exercises *all* levels of the multipole-multipole interactions we have derived so far and represents the most complete test of the new methods.

In the following section, we present results for the total electrostatic energy, as well as the electrostatic contributions to the force and torque on each molecule. These quantities have been computed using the SP, TSF, and GSF methods, as well as a hard cutoff, and have been compared with the values obtained from the multipolar Ewald sum. In Monte Carlo (MC) simulations, the energy differences between two configurations is the primary quantity that governs how the simulation proceeds. These differences are the most important indicators of the reliability of a method even if the absolute energies are not exact. For each of the multipolar systems listed above, we have compared the change in electrostatic potential energy (ΔE) between 250 statistically-independent configurations. In molecular dynamics (MD) simulations, the forces and torques govern the behavior of the simulation, so we also compute the electrostatic contributions to the forces and torques.

3.2.1 Implementation

The real-space methods developed in the chapter 2 in this series have been implemented in our group's open source molecular simulation program, OpenMD,[?] which was used for all calculations in this work. The complementary error function can be a relatively slow function on some processors, so all of the radial functions are precomputed on a fine grid and are spline-interpolated to provide values when required.

Using the same simulation code, we compare to a multipolar Ewald sum with a reciprocal space cutoff, $k_{max} = 7$. Our version of the Ewald sum is a re-implementation of the algorithm originally proposed by Smith that does not use the particle mesh or smoothing approximations.[82, 83] This implementation was tested extensively against the analytic energy constants for the multipolar lattices that are discussed in reference [?]. In all cases discussed below, the quantities being compared are the electrostatic contributions to energies, force, and torques. All other contributions to these quantities (i.e. from Lennard-Jones interactions) are removed prior to the comparisons.

The convergence parameter (α) also plays a role in the balance of the real-space and reciprocal-space portions of the Ewald calculation. Typical molecular mechanics packages set this to a value that depends on the cutoff radius and a tolerance (typically less than 1×10^{-4} kcal/mol). Smaller tolerances are typically associated with increasing accuracy at the expense of computational time spent on the reciprocal-space portion of the summation.[22, 67] A default tolerance of 1×10^{-8} kcal/mol was used in all Ewald calculations, resulting in Ewald coefficient 0.3119 Å^{-1} for a cutoff radius of 12 Å.

The real-space models have self-interactions that provide contributions to the

energies only. Although the self interaction is a rapid calculation, we note that in systems with fluctuating charges or point polarizabilities, the self-term is not static and must be recomputed at each time step.

3.2.2 Model systems

To sample independent configurations of the multipolar crystals, body centered cubic (bcc) crystals, which exhibit the minimum energy structures for point dipoles, were generated using 3,456 molecules. The multipoles were translationally locked in their respective crystal sites for equilibration at a relatively low temperature (50K) so that dipoles or quadrupoles could freely explore all accessible orientations. The translational constraints were then removed, the systems were re-equilibrated, and the crystals were simulated for an additional 10 ps in the microcanonical (NVE) ensemble with an average temperature of 50 K. The balance between moments of inertia and particle mass were chosen to allow orientational sampling without significant translational motion. Configurations were sampled at equal time intervals in order to compare configurational energy differences. The crystals were simulated far from the melting point in order to avoid translational deformation away of the ideal lattice geometry.

For dipolar, quadrupolar, and mixed-multipole *liquid* simulations, each system was created with 2,048 randomly-oriented molecules. These were equilibrated at a temperature of 300K for 1 ns. Each system was then simulated for 1 ns in the microcanonical (NVE) ensemble with the Dullweber, Leimkuhler, and McLachlan (DLM) symplectic splitting integrator using 1 fs timesteps.[19] We collected 250 different configurations at equal time intervals. For the liquid system that included ionic species, we converted 48 randomly-distributed molecules into 24 Na+ and

24 Cl- ions and re-equilibrated. After equilibration, the system was run under the same conditions for 1 ns. A total of 250 configurations were collected. In the following comparisons of energies, forces, and torques, the Lennard-Jones potentials were turned off and only the purely electrostatic quantities were compared with the same values obtained via the Ewald sum.

3.2.3 Accuracy of Energy Differences, Forces and Torques

The pairwise summation techniques (outlined above) were evaluated for use in MC simulations by studying the energy differences between different configurations. We took the Ewald-computed energy difference between two conformations to be the correct behavior. An ideal performance by one of the new methods would reproduce these energy differences exactly. The configurational energies being used here contain only contributions from electrostatic interactions. Lennard-Jones interactions were omitted from the comparison as they should be identical for all methods.

Since none of the real-space methods provide exact energy differences, we used least square regressions analysis for the six different molecular systems to compare ΔE from Hard, SP, GSF, and TSF with the multipolar Ewald reference method. A result of unity for both the correlation (slope) and coefficient of determination (R^2) for these regressions would indicate perfect agreement between the real-space method and the multipolar Ewald sum.

Molecular systems were run long enough to explore independent configurations and 250 configurations were recorded for comparison. Each system provided 31,125 energy differences for a total of 186,750 data points. Similarly, the magnitudes of the forces and torques have also been compared using least squares

regression analysis. In the forces and torques comparison, the magnitudes of the forces acting in each molecule for each configuration were evaluated. For example, our dipolar liquid simulation contains 2048 molecules and there are 250 different configurations for each system resulting in 3,072,000 data points for comparison of forces and torques.

3.2.4   Analysis of vector quantities

Getting the magnitudes of the force and torque vectors correct is only part of the issue for carrying out accurate molecular dynamics simulations. Because the real space methods reweight the different orientational contributions to the energies, it is also important to understand how the methods impact the *directionality* of the force and torque vectors. Fisher developed a probability density function to analyse directional data sets,

$$p_f(\theta) = \frac{\kappa}{2\sinh\kappa} \sin\theta e^{\kappa\cos\theta} \tag{3.1}$$

where κ measures directional dispersion of the data around the mean direction.[?] This quantity (κ) can be estimated as a reciprocal of the circular variance.[?] To quantify the directional error, forces obtained from the Ewald sum were taken as the mean (or correct) direction and the angle between the forces obtained via the Ewald sum and the real-space methods were evaluated,

$$\cos\theta_i = \frac{\mathbf{f}_i^{\text{Ewald}} \cdot \mathbf{f}_i^{\text{GSF}}}{\left|\mathbf{f}_i^{\text{Ewald}}\right| \left|\mathbf{f}_i^{\text{GSF}}\right|} \tag{3.2}$$

The total angular displacement of the vectors was calculated as,

$$R = \sqrt{\left(\sum_{i=1}^{N} \cos\theta_i\right)^2 + \left(\sum_{i=1}^{N} \sin\theta_i\right)^2} \tag{3.3}$$

where N is number of force vectors. The circular variance is defined as

$$\text{Var}(\theta) \approx 1/\kappa = 1 - R/N \tag{3.4}$$

The circular variance takes on values between from 0 to 1, with 0 indicating a perfect directional match between the Ewald force vectors and the real-space forces. Lower values of $\text{Var}(\theta)$ correspond to higher values of κ, which indicates tighter clustering of the real-space force vectors around the Ewald forces.

A similar analysis was carried out for the electrostatic contribution to the molecular torques as well as forces.

3.2.5 Energy conservation

To test conservation the energy for the methods, the mixed molecular system of 2000 soft DQ liquid molecules with 24 Na+ and 24 Cl- ions was run for 1 ns in the microcanonical ensemble at an average temperature of 300K. Each of the different electrostatic methods (Ewald, Hard, SP, GSF, and TSF) was tested for a range of different damping values. The molecular system was started with same initial positions and velocities for all cutoff methods. The energy drift (δE_1) and standard deviation of the energy about the slope (δE_0) were evaluated from the total energy of the system as a function of time. Although both measures are valuable at investigating new methods for molecular dynamics, a useful interaction model must allow for long simulation times with minimal energy drift.

3.3 Results

3.3.1 Configurational energy differences

The combined coefficient of determination and slope for all six systems is shown in Figure 3.2. Most of the methods reproduce the Ewald configurational energy differences with remarkable fidelity. Undamped hard cutoffs introduce a significant amount of random scatter in the energy differences which is apparent in the reduced value of R^2 for this method. This can be easily understood as configurations which exhibit small traversals of a few dipoles or quadrupoles out of the cutoff sphere will see large energy jumps when hard cutoffs are used. The orientations of the multipoles (particularly in the ordered crystals) mean that these energy jumps can go in either direction, producing a significant amount of random scatter, but no systematic error.

The TSF method produces energy differences that are highly correlated with the Ewald results, but it also introduces a significant systematic bias in the values of the energies, particularly for smaller cutoff values. The TSF method alters the distance dependence of different orientational contributions to the energy in a non-uniform way, so the size of the cutoff sphere can have a large effect, particularly for the crystalline systems.

Both the SP and GSF methods appear to reproduce the Ewald results with excellent fidelity, particularly for moderate damping ($\alpha \approx 0.2$ Å^{-1}) and with a commonly-used cutoff value ($r_c = 12$ Å). With the exception of the undamped hard cutoff, and the TSF method with short cutoffs, all of the methods would be appropriate for use in Monte Carlo simulations.

Method   α   Correlation (slope)   Coeff. of Determination (R^2)

              0.8   0.85   0.9   0.95   1   0.94   0.96   0.98   1

Hard

0.0   1.001   0.9703
        0.9942   0.9765
        0.9986   0.9693

0.1   0.9944   0.9974
        0.9975   0.9993
        0.9985   0.9997

0.2   0.9947   0.9989
        0.9988   0.999
        0.9991   0.999

0.3   1.01   0.998
        1.011   0.998
        1.011   0.998

SP

0.0   0.9935   0.9983
        0.9976   0.9991
        0.9989   0.9997

0.1   0.9936   0.9986
        0.9973   0.9995
        0.9985   0.9997

0.2   0.9953   0.9988
        0.9987   0.999
        0.9992   0.999

0.3   1.01   0.998
        1.011   0.998
        1.011   0.998

GSF

0.0   0.9804   0.9966
        0.9931   0.9988
        0.9966   0.9993

0.1   0.9804   0.9966
        0.9933   0.9989
        0.9968   0.9995

0.2   0.9829   0.9982
        0.9963   0.9989
        0.999   0.999

0.3   1.006   0.998
        1.011   0.998
        0.9978   0.998

TSF

0.0   0.8864   0.9951
        0.9378   0.998
        0.9607   0.999

0.1   0.8861   0.9951
        0.9368   0.998
        0.959   0.999

0.2   0.8826   0.995
        0.9613   0.9985
        0.9936   0.999

0.3   0.9719   0.9976
        1.01   0.998
        1.011   0.998

Figure 3.2. Statistical analysis of the quality of configurational energy differences for the real-space electrostatic methods compared with the reference Ewald sum. Results with a value equal to 1 (dashed line) indicate ΔE values indistinguishable from those obtained using the multipolar Ewald sum. Different values of the cutoff radius are indicated with different symbols (9 Å = circles, 12 Å = squares, and 15 Å = inverted triangles).

67

3.3.2 Magnitude of the force and torque vectors

The comparisons of the magnitudes of the forces and torques for the data accumulated from all six systems are shown in Figures 3.3 and 3.4. The correlation and slope for the forces agree well with the Ewald sum even for the hard cutoffs.

For systems of molecules with only multipolar interactions, the pair energy contributions are quite short ranged. Moreover, the force decays more rapidly than the electrostatic energy, hence the hard cutoff method can also produce reasonable agreement for this quantity. Although the pure cutoff gives reasonably good electrostatic forces for pairs of molecules included within each other's cutoff spheres, the discontinuity in the force at the cutoff radius can potentially cause energy conservation problems as molecules enter and leave the cutoff spheres. This is discussed in detail in section 3.3.4.

The two shifted-force methods (GSF and TSF) exhibit a small amount of systematic variation and scatter compared with the Ewald forces. The shifted-force models intentionally perturb the forces between pairs of molecules inside each other's cutoff spheres in order to correct the energy conservation issues, and this perturbation is evident in the statistics accumulated for the molecular forces. The GSF perturbations are minimal, particularly for moderate damping and commonly-used cutoff values ($r_c = 12$ Å). The TSF method shows reasonable agreement in R^2, but again the systematic error in the forces is concerning if replication of Ewald forces is desired.

It is important to note that the forces and torques from the SP and the Hard cutoffs are not identical. The SP method shifts each orientational contribution separately (e.g. the dipole-dipole dot product is shifted by a different function than the dipole-distance products), while the hard cutoff contains no orientation-

dependent shifting. The forces and torques for these methods therefore diverge for multipoles even though the forces for point charges are identical.

The torques (Fig. 3.4) appear to be significantly influenced by the choice of real-space method. The torque expressions have the same distance dependence as the energies, which are naturally longer-ranged expressions than the inter-site forces. Torques are also quite sensitive to orientations of neighboring molecules, even those that are near the cutoff distance.

The results shows that the torque from the hard cutoff method reproduces the torques in quite good agreement with the Ewald sum. The other real-space methods can cause some deviations, but excellent agreement with the Ewald sum torques is recovered at moderate values of the damping coefficient ($\alpha \approx 0.2$ Å^{-1}) and cutoff radius ($r_c \geq 12$ Å). The TSF method exhibits only fair agreement in the slope when compared with the Ewald torques even for larger cutoff radii. It appears that the severity of the perturbations in the TSF method are most in evidence for the torques.

3.3.3 Directionality of the force and torque vectors

The accurate evaluation of force and torque directions is just as important for molecular dynamics simulations as the magnitudes of these quantities. Force and torque vectors for all six systems were analyzed using Fisher statistics, and the quality of the vector directionality is shown in terms of circular variance ($\mathrm{Var}(\theta)$) in Fig. 3.5. The force and torque vectors from the new real-space methods exhibit nearly-ideal Fisher probability distributions (Eq. 3.1). Both the hard and SP cutoff methods exhibit the best vectorial agreement with the Ewald sum. The force and torque vectors from GSF method also show good agreement with the
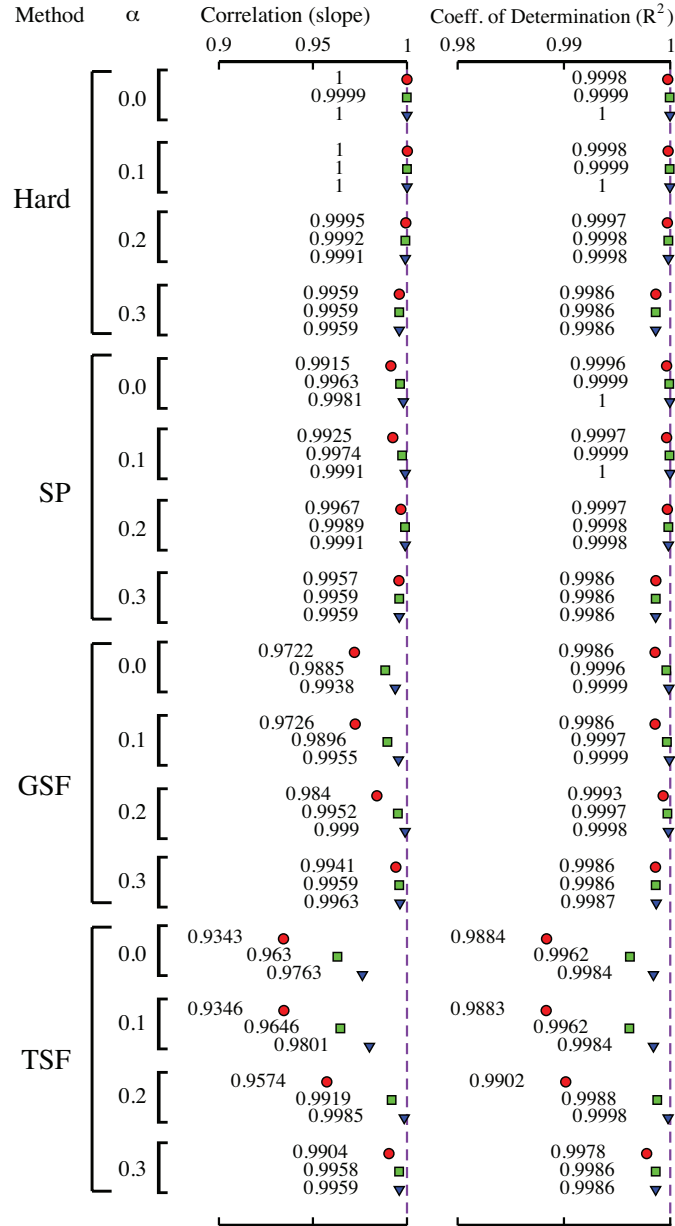
Figure 3.3. Statistical analysis of the quality of the force vector magnitudes for the real-space electrostatic methods compared with the reference Ewald sum. Results with a value equal to 1 (dashed line) indicate force magnitude values indistinguishable from those obtained using the multipolar Ewald sum. Different values of the cutoff radius are indicated with different symbols (9 Å = circles, 12 Å = squares, and 15 Å = inverted triangles).

Method	α	Correlation (slope)		Coeff. of Determination (R²)
		0.9 0.95 1		0.96 0.97 0.98 0.99 1
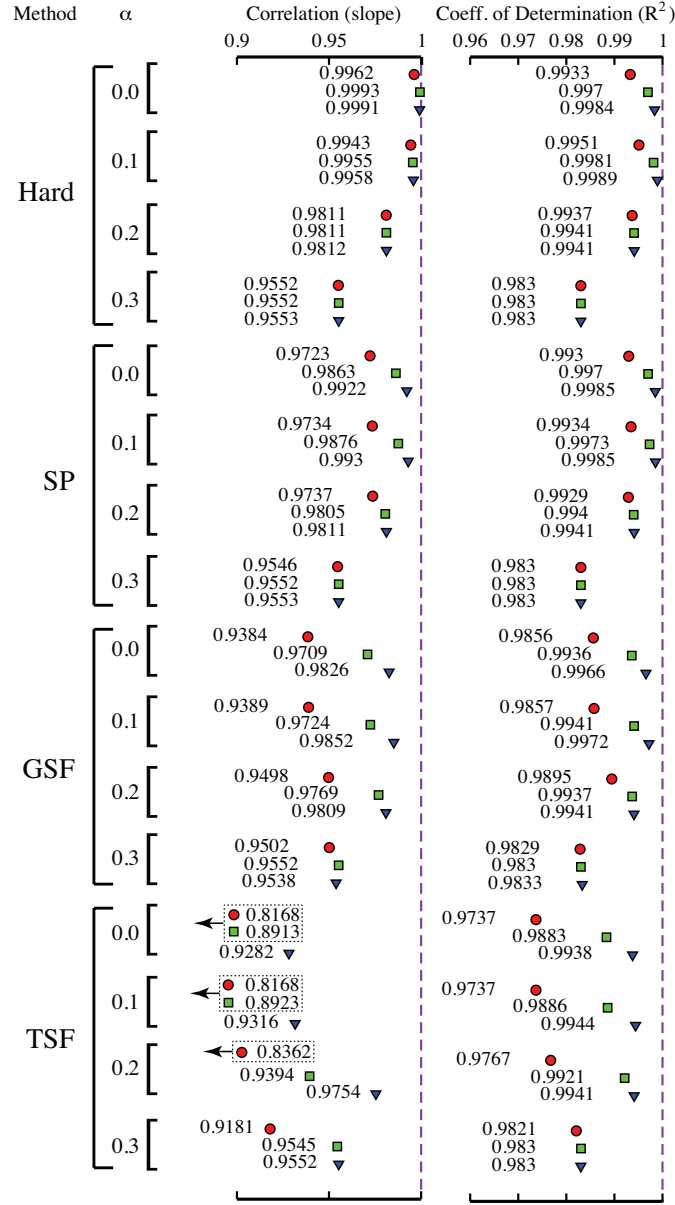
Figure 3.4. Statistical analysis of the quality of the torque vector magnitudes for the real-space electrostatic methods compared with the reference Ewald sum. Results with a value equal to 1 (dashed line) indicate force magnitude values indistinguishable from those obtained using the multipolar Ewald sum. Different values of the cutoff radius are indicated with different symbols (9 Å = circles, 12 Å = squares, and 15 Å = inverted triangles).

Ewald method, which can also be systematically improved by using moderate damping and a reasonable cutoff radius. For $\alpha = 0.2$ Å^{-1} and $r_c = 12$ Å, we observe $\mathrm{Var}(\theta) = 0.00206$, which corresponds to a distribution with 95% of force vectors within 6.37° of the corresponding Ewald forces. The TSF method produces the poorest agreement with the Ewald force directions.

Torques are again more perturbed than the forces by the new real-space methods, but even here the variance is reasonably small. For the same method (GSF) with the same parameters ($\alpha = 0.2$ Å^{-1}, $r_c = 12$ Å), the circular variance was 0.01415, corresponds to a distribution which has 95% of torque vectors are within 16.75° of the Ewald results. Again, the direction of the force and torque vectors can be systematically improved by varying α and r_c.

3.3.4 Energy conservation

We have tested the conservation of energy one can expect to see with the new real-space methods using the soft DQ liquid model with a small fraction of solvated ions. This is a test system which exercises all orders of multipole-multipole interactions derived in the chapter 2 in this series and provides the most comprehensive test of the new methods. A liquid-phase system was created with 2000 liquid-phase molecules and 48 dissolved ions at a density of 0.98 g cm^{-3} and a temperature of 300K. After equilibration in the canonical (NVT) ensemble using a Nosé-Hoover thermostat, six statistically-independent replicas of this liquid-phase system were run in the microcanonical (NVE) ensemble under the Ewald, Hard, SP, GSF, and TSF methods with a cutoff radius of 12 Å. The value of the damping coefficient was also varied from the undamped case ($\alpha = 0$) to a heavily damped case ($\alpha = 0.3$ Å^{-1}) for all of the real space methods. A sample was also run using

72
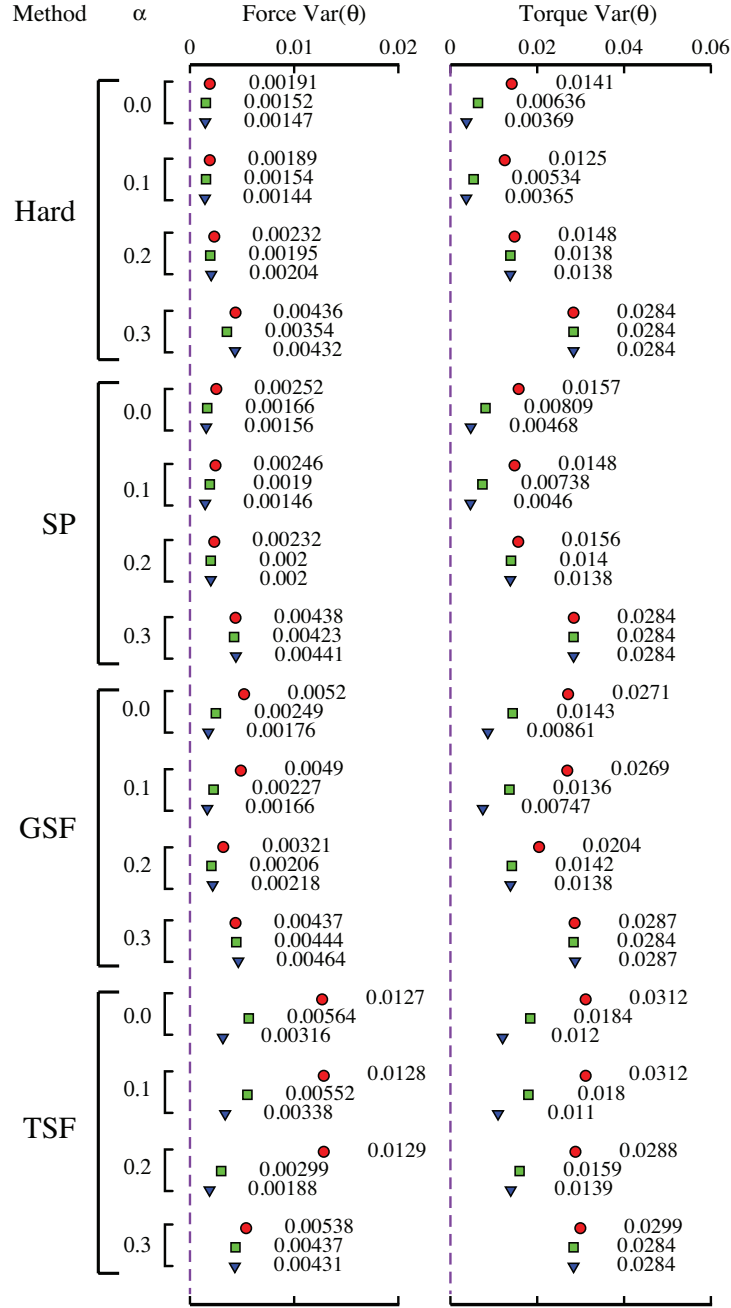
Figure 3.5. The circular variance of the direction of the force and torque vectors obtained from the real-space methods around the reference Ewald vectors. A variance equal to 0 (dashed line) indicates direction of the force or torque vectors are indistinguishable from those obtained from the Ewald sum. Here different symbols represent different values of the cutoff radius (9 Å = circle, 12 Å = square, 15 Å = inverted triangle)

the multipolar Ewald sum with the same real-space cutoff.

In figure 3.6 we show the both the linear drift in energy over time, δE_1, and the standard deviation of energy fluctuations around this drift δE_0. Both of the shifted-force methods (GSF and TSF) provide excellent energy conservation (drift less than 10^{-5} kcal / mol / ns / particle), while the hard cutoff is essentially unusable for molecular dynamics. SP provides some benefit over the hard cutoff because the energetic jumps that happen as particles leave and enter the cutoff sphere are somewhat reduced, but like the Wolf method for charges, the SP method would not be as useful for molecular dynamics as either of the shifted-force methods.

We note that for all tested values of the cutoff radius, the new real-space methods can provide better energy conservation behavior than the multipolar Ewald sum, even when relatively large k-space cutoff values are utilized.

3.3.5 Reproduction of Structural & Dynamical Features

The most important test of the modified interaction potentials is the fidelity with which they can reproduce structural features and dynamical properties in a liquid. One commonly-utilized measure of structural ordering is the pair distribution function, $g(r)$, which measures local density deviations in relation to the bulk density. In the electrostatic approaches studied here, the short-range repulsion from the Lennard-Jones potential is identical for the various electrostatic methods, and since short range repulsion determines much of the local liquid ordering, one would not expect to see many differences in $g(r)$. Indeed, the pair distributions are essentially identical for all of the electrostatic methods studied (for each of the different systems under investigation).

74
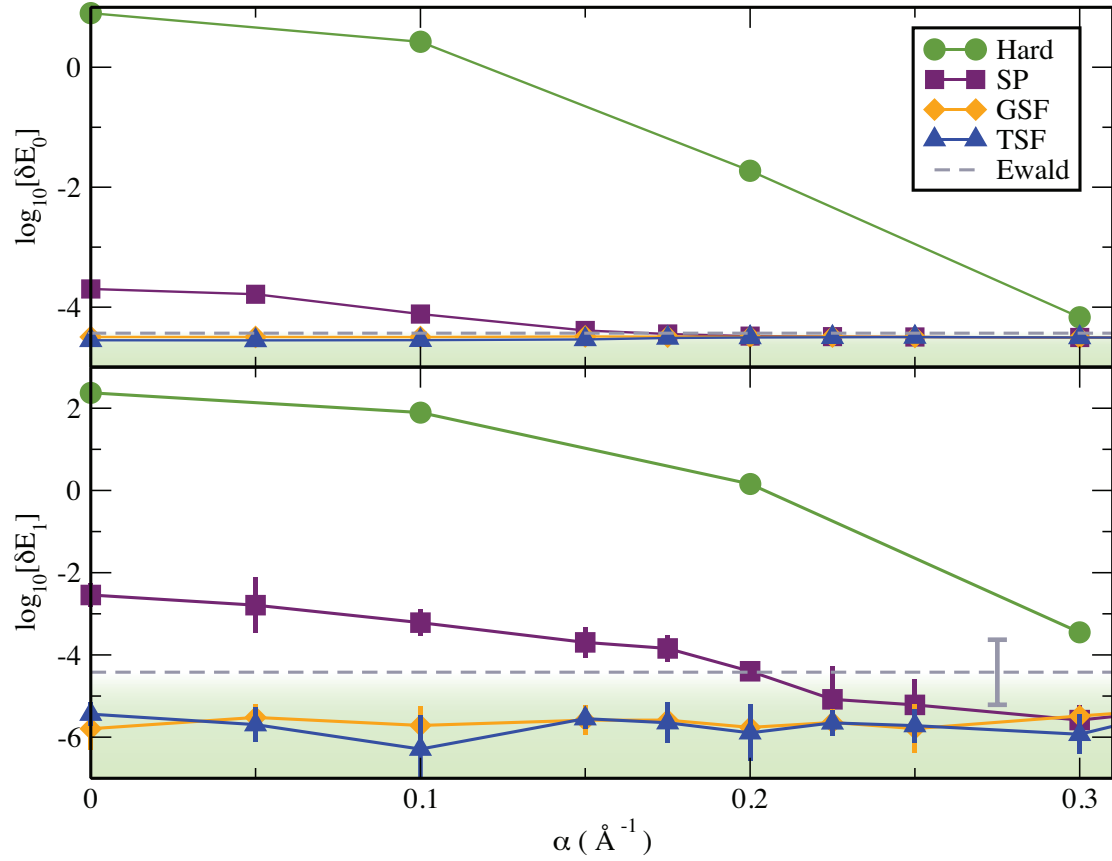
Figure 3.6. Energy conservation of the real-space methods for the soft DQ liquid / ion system. δE_1 is the linear drift in energy over time (in kcal/mol/particle/ns) and δE_0 is the standard deviation of energy fluctuations around this drift (in kcal/mol/particle). Points that appear in the green region at the bottom exhibit better energy conservation than would be obtained using common parameters for Ewald-based electrostatics.

There is a minor over-structuring of the first solvation shell when using TSF or when overdamping with any of the real-space methods. With moderate damping, GSF and SP produce pair distributions that are identical (within numerical noise) to their Ewald counterparts. The degree of over-structuring can be measured most easily using the coordination number,

$$n_C = 4\pi\rho \int_0^a r^2 \mathrm{g}(r)dr, \tag{3.5}$$

where ρ is the number density of the site-site pair interactions, and a is the radial location of the minima following the first peak in $g(r)$ ($a = 4.2$ Å for the soft DQ liquid / ion system). The coordination number is shown as a function of the damping coefficient for all of the real space methods in Fig. 3.7.

A more demanding test of modified electrostatics is the average value of the electrostatic energy $\langle U_{\mathrm{elect}}\rangle/N$ which is obtained by sampling the liquid-state configurations experienced by a liquid evolving entirely under the influence of each of the methods. In Fig. 3.7 we demonstrate how $\langle U_{\mathrm{elect}}\rangle/N$ varies with the damping parameter, α, for each of the methods.

As in the crystals studied in the chapter 2, damping is important for converging the mean electrostatic energy values, particularly for the two shifted force methods (GSF and TSF). A value of $\alpha \approx 0.2$ Å^{-1} is sufficient to converge the SP and GSF energies with a cutoff of 12 Å, while shorter cutoffs require more dramatic damping ($\alpha \approx 0.28$ Å^{-1} for $r_c = 9$ Å). Overdamping the real-space electrostatic methods occurs with $\alpha > 0.3$ Å^{-1}, causing the estimate of the electrostatic energy to drop below the Ewald results.

These "optimal" values of the damping coefficient for structural features are similar to those observed for DSF electrostatics for purely point-charge systems,

and the range $\alpha = 0.175 \to 0.225$ Å^{-1} for $r_c = 12$ Å appears to be an excellent compromise for mixed charge/multipolar systems.

To test the fidelity of the electrostatic methods at reproducing *dynamics* in a multipolar liquid, it is also useful to look at transport properties, particularly the diffusion constant,

$$D = \lim_{t \to \infty} \frac{1}{6t} \langle |\mathbf{r}(t) - \mathbf{r}(0)|^2 \rangle \tag{3.6}$$

which measures long-time behavior and is sensitive to the forces on the multipoles. The self-diffusion constants (D) were calculated from linear fits to the long-time portion of the mean square displacement, $\langle r^2(t) \rangle$.[9] In Fig. 3.7 we demonstrate how the diffusion constant depends on the choice of real-space methods and the damping coefficient. Both the SP and GSF methods can obtain excellent agreement with Ewald again using moderate damping.

In addition to translational diffusion, orientational relaxation times were calculated for comparisons with the Ewald simulations and with experiments. These values were determined by calculating the orientational time correlation function,

$$C_l^\gamma(t) = \left\langle P_l \left[\hat{\mathbf{A}}_\gamma(t) \cdot \hat{\mathbf{A}}_\gamma(0) \right] \right\rangle, \tag{3.7}$$

from the same 350 ps microcanonical trajectories that were used for translational diffusion. Here, P_l is the Legendre polynomial of order l and $\hat{\mathbf{A}}_\gamma$ is the unit vector for body axis γ. The reference frame used for our sample dipolar systems has the z-axis running along the dipoles, and for the soft DQ liquid model, the y-axis connects the two implied hydrogen-like positions. From the orientation autocorrelation functions, we can obtain time constants for rotational relaxation either by fitting to a multi-exponential model for the orientational relaxation, or by integrating the correlation functions.

In a good model for water, the orientational decay times would be comparable to water orientational relaxation times from nuclear magnetic resonance (NMR). The relaxation constant obtained from $C_2^y(t)$ is normally of experimental interest because it describes the relaxation of the principle axis connecting the hydrogen atoms. Thus, $C_2^y(t)$ can be compared to the intermolecular portion of the dipole-dipole relaxation from a proton NMR signal and can provide an estimate of the NMR relaxation time constant.[36] In Fig. 3.7 we compare the τ_2^y and τ_2^z values for the various real-space methods over a range of different damping coefficients. The rotational relaxation for the z axis primarily probes the torques on the dipoles, while the relaxation for the y axis is sensitive primarily to the quadrupolar torques.

In Fig. 3.7 it appears that values for D, τ_2^y, and τ_2^z using the Ewald sum are reproduced with excellent fidelity by the GSF and SP methods. All of the real space methods can be *overdamped*, which reduces the effective range of multipole interactions, causing structural and dynamical changes from the correct behavior. Because overdamping weakens orientational preferences between adjacent molecules, it manifests as too-rapid orientational decay coupled with faster diffusion and over-coordination of the liquid. Underdamping is less problematic for the SP and GSF methods, as their structural and dynamical properties still reproduce the Ewald results even in the completely undamped ($\alpha = 0$) case. An optimal range for the electrostatic damping parameter appears to be $\alpha = 0.175 \rightarrow 0.225$ Å^{-1} for $r_c = 12$ Å, which similar to the optimal range found for the damped shifted force potential for point charges.[23]
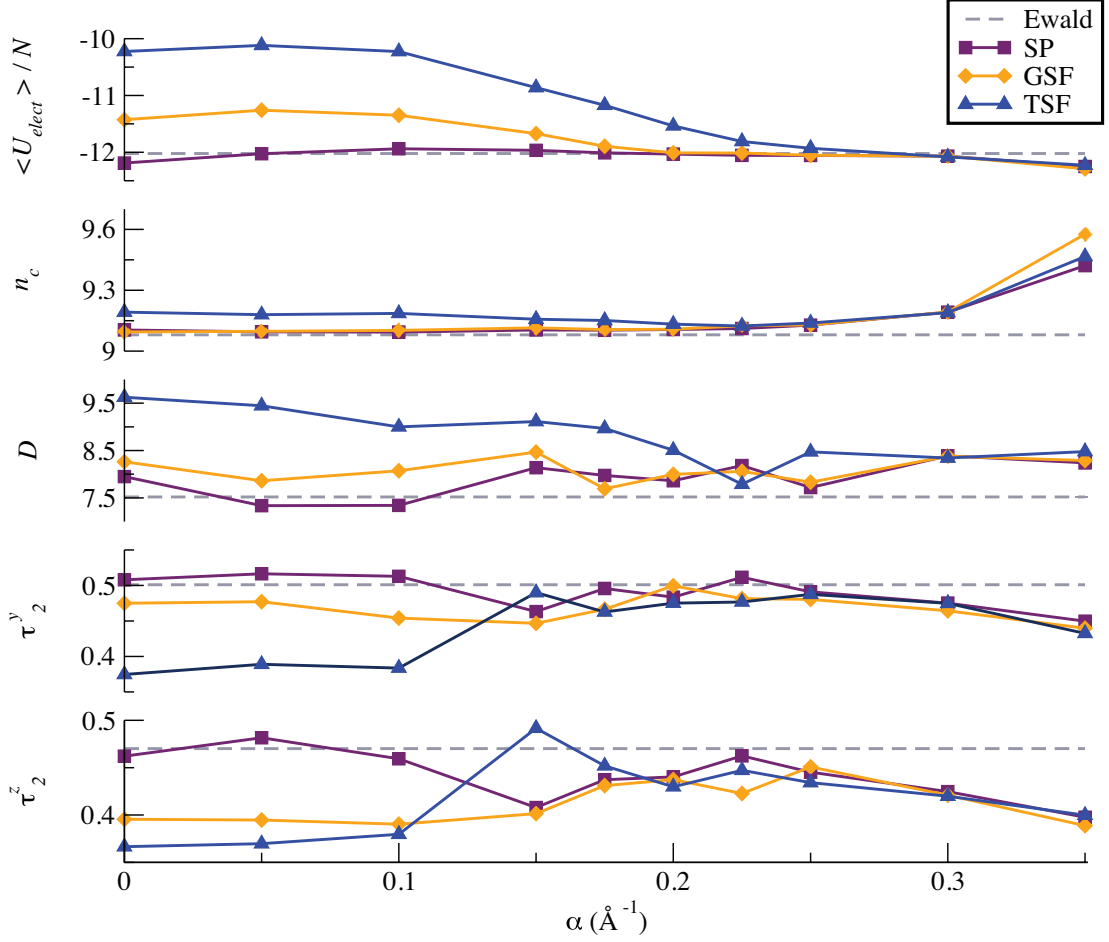
Figure 3.7. Comparison of the structural and dynamic properties for the combined multipolar liquid (soft DQ liquid + ions) for all of the real-space methods with $r_c = 12$ Å. Electrostatic energies, $\langle U_{elect} \rangle / N$ (in kcal / mol), coordination numbers, n_C, diffusion constants (in $10^{-5} cm^2 s^{-1}$), and rotational correlation times (in ps) all show excellent agreement with Ewald results for damping coefficients in the range $\alpha = 0.175 \rightarrow 0.225$ Å^{-1}.

3.4 Summary

In the chapter 2, we generalized the charge-neutralized electrostatic energy originally developed by Wolf *et al.*[95] to multipole-multipole interactions up to quadrupolar order. The SP method is essentially a multipole-capable version of the Wolf model. The SP method for multipoles provides excellent agreement with Ewald-derived energies, forces and torques, and is suitable for Monte Carlo simulations, although the forces and torques retain discontinuities at the cutoff distance that prevents its use in molecular dynamics.

We also developed two natural extensions of the damped shifted-force (DSF) model originally proposed by Zahn *et al.* and extended by Fennell and Gezelter.[18, 23] The GSF and TSF approaches provide smooth truncation of energies, forces, and torques at the real-space cutoff, and both converge to DSF electrostatics for point-charge interactions. The TSF model is based on a high-order truncated Taylor expansion which can be relatively perturbative inside the cutoff sphere. The GSF model takes the gradient from an images of the interacting multipole that has been projected onto the cutoff sphere to derive shifted force and torque expressions, and is a significantly more gentle approach.

The GSF method produces quantitative agreement with Ewald energies, forces, and torques. It also performs well in conserving energy in MD simulations. The Taylor-shifted (TSF) model provides smooth dynamics, but these take place on a potential energy surface that is significantly perturbed from Ewald-based electrostatics. Because it performs relatively poorly compared with GSF, it may seem odd that that the TSF model was included in this work. However, the functional forms derived for the SP and GSF methods depend on the separation of orientational contributions that were made visible by the Taylor series of the electrostatic

kernel at the cutoff radius. The TSF method also has the unique property that a large number of derivatives can be made to vanish at the cutoff radius. This property has proven useful in past treatments of the corrections to the Clausius-Mossotti fluctuation formula for dielectric constants.[37]

Reproduction of both structural and dynamical features in the liquid systems is remarkably good for both the SP and GSF models. Pair distribution functions are essentially equivalent to the same functions produced using Ewald-based electrostatics, and with moderate damping, a structural feature that directly probes the electrostatic interaction (e.g. the mean electrostatic potential energy) can also be made quantitative. Dynamical features are sensitive probes of the forces and torques produced by these methods, and even though the smooth behavior of forces is produced by perturbing the overall potential, the diffusion constants and orientational correlation times are quite close to the Ewald-based results.

The only cases we have found where the new GSF and SP real-space methods can be problematic are those which retain a bulk dipole moment at large distances (e.g. the Z_1 dipolar lattice). In ferroelectric materials, uniform weighting of the orientational contributions can be important for converging the total energy. In these cases, the damping function which causes the non-uniform weighting can be replaced by the bare electrostatic kernel, and the energies return to the expected converged values.

Based on the results of this work, we can conclude that the GSF method is a suitable and efficient replacement for the Ewald sum for evaluating electrostatic interactions in modern MD simulations, and the SP method would be an excellent choice for Monte Carlo simulations where smooth forces and energy conservation are not important. Both the SP and GSF methods retain excellent fidelity to the

Ewald energies, forces and torques. Additionally, the energy drift and fluctuations from the GSF electrostatics are significantly better than a multipolar Ewald sum for finite-sized reciprocal spaces, and physical properties are reproduced accurately.

As in all purely pairwise cutoff methods, the SP, GSF and TSF methods are expected to scale approximately *linearly* with system size, and are easily parallelizable. This should result in substantial reductions in the computational cost of performing large simulations. With the proper use of pre-computation and spline interpolation of the radial functions, the real-space methods are essentially the same cost as a simple real-space cutoff. They require no Fourier transforms or k-space sums, and guarantee the smooth handling of energies, forces, and torques as multipoles cross the real-space cutoff boundary.

We are not suggesting that there is any flaw with the Ewald sum; in fact, it is the standard by which the SP, GSF, and TSF methods have been judged in this work. However, these results provide evidence that in the typical simulations performed today, the Ewald summation may no longer be required to obtain the level of accuracy most researchers have come to expect.

CHAPTER 4

DIELECTRIC PROPERTIES

In the previous chapter, we have derived various physical properties considering SP, GSF, and TSF methods and tested result against the multipolar Ewald method. In this chapter, we discuss fluctuation, perturbation, and potential of mean force (PMF) methods for calculating the dielectric properties of the dipolar and quadrupolar fluids using newly developed real space methods. Since the dielectric constant is a macroscopic property, the interactions of a molecule with the rest of the molecules of the system are important. Our newly developed real space methods utilize a cutoff radius which reduces the number of interactions calculated in the system. Hence, the formula for the dielectric constant should be modified accordingly. Therefore to get correct dielectric properties using the result obtained from the simulation, we need to evaluate correction factor for each real-space methods separately. In this chapter, we have also calculated the correction factors for each real-space methods and tabulated for both dipolar and quadrupolar fluids.

4.1 Introduction

One of the most difficult tests of any new electrostatic method is the fidelity with which that method can reproduce the bulk-phase polarizability or equiva-

lently, the dielectric properties of a fluid. Before the advent of computer simulations, Kirkwood and Onsager developed fluctuation formulae for the dielectric properties of dipolar fluids.[43, 64] Of particular interest is the static dielectric constant, ϵ. Using the Ewald sum under tin-foil boundary conditions, ϵ can be calculated for systems of non-polarizable substances via

$$\epsilon = 1 + \frac{\langle M^2 \rangle}{3\epsilon_0 k_{\mathrm{B}} T V}, \tag{4.1}$$

where ϵ_0 is the permittivity of free space and $\langle M^2 \rangle$ is the fluctuation of the system dipole moment.[9] The numerator in the fractional term in equation (4.1) is identical to the quantity calculated in the finite-system Kirkwood g factor (G_k):

$$G_k = \frac{\langle M^2 \rangle}{N\mu^2}, \tag{4.2}$$

where μ is the dipole moment of a single molecule of the homogeneous system.[60–63] The fluctuation term in both equation (4.1) and (4.2) is calculated as follows,

$$\begin{aligned}
\langle M^2 \rangle &= \langle M \cdot M \rangle - \langle M \rangle \cdot \langle M \rangle \\
&= \langle M_x^2 + M_y^2 + M_z^2 \rangle - (\langle M_x \rangle^2 + \langle M_x \rangle^2 + \langle M_x \rangle^2).
\end{aligned} \tag{4.3}$$

This fluctuation term can be accumulated during a simulation; however, it converges rather slowly, thus requiring multi-nanosecond simulation times.[32] In the case of tin-foil boundary conditions, the dielectric/surface term of the Ewald summation is equal to zero.

Similar formulae were developed by Logan *et al.* for the bulk polarizability of quadrupolar fluids.[45–47] In modern simulations, bulk materials are usually

treated using periodic replicas of small regions, and this level of approximation requires corrections to the fluctuation formulae that were derived for the bulk fluids. In 1983 Neumann proposed a general formula for evaluating dielectric properties of dipolar fluids using real-space cutoff methods.[60] Steinhauser and Neumann used this formula to evaluate the corrected dielectric constant for the Stockmayer fluid using two different methods: Ewald-Kornfield (EK) and reaction field (RF) methods.[62]

Zahn *et al.*[18] utilized this approach and evaluated the correction factor for using damped shifted charge-charge kernel. This was later generalized by Izvekov *et al.*,[37] who that the expression for the dielectric constant reduces to widely-used *conducting boundary* formula for real-space cutoff methods that have first derivatives that vanish at the cutoff sphere.

In quadrupolar fluids, the relationship between quadrupolar susceptibility and the dielectric constant is not as straightforward as in the dipolar case. The dielectric constant depends on the geometry of the external field perturbation.[21] Significant efforts have been made to increase our understanding the dielectric properties of these fluids,[13, 39, 40] although a correction formula for different real-space methods has not yet been developed.

In this paper we derive general formulae for calculating the dielectric properties of quadrupolar fluids. We also evaluate the correction factor for SP, GSF, and TSF methods for both dipolar and quadrupolar fluids interacting via point charges, point dipoles or through quadrupole-quadrupole interactions.

We have also calculated the screening behavior for two ions immersed in a quadrupolar fluid to estimate the dielectric screening from the quadrupolar susceptibility. We have used three different methods to compare our results with

computer simulations:

1. responses of the fluid to external perturbations,

2. fluctuations of box multipole moments, and

3. potentials of mean force between solvated ions,

In the external field perturbation, the net polarization of the system is observed as a linear response of the applied field perturbation, where proportionality constant is determined by the electrostatic interaction between the electrostatic multipoles at a given temperature. The fluctuation formula observes the time average fluctuation of the multipolar moment as a function of temperature. The average fluctuation value of the system is determined by the multipole-multipole interactions between molecules at a given temperature. Since the expression of the electrostatic interaction energy, force, and torque in the real space electrostatic methods are different from their original definition, both fluctuation and external field perturbation formula should also be modified accordingly. The potential of mean force method calculates dielectric constant or screening factor from the potential energy between ions before and after dielectric material is introduced. All of these different methods for calculating dielectric properties will be discussed in detail in the following sections: 4.3.1,4.3.2, and 4.4.

4.2   Boltzmann average for orientational polarization

The dielectric properties of the system is mainly arise from two different ways: i) the applied field distort the charge distributions so it produces an induced multipolar moment in each molecule; and ii) the applied field tends to line up originally randomly oriented molecular moment towards the direction of the applied field.

In this study, we basically focus on the orientational contribution in the dielectric properties. If we consider a system of molecules in the presence of external field perturbation, the perturbation experienced by any molecule will not be only due to external field or field gradient but also due to the field or field gradient produced by the all other molecules in the system. In the following subsections 4.2.1 and 4.2.2, we will discuss about the molecular polarization only due to external field perturbation. The contribution of the field or field gradient due to all other molecules will be taken into account while calculating correction factor in the section 4.5.

4.2.1 Dipole

Consider a system of molecules, each with permanent dipole moment p_o. In the absense of external field, thermal agitation orients the dipoles randomly, reducing the system moment to zero. External fields will tend to line up the dipoles in the direction of applied field. Here we have considered net field from all other molecules is considered to be zero. Therefore the total Hamiltonian of each molecule is,[38]

$$H = H_o - \mathbf{p_o}.\mathbf{E}, \tag{4.4}$$

where H_o is a function of the internal coordinates of the molecule. The Boltzmann average of the dipole moment is given by,

$$\langle p_{mol} \rangle = \frac{\int d\Omega \ p_o \ cos\theta \ e^{\frac{p_o E \ cos\theta}{k_B T}}}{\int d\Omega \ e^{\frac{p_o E \ cos\theta}{k_B T}}}, \tag{4.5}$$

where $\mathbf{E}$ is selected along z-axis. If we consider that the applied field is small, *i.e.* $\frac{p_o E \cos\theta}{k_B T} \ll 1$,

$$\langle p_{mol} \rangle \approx \frac{1}{3} \frac{p_o{}^2}{k_B T} E, \tag{4.6}$$

where $\alpha_p = \frac{1}{3} \frac{p_o{}^2}{k_B T}$ is a molecular polarizability. The orientational polarization depends inversely on the temperature and applied field must overcome the thermal agitation.

4.2.2 Quadrupole

Consider a system of molecules with permanent quadrupole moment $q_{\alpha\beta}$. The average quadrupole moment at temperature T in the presence of uniform applied field gradient is given by,[4, 5]

$$\langle q_{\alpha\beta} \rangle = \frac{\int d\Omega \; e^{-\frac{H}{k_B T}} q_{\alpha\beta}}{\int d\Omega \; e^{-\frac{H}{k_B T}}} = \frac{\int d\Omega \; e^{\frac{q_{\mu\nu} \, \partial_\nu E_\mu}{k_B T}} q_{\alpha\beta}}{\int d\Omega \; e^{\frac{q_{\mu\nu} \, \partial_\nu E_\mu}{k_B T}}}, \tag{4.7}$$

where $\int d\Omega = \int_0^{2\pi} \int_0^{\pi} \int_0^{2\pi} \sin\theta \; d\theta \; d\phi \; d\psi$ is the integration over Euler angles, $H = H_o - q_{\mu\nu} \, \partial_\nu E_\mu$ is the energy of a quadrupole in the gradient of the applied field and H_o is a function of internal coordinates of the molecule. The energy and quadrupole moment can be transformed into body frame using following relation,

$$q_{\alpha\beta} = \eta_{\alpha\alpha'} \, \eta_{\beta\beta'} \, q^*_{\alpha'\beta'}$$

$$H = H_o - q : \vec{\nabla}\vec{E} = H_o - q_{\mu\nu} \, \partial_\nu E_\mu = H_o - \eta_{\mu\mu'} \, \eta_{\nu\nu'} \, q^*_{\mu'\nu'} \, \partial_\nu E_\mu. \tag{4.8}$$

Here the starred tensors are the components in the body fixed frame. Substituting equation (4.8) in the equation (4.7) and taking linear terms in the expansion we

get,

$$\langle q_{\alpha\beta} \rangle = \frac{\int d\Omega \left(1 + \frac{\eta_{\mu\mu'} \, \eta_{\nu\nu'} \, q^*_{\mu'\nu'} \, \partial_\nu E_\mu}{k_B T} \right) q_{\alpha\beta}}{\int d\Omega \left(1 + \frac{\eta_{\mu\mu'} \, \eta_{\nu\nu'} \, q^*_{\mu'\nu'} \, \partial_\nu E_\mu}{k_B T} \right)}, \tag{4.9}$$

where $\eta_{\alpha\alpha'}$ is the inverse of the rotation matrix that transforms the body fixed co-ordinates to the space co-ordinates,

$$\eta_{\alpha\alpha'} = \begin{pmatrix} cos\phi \; cos\psi - cos\theta \; sin\phi \; sin\psi & -cos\theta \; cos\psi \; sin\phi - cos\phi \; sin\psi & sin\theta \; sin\phi \\ cos\psi \; sin\phi + cos\theta \; cos\phi \; sin\psi & cos\theta \; cos\phi \; cos\psi - sin\phi \; sin\psi & -cos\phi \; sin\theta \\ sin\theta \; sin\psi & -cos\psi \; sin\theta & cos\theta \end{pmatrix}.$$

Integration of 1st and 2nd terms in the denominator gives $8\pi^2$ and $8\pi^2/3 \; \vec{\nabla}.\vec{E} \; Tr(q^*)$ respectively. The second term vanishes for charge free space (i.e. $\vec{\nabla}.\vec{E} = 0$). Similarly integration of the 1st term in the numerator produces $8\pi^2/3 \; Tr(q^*)\delta_{\alpha\beta}$ and the 2nd term produces $8\pi^2/15k_B T(3q^*_{\alpha'\beta'}q^*_{\beta'\alpha'} - q^*_{\alpha'\alpha'}q^*_{\beta'\beta'})\partial_\alpha E_\beta$, if $\vec{\nabla}.\vec{E} = 0$, $\partial_\alpha E_\beta = \partial_\beta E_\alpha$ and $q^*_{\alpha'\beta'} = q^*_{\beta'\alpha'}$. Therefore the Boltzmann average of a quadrupole moment can be written as,

$$\langle q_{\alpha\beta} \rangle = \frac{1}{3}Tr(q^*) \, \delta_{\alpha\beta} + \frac{\bar{q_o}^2}{15k_B T} \, \partial_\alpha E_\beta, \tag{4.10}$$

where $\alpha_q = \frac{\bar{q_o}^2}{15k_B T}$ is a molecular quadrupolarizablity and $\bar{q_o}^2 = 3q^*_{\alpha'\beta'}q^*_{\beta'\alpha'} - q^*_{\alpha'\alpha'}q^*_{\beta'\beta'}$ is a square of the net quadrupole moment of a molecule.

4.3 Macroscopic Polarizability

If we consider a system of dipolar or quadrupolar fluid in the external field perturbation, the net polarization of the system will still be proportional to the applied field perturbation.[13, 80, 81, 84] In simulation the net polarization of the system is determined by the interaction of molecule with all other molecules as well

as external field perturbation. Therefore the macroscopic polarizablity obtained from the simulation always varies with nature of real-space electrostatic interaction methods implemented in the simulation. To determine a susceptibility or dielectric constant of the material (which is a actual physical property of the dipolar or quadrupolar fluid) from the macroscopic polarizablity, we need to incorporate the interaction between molecules which has been discussed in detail in section 4.5. In this section we discuss about the two different methods of calculating macroscopic polarizablity for both dipolar and quadrupolar fluid.

4.3.1   External field perturbation

In the presence of uniform electric field $\mathbf{E}^o$, a system of dipolar molecules polarizes along the direction of the applied field (or field gradient). Therefore the net dipolar polarization $\mathbf{P}$ of the system is,

$$\mathbf{P} = \epsilon_o \alpha_D \, \mathbf{E}^o. \tag{4.11}$$

The constant α_D is a macroscopic polarizability, which is a property of the dipolar fluid in a given density and temperature.

Similarly, in the presence of external field gradient the system of quadrupolar molecule polarizes along the direction of applied field gradient therefore the net quadrupolar polarization of the system can be given by,

$$Q_{\alpha\beta} = \frac{1}{3} \, Tr(Q) \, \delta_{\alpha\beta} + \epsilon_o \, \alpha_Q \, \partial_\alpha E_\beta^o$$

$$or \tag{4.12}$$

$$\frac{1}{3} \, \Theta_{\alpha\beta} = \epsilon_o \, \alpha_Q \, \partial_\alpha E_\beta^o$$

where $Q_{\alpha\beta}$ is a tensor component of the traced quadrupolar moment of the system, α_Q is a macroscopic quadrupolarizability has a dimension of $length^{-2}$, and $\Theta_{\alpha\beta} = 3Q_{\alpha\beta} - Tr(Q)$ is the traceless component of the quadrupole moment.

4.3.2 Fluctuation formula

For a system of molecules with net dipolar moment $\mathbf{M}$ at thermal equilibrium of temperature T in the presence of applied field $\mathbf{E^o}$, the average dipolar polarization can be expressed in terms of fluctuation of the net dipole moment as below,[85]

$$\langle\mathbf{P}\rangle = \epsilon_o \frac{\langle\mathbf{M^2}\rangle - \langle\mathbf{M}\rangle^2}{3\epsilon_o V k_B T}\mathbf{E^o} \tag{4.13}$$

This is similar to the formula for boltzmann average of single dipolar molecule in the subsection 4.2.1. Here $\langle\mathbf{P}\rangle$ is average polarization and $\langle\mathbf{M^2}\rangle - \langle\mathbf{M}\rangle^2$ is the net dipole fluctuation at temperature T. For the limiting case $\mathbf{E}^o \to 0$, ensemble average of both net dipole moment $\langle\mathbf{M}\rangle$ and dipolar polarization $\langle\mathbf{P}\rangle$ tends to vanish but $\langle\mathbf{M^2}\rangle$ will still be non-zero. The dipolar macroscopic polarizability can be written as,

$$\alpha_D = \frac{\langle\mathbf{M^2}\rangle - \langle\mathbf{M}\rangle^2}{3\epsilon_o V k_B T} \tag{4.14}$$

This is a macroscopic property of dipolar material which is true even if applied field $\mathbf{E}^o \to 0$.

Analogous formula can also be written for a system with quadrupolar molecules,

$$\langle Q_{\alpha\beta}\rangle = \frac{1}{3}Tr(\mathbf{Q})\,\delta_{\alpha\beta} + \epsilon_o \frac{\langle\mathbf{Q^2}\rangle - \langle\mathbf{Q}\rangle^2}{15\epsilon_o V k_B T}\partial_\alpha E_\beta^o \tag{4.15}$$

where $Q_{\alpha\beta}$ is a component of system quadrupole moment, $\mathbf{Q}$ is net quadrupolar moment which can be expressed as $\mathbf{Q}^2 = 3Q_{\alpha\beta}Q_{\alpha\beta} - (Tr\mathbf{Q})^2$. The macroscopic

91

quadrupolarizability is given by,

$$\alpha_Q = \frac{\langle \mathbf{Q}^2 \rangle - \langle \mathbf{Q} \rangle^2}{15\epsilon_o V k_B T} \tag{4.16}$$

4.4 Potential of mean force

In this method, we will measure the interaction between a positive and negative charge at varying distances after introducing a dipolar (or quadrupolar) material between them. The potential of mean force (PMF) between two ions in a liquid is obtained by constraining their distance and measuring the mean constraint force required to hold them at a fixed distance r. The PMF is obtained from a sequence of simulations can be expressed as [91],

$$w(r) = \int_{r_o}^{r} \langle \frac{\partial f}{\partial r'} \rangle \, dr' + 2kT \log(r/r_o) + w(r_o), \tag{4.17}$$

where $\langle \partial f/\partial r' \rangle$ is the mean constraint force, $2kT \log(r/r_o)$ is the Fixman factor, and r_o is the reference position. The potential energy between two charges at separation r is given by,

$$w(r) = \frac{1}{4\pi\epsilon} \frac{q_1 q_2}{r}, \tag{4.18}$$

where ϵ is the dielectric constant for the fluid.

The quadrupole molecule can couple with the gradient of the electric field and the two opposite point charges produces non-zero value of both electric field as well as gradient of the field. Therefore, this simulation set up can be used to determine the dielectric constant for both dipolar and quadrupolar fluid.

4.5 Correction factor

Since equations (4.11, 4.12, 4.13, and 4.15) provide relation between polarization (dipolar or quadrupolar) and applied field (uniform field or field gradient), χ_d (or χ_q) is actually a macroscopic polarizability (or quadrupolarizability), which is different than the dipolar (or quadrupolar) susceptibility of the fluid. Actual constitutive relation should have a relation between polarization and Maxwell field (or field gradient) at different point in the sample. We can obtain susceptibility of the fluid from its macroscopic polarizability using correction factor evaluated below.

4.5.1 Dipolar system

In the presence of an external field $\mathbf{E}$ polarization $\mathbf{E}$ will be induced in a dipolar system. The total electrostatic field (or Maxwell electric field) at point $\mathbf{r}$ in a system is,[60]

$$\mathbf{E}(\mathbf{r}) = \mathbf{E}^o(\mathbf{r}) + \frac{1}{4\pi\epsilon_o} \int d^3r' \mathbf{T}(\mathbf{r} - \mathbf{r}') \cdot \mathbf{P}(\mathbf{r}'). \qquad (4.19)$$

We can consider the cases of Stockmayer (dipolar) soft spheres that are represented either by two closely-spaced point charges or by a single point dipole (see Fig. 4.1). In the case where point charges are interacting via an electrostatic kernel, $v(r)$, the effective *molecular* dipole tensor, $\mathbf{T}$ is obtained from two successive applications of the gradient operator to the electrostatic kernel,

$$\mathbf{T}_{\alpha\beta}(r) = \nabla_\alpha \nabla_\beta \left(v(r) \right) = \delta_{\alpha\beta} \left(\frac{1}{r} v'(r) \right) + \frac{r_\alpha r_\beta}{r^2} \left(v''(r) - \frac{1}{r} v'(r) \right) \qquad (4.20)$$

where $v(r)$ may be either the bare kernel $(1/r)$ or one of the modified (Wolf or
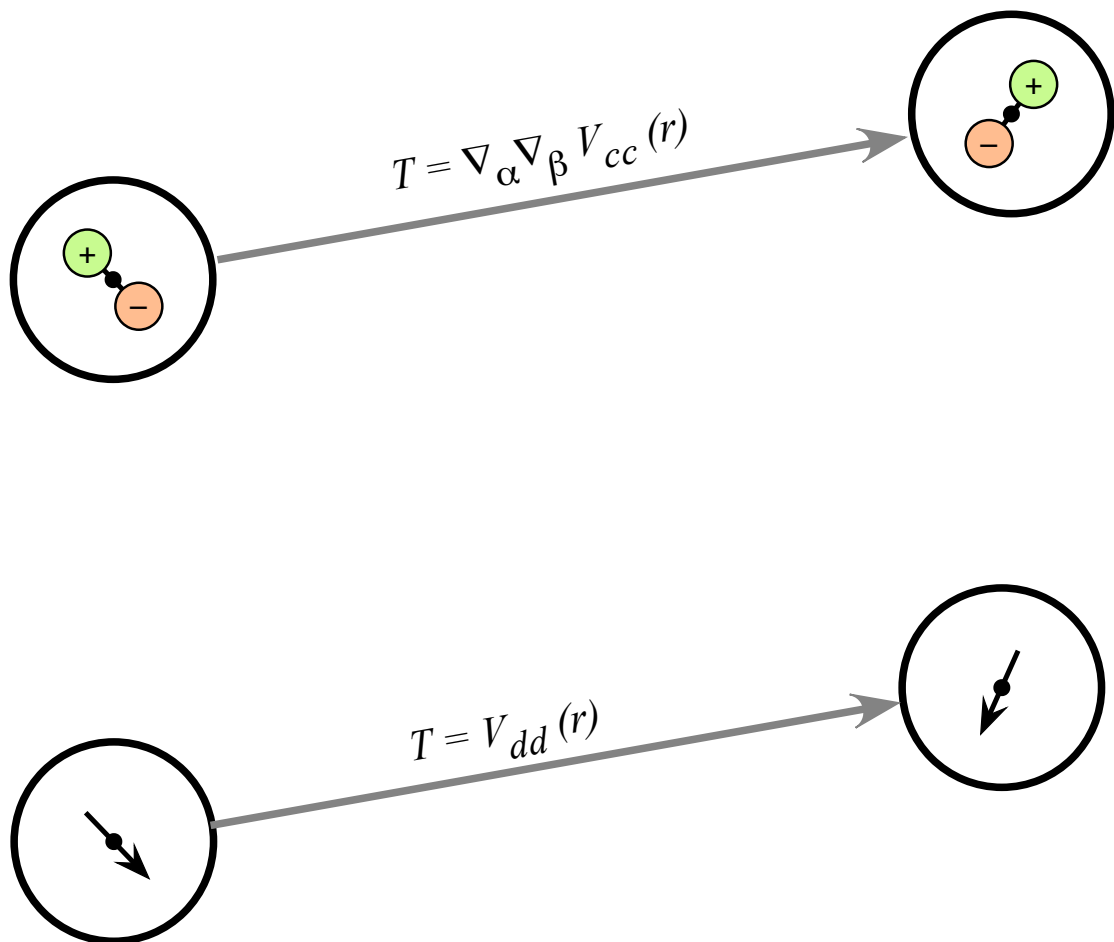
Figure 4.1. With the real-space electrostatic methods, the effective dipole tensor, **T**, governing interactions between molecular dipoles is not the same for charge-charge interactions as for point dipoles.

DSF) kernels. This tensor describes the effective interaction between molecular dipoles ($\mathbf{D}$) in Gaussian units as $-\mathbf{D} \cdot \mathbf{T} \cdot \mathbf{D}$. When utilizing the new real-space methods for point dipoles, the tensor is explicitly constructed,

$$\mathbf{T}_{\alpha\beta}(r) = \delta_{\alpha\beta} v_{21}(r) + \frac{r_\alpha r_\beta}{r^2} v_{22}(r) \tag{4.21}$$

where the functions $v_{21}(r)$ and $v_{22}(r)$ depend on the level of the approximation. Although the Taylor-shifted (TSF) and gradient-shifted (GSF) models produce to the same $v(r)$ function for point charges, they have distinct forms for the dipole-dipole interactions.

Using constitutive relation, the polarization density $\mathbf{P}(\mathbf{r})$ is given by,

$$\mathbf{P}(\mathbf{r}) = \epsilon_o \, \chi_D^* \left(\mathbf{E}^o(\mathbf{r}) + \frac{1}{4\pi\epsilon_o} \int d^3 r' \mathbf{T}(\mathbf{r} - \mathbf{r}') \cdot \mathbf{P}(\mathbf{r}') \right). \tag{4.22}$$

Here χ_D^* is a dipolar susceptibility can be expressed in terms of dielectric constant as $\chi_D^* = \epsilon - 1$ which different than macroscopic dipolar polarizability α_D in the sections 4.3.1 and 4.3.2. We can split integral into two parts: singular part i.e $|\mathbf{r} - \mathbf{r}'| \to 0$ and non-singular part i.e $|\mathbf{r} - \mathbf{r}'| > 0$. The singular part of the integral can be written as,[38, 60]

$$\frac{1}{4\pi\epsilon_o} \int_{|\mathbf{r}-\mathbf{r}'| \to 0} d^3 r' \, \mathbf{T}(\mathbf{r} - \mathbf{r}') \cdot \mathbf{P}(\mathbf{r}') = -\frac{\mathbf{P}(\mathbf{r})}{3\epsilon_o} \tag{4.23}$$

Substituting equation (4.23) in the equation (4.22) we get,

$$\mathbf{P}(\mathbf{r}) = 3\epsilon_o \frac{\chi_D^*}{\chi_D^* + 3} \left(\mathbf{E}^o(\mathbf{r}) + \frac{1}{4\pi\epsilon_o} \int_{|\mathbf{r}-\mathbf{r}'|>0} d^3 r' \, \mathbf{T}(\mathbf{r} - \mathbf{r}') \cdot \mathbf{P}(\mathbf{r}') \right). \tag{4.24}$$

For both polarization and electric field homogeneous, this can be easily solved

using Fourier transformation,

$$\mathbf{P}(\kappa) = 3\epsilon_o \frac{\chi_D^*}{\chi_D^* + 3} \left(1 - \frac{3}{4\pi} \frac{\chi_D^*}{\chi_D^* + 3} \mathbf{T}(\kappa)\right)^{-1} \mathbf{E}^o(\kappa). \qquad (4.25)$$

For homogeneous applied field Fourier component is non-zero only if $\kappa = 0$. Therefore,

$$\mathbf{P}(0) = 3\epsilon_o \frac{\chi_D^*}{\chi_D^* + 3} \left(1 - \frac{\chi_D^*}{\chi_D^* + 3} A_{dipole}\right)^{-1} \mathbf{E}^o(0). \qquad (4.26)$$

where $A_{dipole} = \frac{3}{4\pi} T(0) = \frac{3}{4\pi} \int_V d^3r \, T(r)$. Now equation (4.26) can be compared with equation (4.13). Therefore,

$$\frac{\langle \mathbf{M^2} \rangle - \langle \mathbf{M} \rangle^2}{3\epsilon_o V k_B T} = \frac{3 \, \chi_D^*}{\chi_D^* + 3} \left(1 - \frac{\chi_D^*}{\chi_D^* + 3} A_{dipole}\right)^{-1} \qquad (4.27)$$

Substituting $\chi_D^* = \epsilon - 1$ and $\frac{\langle \mathbf{M^2} \rangle - \langle \mathbf{M} \rangle^2}{3\epsilon_o V k_B T} = \epsilon_{CB} - 1 = \alpha_D$ in above equation we get,

$$\epsilon = \frac{3 + (A_{dipole} + 2)(\epsilon_{CB} - 1)}{3 + (A_{dipole} - 1)(\epsilon_{CB} - 1)} = \frac{3 + (A_{dipole} + 2)\alpha_D}{3 + (A_{dipole} - 1)\alpha_D} \qquad (4.28)$$

where ϵ_{CB} is dielectric constant obtained from conducting boundary condition. Equation (4.28) calculates actual dielectric constant from the dielectric constant obtained from the conducting boundary condition (which can be obtained directly from the simulation) using correction factor. The correction factor is different for different real-space cutoff methods. The expression for correction factor assuming a single point dipole or two closely spaced point charges for SP, GSF, and TSF method is listed in Table 4.1.

TABLE 4.1

Expressions for the dipolar correction factor (A) for the real-space electrostatic methods in terms of the damping parameter (α) and the cutoff radius (r_c). The Ewald-Kornfeld result derived in Refs. [2, 3, 60] is shown for comparison using the Ewald convergence parameter (κ) and the real-space cutoff value (r_c).

Method	A_{charges}	A_{dipoles}
Spherical Cutoff (SC)	$\text{erf}(r_c\alpha) - \frac{2\alpha r_c}{\sqrt{\pi}}e^{-\alpha^2 r_c^2}$	$\text{erf}(r_c\alpha) - \frac{2\alpha r_c}{\sqrt{\pi}}e^{-\alpha^2 r_c^2}$
Shifted Potental (SP)	$\text{erf}(r_c\alpha) - \frac{2\alpha r_c}{\sqrt{\pi}}e^{-\alpha^2 r_c^2}$	$\text{erf}(r_c\alpha) - \frac{2\alpha r_c}{\sqrt{\pi}}\left(1 + \frac{2\alpha^2 r_c^2}{3}\right)e^{-\alpha^2 r_c^2}$
Gradient-shifted (GSF)	1	$\text{erf}(\alpha r_c) - \frac{2\alpha r_c}{\sqrt{\pi}}\left(1 + \frac{2\alpha^2 r_c^2}{3} + \frac{\alpha^4 r_c^4}{3}\right)e^{-\alpha^2 r_c^2}$
Taylor-shifted (TSF)	1	1
Ewald-Kornfeld (EK)	$\text{erf}(r_c\kappa) - \frac{2\kappa r_c}{\sqrt{\pi}}e^{-\kappa^2 r_c^2}$	$\text{erf}(r_c\kappa) - \frac{2\kappa r_c}{\sqrt{\pi}}e^{-\kappa^2 r_c^2}$

4.5.2 Quadrupolar system

In the presence of the field gradient $\partial_\alpha E_\beta$, a non-vanishing quadrupolar polarization (quadrupole moment per unit volume) $\bar{Q}_{\alpha\beta}$ will be induced in the entire volume of a sample. The total field at any point $\vec{r}$ in the sample is given by,

$$\partial_\alpha E_\beta(\mathbf{r}) = \partial_\alpha E^o{}_\beta(\mathbf{r}) + \frac{1}{4\pi\epsilon_o} \int T_{\alpha\beta\gamma\delta}(|\mathbf{r} - \mathbf{r}'|)\, Q_{\gamma\delta}(\mathbf{r}')\, d^3r' \qquad (4.29)$$

where $\partial_\alpha E^o{}_\beta$ is the applied field gradient and $T_{\alpha\beta\gamma\delta}$ is the quadrupole-quadrupole interaction tensor. We can represent quadrupole as a group of four closely spaced charges, two closely spaced point dipoles or single point quadrupole (see Fig. 4.2). The quadrupole-quadrupole interaction tensor from the charge representation can obtained from the application of the four successive gradient operator to the electrostatic kernel $v(r)$.

$$
\begin{aligned}
T_{\alpha\beta\gamma\delta}(r) &= \nabla_\alpha \nabla_\beta \nabla_\gamma \nabla_\delta\, v(r) \\
&= (\delta_{\alpha\beta}\delta_{\gamma\delta} + \delta_{\alpha\gamma}\delta_{\beta\delta} + \delta_{\alpha\delta}\delta_{\beta\gamma})\left(-\frac{v'(r)}{r^3} + \frac{v''(r)}{r^2}\right) \\
&+ (\delta_{\alpha\beta}r_\gamma r_\delta + 5\ permutations)\left(\frac{3v'(r)}{r^5} - \frac{3v''(r)}{r^4} + \frac{v'''(r)}{r^3}\right) \\
&+ r_\alpha r_\beta r_\gamma r_\delta \left(-\frac{15v'(r)}{r^7} + \frac{15v''(r)}{r^6} - \frac{6v'''(r)}{r^5} + \frac{v''''(r)}{r^4}\right),
\end{aligned}
\qquad (4.30)
$$

where $v(r)$ can either be electrostatic kernel for spherical truncation or one of the modified (Wolf or DSF) method. Similarly in point dipole representation the qaudrupole-quadrupole interaction tensor can be obtained from the applications

of the two successive gradient in the dipole-dipole interaction tensor,

$$
\begin{aligned}
T_{\alpha\beta\gamma\delta}(r) &= \nabla_\alpha \nabla_\beta\, v_{\gamma\delta}(r) \\
&= \delta_{\alpha\beta}\delta_{\gamma\delta}\frac{v'_{21}(r)}{r} + (\delta_{\alpha\gamma}\delta_{\beta\delta} + \delta_{\alpha\delta}\delta_{\beta\gamma})\,\frac{v_{22}(r)}{r^2} \\
&\quad + \delta_{\gamma\delta}r_\alpha r_\beta \left(\frac{v''_{21}(r)}{r^2} - \frac{v'_{21}(r)}{r^3}\right) \\
&\quad + (\delta_{\alpha\beta}r_\gamma r_\delta + \delta_{\alpha\gamma}r_\beta r_\delta + \delta_{\alpha\delta}r_\gamma r_\beta + \delta_{\beta\gamma}r_\alpha r_\delta + \delta_{\beta\delta}r_\alpha r_\gamma)\left(\frac{v'_{22}(r)}{r^3} - \frac{2v_{22}(r)}{r^4}\right) \\
&\quad + r_\alpha r_\beta r_\gamma r_\delta \left(\frac{v''_{22}(r)}{r^4} - \frac{5v'_{22}(r)}{r^5} + \frac{8v_{22}(r)}{r^6}\right),
\end{aligned}
$$

$$(4.31)$$

where $v_{\gamma\delta}(r)$ is the electrostatic dipole-dipole interaction tensor, which is different for different electrostatic cut off methods. Similarly $v_{21}(r)$ *and* $v_{22}(r)$ are the radial function for different real space cutoff methods defined in Paper I of the series.[?] Using point quadrupole representation the quadrupole-quadrupole interaction can be constructed as,

$$
\begin{aligned}
T_{\alpha\beta\gamma\delta}(r) &= (\delta_{\alpha\beta}\delta_{\gamma\delta} + \delta_{\alpha\gamma}\delta_{\beta\delta} + \delta_{\alpha\delta}\delta_{\beta\gamma})\,v_{41}(r) + \delta_{\gamma\delta}r_\alpha r_\beta\frac{v_{42}(r)}{r^2} \\
&\quad + r_\alpha r_\beta r_\gamma r_\delta \left(\frac{v_{43}(r)}{r^4}\right),
\end{aligned}
$$

$$(4.32)$$

where $v_{41}(r)$, $v_{42}(r)$, and $v_{43}(r)$ are defined in Paper I of the series. [?] They have different functional forms for different electrostatic cutoff methods.

The integral in equation (4.29) can be divided into two parts, $|\mathbf{r} - \mathbf{r}'| \to 0$ and $|\mathbf{r} - \mathbf{r}'| > 0$. Since the total field gradient due to quadrupolar fluid vanishes at the
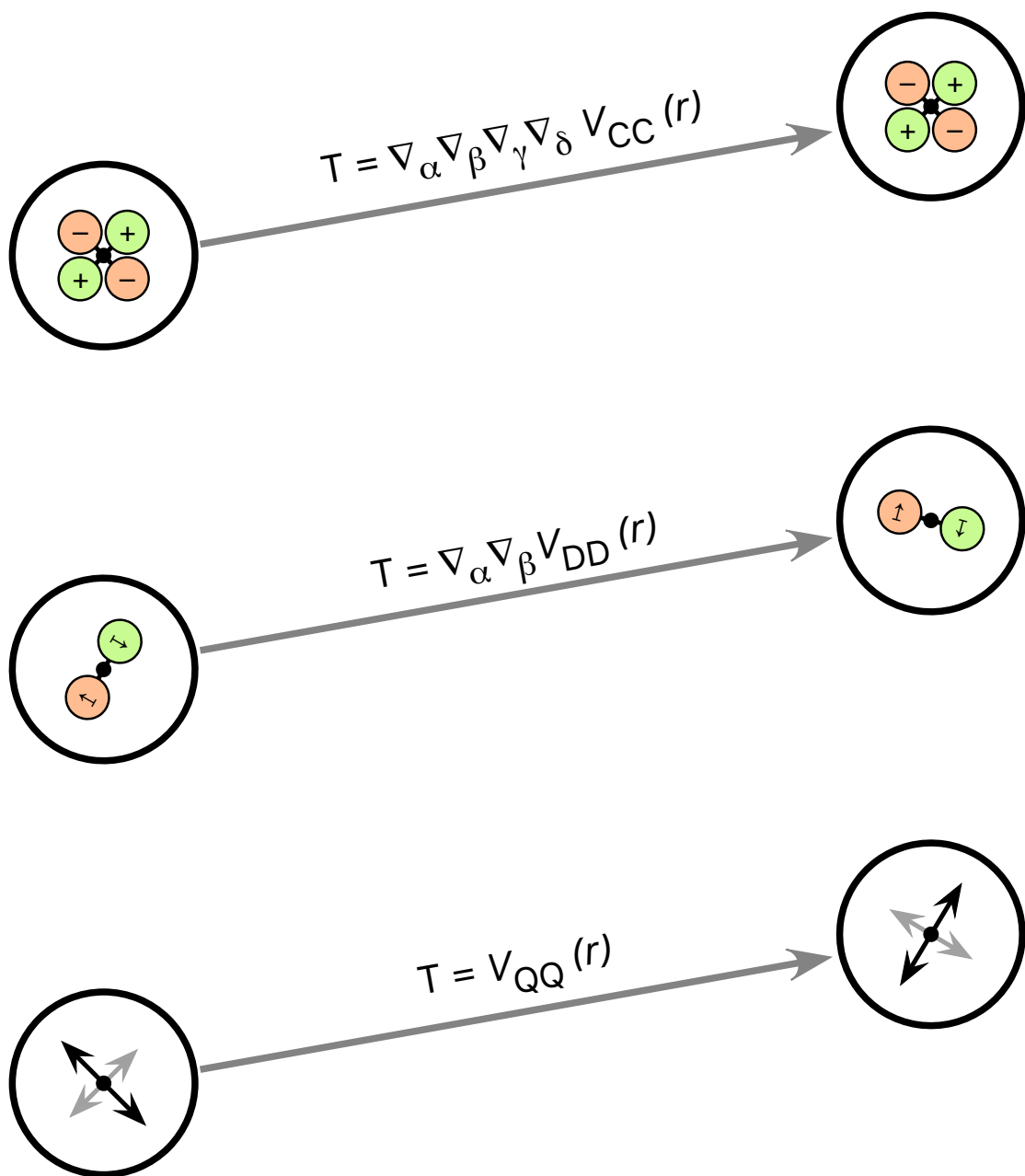
Figure 4.2. With the real-space electrostatic methods, the effective quadrupolar tensor, $\mathbf{T}_{\alpha\beta\gamma\delta}(r)$, governing interactions between molecular quadrupoles can be represented by interaction of charges, point dipoles or single point quadrupoles.

singularity (see Appendix B.2), equation (4.29) can be written as,

$$\partial_\alpha E_\beta(\mathbf{r}) = \partial_\alpha E^o{}_\beta(\mathbf{r}) + \frac{1}{4\pi\epsilon_o} \int\limits_{|\mathbf{r}-\mathbf{r}'|>0} T_{\alpha\beta\gamma\delta}(|\mathbf{r}-\mathbf{r}'|)\, Q_{\gamma\delta}(\mathbf{r}')\, d^3r'. \qquad (4.33)$$

If $\mathbf{r} = \mathbf{r}'$ is excluded from the integration, the gradient of the electric can be expressed in terms of traceless quadrupole moment as below, [45]

$$\partial_\alpha E_\beta(\mathbf{r}) = \partial_\alpha E^o{}_\beta(\mathbf{r}) + \frac{1}{12\pi\epsilon_o} \int\limits_{|\mathbf{r}-\mathbf{r}'|>0} T_{\alpha\beta\gamma\delta}(|\mathbf{r}-\mathbf{r}'|)\, \Theta_{\gamma\delta}(\mathbf{r}')\, d^3r', \qquad (4.34)$$

where $\Theta_{\alpha\beta} = 3Q_{\alpha\beta} - \delta_{\alpha\beta}Tr(Q)$ is the traceless quadrupole moment. The total quadrupolar polarization is written as,

$$Q_{\alpha\beta}(\mathbf{r}) = \frac{1}{3}\delta_{\alpha\beta}\, Tr(Q) + \epsilon_o\chi_Q^*\, \partial_\alpha E_\beta(\mathbf{r}), \qquad (4.35)$$

In the equation (4.35), $\partial_\alpha E_\beta$ is Maxwell field gradient and χ_Q^* is the actual quadrupolar susceptibility of the fluid which is different than the proportionality constant χ_q in the equation (4.16). In terms of traceless quadrupole moment, equation (4.35) can be written as,

$$\frac{1}{3}\Theta_{\alpha\beta}(\mathbf{r}) = \epsilon_o\chi_Q^*\, \partial_\alpha E_\beta(\mathbf{r}) = \epsilon_o\chi_Q^* \left(\partial_\alpha E^o{}_\beta(\mathbf{r}) + \frac{1}{12\pi\epsilon_o} \int\limits_{|\mathbf{r}-\mathbf{r}'|>0} T_{\alpha\beta\gamma\delta}(|\mathbf{r}-\mathbf{r}'|)\, \Theta_{\gamma\delta}(\mathbf{r}')\, d^3r' \right)$$

$$(4.36)$$

For toroidal boundary conditions, both $\partial_\alpha E_\beta$ and $\Theta_{\alpha\beta}$ are uniform over the entire space. After performing a Fourier transform (see the Appendix in the Neumann's

Paper [60]) we get,

$$\frac{1}{3}\Theta_{\alpha\beta}(\kappa) = \epsilon_o\chi_Q^* \left[\partial_\alpha E^o{}_\beta(\kappa) + \frac{1}{12\pi\epsilon_o} T_{\alpha\beta\gamma\delta}(\kappa) \, \Theta_{\gamma\delta}(\kappa) \right] \qquad (4.37)$$

Since the quadrupolar polarization is in the direction of the applied field, we can write $\Theta_{\gamma\delta}(\kappa) = \Theta_{\alpha\beta}(\kappa)$ and $T_{\alpha\beta\gamma\delta}(\kappa) = T_{\alpha\beta\alpha\beta}(\kappa)$. Therefore we can consider each component of the interaction tensor as scalar and perform calculation.

$$\begin{aligned}
\frac{1}{3}\Theta_{\alpha\beta}(\kappa) &= \epsilon_o\chi_Q^* \left[\partial_\alpha E_\beta^o(\kappa) + \frac{1}{12\pi\epsilon_o} T_{\alpha\beta\alpha\beta}(\kappa) \, \Theta_{\alpha\beta}(\kappa) \right] \\
&= \epsilon_o\chi_Q^* \left(1 - \frac{1}{4\pi}\chi_Q^* \, T_{\alpha\beta\alpha\beta}(\kappa) \right)^{-1} \partial_\alpha E_\beta^o(\kappa)
\end{aligned} \qquad (4.38)$$

If the field gradient is homogeneous over the entire volume, $\partial_\alpha E_\beta(\kappa) = 0$ except at $\kappa = 0$, hence it is sufficient to know $T_{\alpha\beta\alpha\beta}(\kappa)$ at $\kappa = 0$. Therefore equation (4.38) can be written as,

$$\frac{1}{3}\Theta_{\alpha\beta}(0) = \epsilon_o\chi_Q^* \left(1 - \frac{1}{4\pi}\chi_Q^* \, T_{\alpha\beta\alpha\beta}(0) \right)^{-1} \partial_\alpha E_\beta^o(0) \qquad (4.39)$$

where $T_{\alpha\beta\alpha\beta}(0)$ can be evaluated as,

$$T_{\alpha\beta\alpha\beta}(0) = \int T_{\alpha\beta\alpha\beta}(\mathbf{r})d^3r \qquad (4.40)$$

In terms of traced quadrupole moment equation (4.39) can be written as,

$$Q_{\alpha\beta} = \frac{1}{3}\delta_{\alpha\beta} \, Tr(Q) + \epsilon_o \, \chi_Q^* \left(1 - \frac{1}{4\pi}\chi_Q^* \, T_{\alpha\beta\alpha\beta}(0) \right)^{-1} \partial_\alpha E_\beta^o \qquad (4.41)$$

Comparing (4.41) and (4.15) we get,

$$
\begin{aligned}
\frac{\langle Q^2 \rangle - \langle Q \rangle^2}{15\epsilon_o V k_B T} &= \chi_Q^* \left(1 - \frac{1}{4\pi} \chi_Q^* \, T_{\alpha\beta\alpha\beta}(0) \right)^{-1}, \\
\chi_Q^* &= \frac{\langle Q^2 \rangle - \langle Q \rangle^2}{15\epsilon_o V k_B T} \left(1 + \frac{1}{4\pi} \frac{\langle Q^2 \rangle - \langle Q \rangle^2}{15\epsilon_o V k_B T} \, T_{\alpha\beta\alpha\beta}(0) \right)^{-1}
\end{aligned}
\tag{4.42}
$$

Finally the quadrupolar susceptibility cab be written in terms of quadrupolar correction factor (A_{quad}) as below,

$$
\chi_Q^* = \frac{\langle Q^2 \rangle - \langle Q \rangle^2}{15\epsilon_o V k_B T} \left(1 + \frac{\langle Q^2 \rangle - \langle Q \rangle^2}{15\epsilon_o V k_B T} A_{quad} \right)^{-1} = \alpha_Q \left(1 + \alpha_Q \, A_{quad} \right)^{-1} \tag{4.43}
$$

where $A_{quad} = \frac{1}{4\pi} \int T_{\alpha\beta\alpha\beta}(\mathbf{r}) d^3 r$ has dimension of the $length^{-2}$ is different for different cutoff methods which is listed in Table 4.2. The dielectric constant associated with the quadrupolar susceptibility is defined as,[21]

$$
\epsilon = 1 + \chi_Q^* \, G = 1 + G \, \alpha_Q \left(1 + \alpha_Q \, A_{quad} \right)^{-1} \tag{4.44}
$$

where $G = \dfrac{\displaystyle\int_V |\partial_\alpha E_\beta^o|^2 d^3 r}{\displaystyle\int_V |E^o|^2 d^3 r}$ is a geometrical factor depends on the nature of the external field perturbation. This is true when the quadrupolar fluid is homogeneous over the sample. Since quadrupolar molecule couple with the gradient of the field, the distribution of the quadrupoles is inhomogeneous for varying field gradient. Hence the distribution function should also be taken into account to calculate actual geometrical factor in the presence of non-uniform gradient field. Therefore,

$$
G = \frac{\displaystyle\int_V g(r, \theta, \phi) \, |\partial_\alpha E_\beta^o|^2 d^3 r}{\displaystyle\int_V |E^o|^2 d^3 r} \tag{4.45}
$$

where $g(r, \theta, \phi)$ is a distribution function of the quadrupoles in with respect to origin at the center of line joining two probe charges.

4.6 Methodology

We have used three different simulation methods: i) external field perturbation, ii) fluctuation formula, and iii) potential of mean force (PMF), to calculate dielectric properties for dipolar and quadrupolar fluid. For the dipolar system we calculated macroscopic polarzability using first two methods and derived the dielectric constant using polarizability and correction factor (see equation 4.28). Similarly we used equation (4.17) to calculate screening factor from dipolar fluid using PMF method. For quadrupolar fluid, we have calculated quadrupolarizablity using fluctuation formula and external field perturbation and derived quadrupolar susceptibility using quadrupolarizability and correction factor (equation 4.43). Since dielectric constant due to quadrupolar fluid depends on the nature of gradient of the field applied in the system, we have used geometrical factor (in equation 4.45) and quadrupolar susceptibility to evaluate dielectric constant for two ions dissolved quadrupolar fluid (see equation 4.44) . The the dielectric constant evaluated using equation (4.44) has been compared with the result evaluated from PMF method (i.e. equation 4.17). We have also used three different test systems for both dipolar and quadrupolar fluids to calculate dielectric properties. The parameters used in the test systems are given in table 4.3.

First test system consists of point dipolar or quadrupolar molecules in the presence of constant field or gradient field. Since there is no isolated charge within the system, the divergence of the field should be zero $i.e. \vec{\nabla}.\vec{E} = 0$. This condition is satisfied by selecting applied potential as described in Appendix B.3. When

TABLE 4.2: Expressions for the quadrupolar correction factor (A) for the real-space electrostatic methods in terms of the damping parameter (α) and the cutoff radius (r_c). The dimension of the correction factor is $length^{-2}$ in case of quadrupolar fluid.

Method	A_{charges}	A_{dipoles}	$A_{\text{quadrupoles}}$
Spherical Cutoff (SC)	$-\frac{8\alpha^5 r_c^3}{3\sqrt{\pi}} e^{-\alpha^2 r_c^2}$	$-\frac{8\alpha^5 r_c^3}{3\sqrt{\pi}} e^{-\alpha^2 r_c^2}$	$-\frac{8\alpha^5 r_c^3}{3\sqrt{\pi}} e^{-\alpha^2 r_c^2}$
Shifted Potental (SP)	$-\frac{8\alpha^5 r_c^3}{3\sqrt{\pi}} e^{-\alpha^2 r_c^2}$	$-\frac{8\alpha^5 r_c^3}{3\sqrt{\pi}} e^{-\alpha^2 r_c^2}$	$-\frac{16\alpha^7 r_c^5}{9\sqrt{\pi}} e^{-\alpha^2 r_c^2}$
Gradient-shifted (GSF)	$-\frac{8\alpha^5 r_c^3}{3\sqrt{\pi}} e^{-\alpha^2 r_c^2}$	0	$-\frac{4\alpha^7 r_c^5}{9\sqrt{\pi}} e^{-\alpha^2 r_c^2}(-1 + 2\alpha^2 r_c^2)$
Taylor-shifted (TSF)	$-\frac{8\alpha^5 r_c^3}{3\sqrt{\pi}} e^{-\alpha^2 r_c^2}$	$\frac{4\,\text{erfc}(\alpha r_c)}{r_c^2} + \frac{8\alpha}{3\sqrt{\pi}r_c} e^{-\alpha^2 r_c^2}\left(3 + 2\alpha^2 r_c^2 + \alpha^4 r_c^4\right)$	$\frac{10\,\text{erfc}(\alpha r_c)}{r_c^2} + \frac{4\alpha}{9\sqrt{\pi}r_c} e^{-\alpha^2 r_c^2}\left(45 + 30\alpha^2 r_c^2 + 12\alpha^4 r_c^4 + 3\alpha^6 r_c^6 + 2\alpha^8 r_c^8\right)$

TABLE 4.3: The mass, moment of intertia, Lennard-Jones, and electrostatic parameters for the test systems are listed below.

Test system	LJ parameters		Electrostatic moments					mass	I_{xx}	I_{yy}	I_{zz}
	σ (Å)	ϵ (kcal/mol)	C (e)	D (debye)	Q_{xx}	Q_{yy} (debye Å)	Q_{zz}	(amu)		(amu Å^2)	
Stockmayer fluid	3.41	0.2381	-	1.4026	-	-	-	39.948	11.613	11.613	0.0
Quadrupolar fluid	2.985	0.265	-	-	0.0	0.0	-2.139	18.0153	43.0565	43.0565	0.0
q+	1.0	0.1	+1	-	-	-	-	22.98	-	-	-
q-	1.0	0.1	-1	-	-	-	-	22.98	-	-	-

constant electric field or field gradient applied to the system, the molecules align along the direction of the applied field. We have calculated ensemble average of the box dipole or quadrupole moment as a response field or field gradient. Similarly the macroscopic polarizability of the system is derived using ratio between system multipolar moment and applied field or field gradient. This method works properly when the system is at the linear response region of field or field gradient.

Second test system consists of box of point dipolar or quadrupolar molecules is simulated for 1 ns in NVE ensemble after equilibration in the absence of any external perturbation. The fluctuation of the ensemble average of the box multipolar moment, $\langle A^2 \rangle - \langle A \rangle^2$ where A is box dipolar or quadrupolar moment, is measured at the fixed temperature and density for a given multipolar fluid. Finally the macroscopic polarizability of the system at a particular density is derived using equation (4.15).

Final system consists of dipolar or quadrupolar fluids with two oppositely charged ions immersed in it. These ions are constraint to be at fixed distance throughout the simulation. We run separate simulations for the different constraint distances. We calculated the screening factor using ratio between the force between the two ions in the absence of medium and the average constraint force during the simulation. Since the constraint force is pretty noisy we run each simulation for long time (~ 5 ns) to reduce simulation error.

4.6.1 Implementation

We have used real-space electrostatic methods implemented in OpenMD [**?**] software to evaluate electrostatic interactions between the molecules. In our simulations we used all three different real-space electrostatic methods: SP, GSF,

and TSF developed in the previous paper [?] in the series. The radius of the cutoff sphere is taken to be $12\mathring{A}$. Each real space method can be tuned using different values of damping parameter. We have selected ten different values of damping parameter (unit-$\mathring{A}^{-1}$); 0.0, 0.05, 0.1, 0.15, 0.175, 0.2, 0.225, 0.25, 0.3, and 0.35 in our simulations for dipolar system. Since quadrupolar interactions are less sensitive to damping parameter as compared to dipole we selected only four values of dampig alpha 0.0, 0.1 0.2, and 0.3 $\mathring{A} - 1$ in our simulation. The short range interaction in the simulations is incorporated using 6-12 Lennard Jones interactions.

To derive the box multipolar (dipolar or quadrupolar) moment, we added the component each individual molecule and taken ensemble average of each snapshot in the entire simulation. The first component of the fluctuation of the dipolar moment is derived by using relation $\langle M^2 \rangle = \langle M_x{}^2 + M_y{}^2 + M_z{}^2 \rangle$, where M_x, M_y, and M_z are x, y and z components of the box dipolar moment. Similarly the first term in the quadrupolar system is derived using relation $\langle Q^2 \rangle = \langle 3Q : Q - \mathrm{Tr}Q^2 \rangle$, where Q is the box quadrupole moment, double dot represent the outer product of the quadrupolar matrices, and TrQ is the trace of the box quadrupolar moment. The second component of the fluctuation formula has been derived using square of the ensemble average of the box dipole moment. The applied constant field or field gradient in the test systems has been taken in the form described in the Appendix B.3.

4.6.2 Model systems

To evaluate dielectric properties for dipolar systems using perturbation and fluctuation formula methods, we have taken system of 2048 Stockmayer molecules

with reduced density $\rho^* = 0.822$, temperature $T^* = 1.15$, moment of inertia $I^* = 0.025$, and dipole moment $\mu^* = \sqrt{3.0}$. Test systems are equilibrated for 500 ps and run for 1 ns and components of box dipole moment are obtained at every femtosecond. The systems have been run in the presence of constant external field from $0 - 10 \times 10^{-4}$ $V/\mathring{A}$ in the step of 10^{-4} $V/\mathring{A}$ for each simulation. For pmf method, Two dipolar molecules in the above system are converted into $q+$ and $q-$ ions and constrained to remain in fixed distance in simulation. The constrained distance is varied from 5 $\mathring{A} - 12$ $\mathring{A}$ for different simulations. In pmf method all simulations are equilibrated for 500 ps in NVT ensemble and run for 5 ns in NVE ensemble to print constraint force at an interval of 20 fs.

Quadrupolar systems consists 4000 linear point quadrupoles with density 2.338 g/cm^3 at temperature 500 ^oK. For both perturbation and fluctuation methods, test systems are equalibrated for 200 ps in NVT ensemble and run for 500 ps in NVE ensemble. To find the ensemble average of the box quadrupole moment and fluctuation, the components of box quadrupole moments are printed every 100 fs. Each simulations repeated at different values of applied gradients from $0-9\times10^{-2}$ $V/\mathring{A}^2$. To calculate dielectric constant using pmf method, two ions in the systems are converted into $q+$ and $q-$ ions and constrained to remain at fixed distance in the simulation. These constraint distances are varied from 5 $\mathring{A} - 12$ $\mathring{A}$ at the step of 0.1 $\mathring{A}$ for different simulations. For calculating dielectric constant, the test systems are run for 500 ps to equlibrate and run for 5 ns to print constraint force at a time interval of 20 fs.

4.7 Results

4.7.1 Dipolar fluid

The macroscopic polarizability (α_D) for Stockmayer fluid evaluated using perturbation (left) and fluctuation (right) methods as shown in figure 4.3 . The polarizability obtained from the both perturbation and fluctuation methods show excellent agreement with each other. The result shows that polarizability hugely depends on the values of the damping parameter in the case of Shifted Potential (SP) and Gradient Shifted force (GSF) methods. But the results obtained using Taylor Shifted Force (TSF) show slight dependence on the damping alpha. To get correct dielectric properties from the polarizability we used a correction factor as we discussed in section 4.5. The correction factor for dipolar fluids (A_{dipole}) for the different values of damping parameter is also plotted in figure 4.3. For TSF method, $A_{dipole} = 1$ for all the values of damping alpha. Therefore we do not need to perform any correction to obtain dielectric constant from the polarizability. The values of A_{dipole} varies with the damping parameter in the case of SP and GSF methods therefore correction factor should be incorporated to calculate the dielectric constant (ϵ) from the polarzability. The dielectric constant obtained from the polarizability and correction factor is also plotted in the figure 4.3. The dielectric constant evaluated using SP and GSF method shows good agreement with the previous simulation result (straight dotted line in the lower panels)[60] for the damping parameter from 0.25 to 0.3 $\mathring{A} - 1$. For lower value of the damping alpha the dielectric constant is much deviated away from the previous simulation result. To investigate furthermore we performed inverse transformation of expected dielectric constant [60], using correction factor and calculated expected polarizability for the simulation, which is represented by the

110

dotted line in the upper-left and upper-right panels. In the plot we can clearly see that expected ploarizability for the SP and GSF methods are very close to results obtained from the simulations. Sometime even they are within the range of the error-bar but when the dielectric constant is calculated using simulation result and correction formula, it is found to be deviated much away from the expected result for the lower values of the damping alpha. This tell us that the correction formula (equation 4.28) for the dipolar fluid is very sensitive when the value of A_{dipole} is deviated much away from 1 for the small values of damping parameter. Therefore it is always better to select damping alpha from 0.25 to 0.3 $\mathring{A}^{-1}$ to evaluate dielectric constant using perturbation and fluctuation formula while using SP and GSF methods in simulation.

We have also evaluated the screening factor between two oppositely charged ions when they are placed in the Stockmayer fluid as shown in figure 4.4. The screening factor have been evaluated using equation 4.17. This screening factor is analogous to dielectric screening but there is subtle differences between them. Actually screening factor measures a local property of the ions in the fluid and depends on ion-dipole and dipole-dipole interactions. These interactions depends on the distance between ions and electrostatic interaction methods implemented in the simulations. But we can expect screening to be close to dielectric constant when the field due to ions is very gentle in perturbation. It is possible when distance between ions are far apart and values of damping parameter relatively higher. In the figure 4.4 we can observe that for the higher value of damping alpha i.e $\alpha = 0.2\mathring{A}^{-1}$ and $0.3\mathring{A}^{-1}$ and large separation between ions, the screening factor approaches to the dielectric constant. We can also observe that for TSF method has got higher screening factor as compared SP and GSF method even

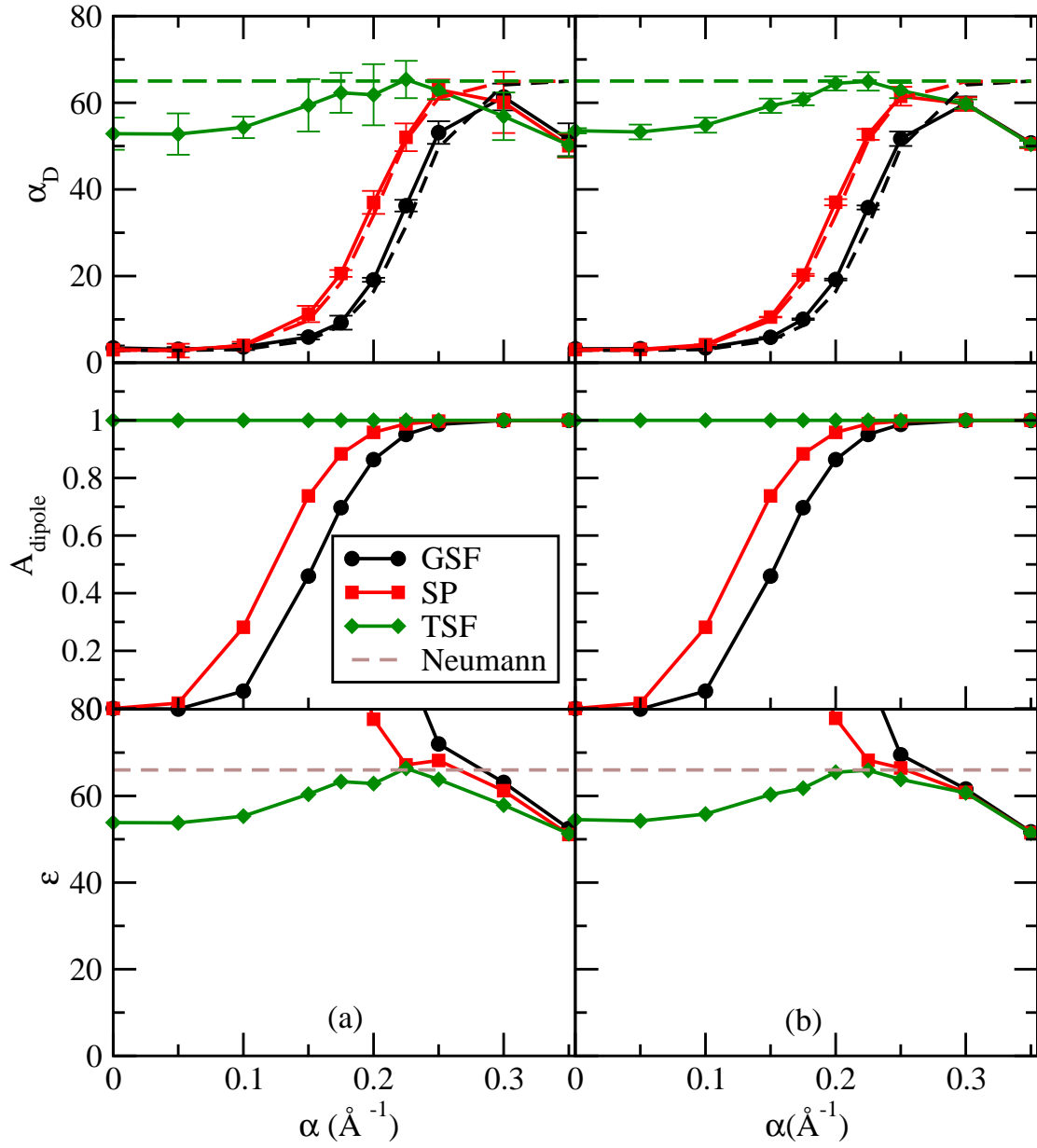Figure 4.3. In the figure, α_D, A_{dipole}, and ϵ are polarizability, correction factor, and dielectric constant for Stockmayer fluid. Plots in the left panel show results for (a) perturbation method and right (b) fluctuation method.

for lower damping alpha. It is because of dipole-dipole interactions do not need any correction factor in the case of TSF as we discussed earlier. But presence of ion-dipole interaction causing local effect even in the case of TSF method for small ions separation.

4.7.2 Quadrupolar fluid

The polarizability (α_Q), correction factor (A_{quad}), and susceptibility (χ) for the quadrupolar fluid is plotted against damping parameter in the figure 4.5. Different than the dipolar fluid, the polarizability and susceptibility for the quadrupolar fluid have a dimension of $\mathring{A}^2$. Although susceptibility has got dimension, it is a measure of macroscopic quadrupolar properties at a given temperature and density [39, 40]. The left panel in the plot showing results obtained from the perturbation whereas the results from the fluctuation formula are plotted in the right panel. In the figure, we can observe that the polarizablity evaluated from the perturbation (top-left) shows excellent agreement with the result obtained from the fluctuation formula (top-right). The susceptibility for the quadrupolar fluid is obtained from quadrupolarizability and correction factor using equation 4.43 which is plotted at the bottom-left and bottom-right in the figure 4.5. All three methods: SP, GSF, and TSF tends to produce same value of susceptibility for the given value damping alpha. This shows that susceptibility derived using correction factor and polarizablity is tends to be independent of the electrostatic method implemented in the simulation for quadrupolar fluid.

The actual test of the susceptibility can be made by comparing the results obtained from the perturbation and fluctuation with the result calculated from more direct, potential of mean force (PMF), method. For this purpose, we have
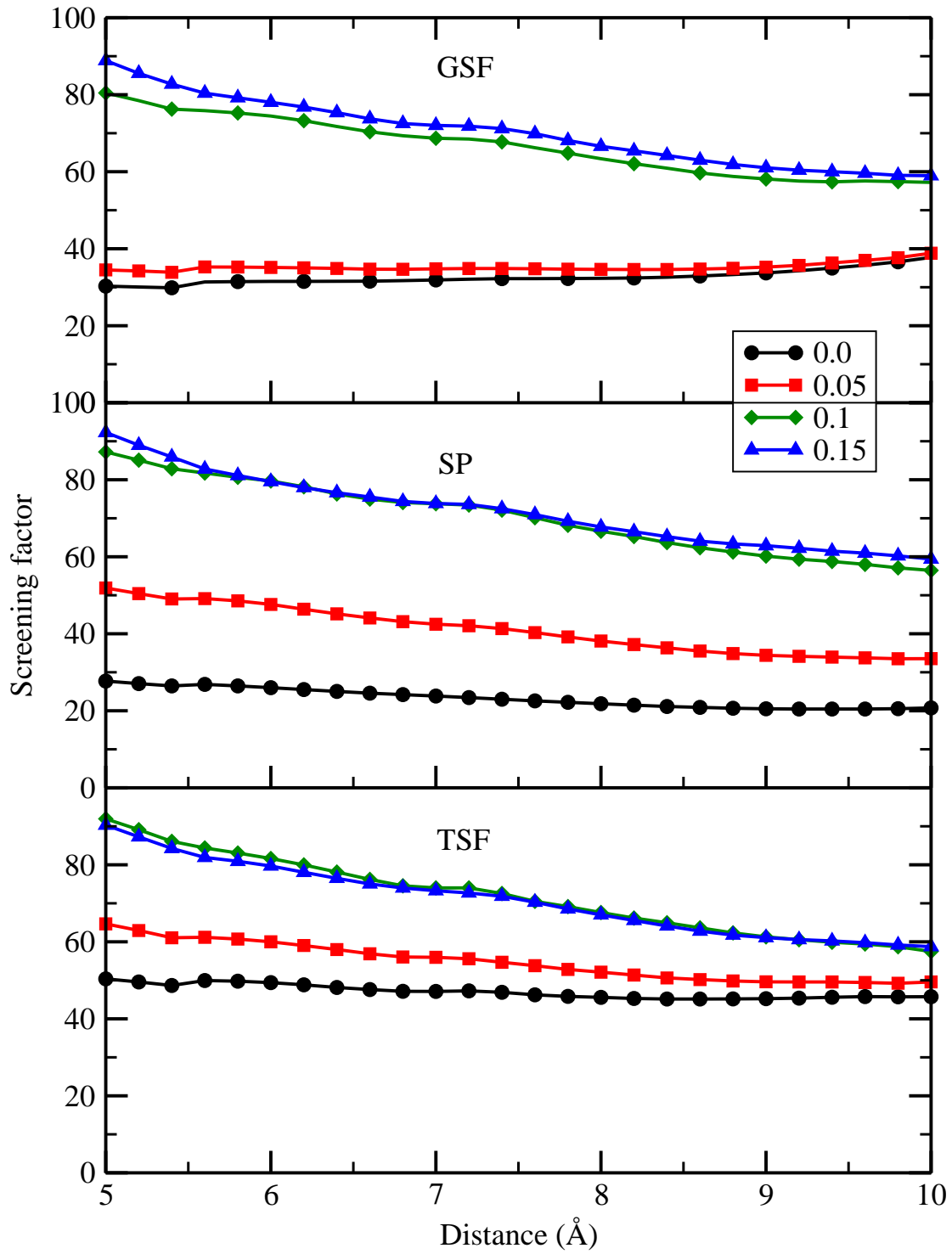
Figure 4.4. Figure shows screening factor between two oppositely charged ions immersed in Stockmayer fluid as a function of ions-separation for the different values damping alpha and electrostatic methods.

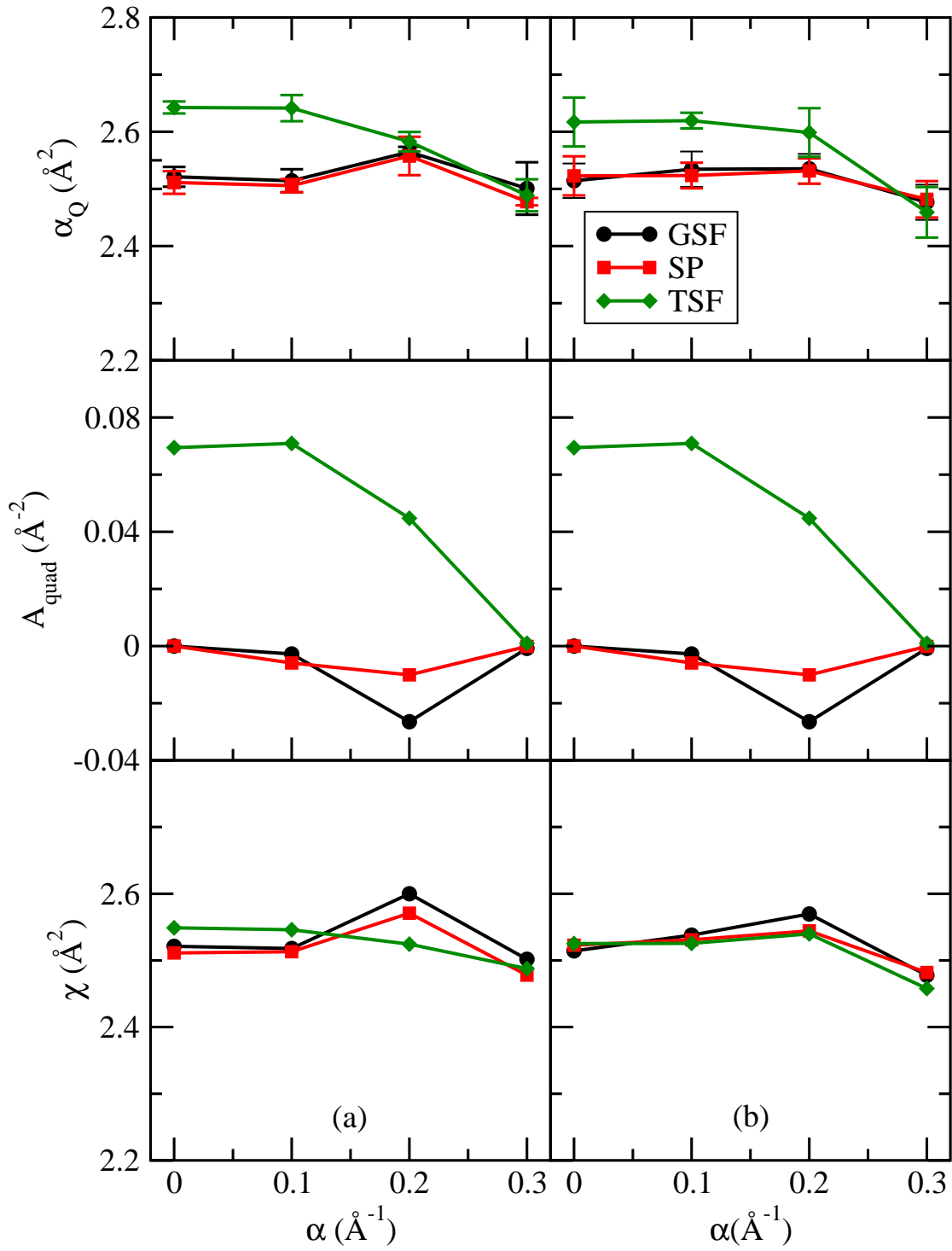Figure 4.5. In the figure, α_Q, A_{quad}, and χ are polarizability, correction factor, and susceptibility for the quadrupolar fluid. Plots in the left panel show results for (a) perturbation method and right (b) fluctuation method.

calculated the expected dielectric constant from the susceptibility and geometrical factor using equation 4.44. Since the dielectric constant for quadrupolar fluid is geometry-dependent, it is not a actual measure of the property of the quadrupolar fluid. This geometrical factor varies with the variation in ions separation as well as damping parameter therefore the dielectric constant can be refereed as screening factor. The screening factor plotted against ions separation, evaluated from the perturbation and fluctuation method are shown in right and central panel of the figure 4.6. Here the susceptibility is calculated from the simulation and the geometrical factor is evaluated analytically, using field and field-gradient produced by ions. The right hand panel shows screening factor plotted against ions separation, for the different values of the damping alpha, obtained from the PMF method. The figure clearly shows that the screening factor obtained from the perturbation and fluctuation formula shows good agreement with the screening factor calculated using PMF method. Since there is no huge differences in quadrupole-quadruople interactions for various real-space methods, we do not observe large differences in the screen factors for SP, GSF, and TSF methods.

4.8   Summary

We have used the perturbation and fluctuation formula to evaluate dielectric properties for dipolar and quadrupolar fluids implementing SP, GSF, and TSF methods in the simulation. Similarly the correction factors for the both dipolar and quadrupolar systems have also been calculated for all SP, GSF, and TSF methods. We have also derived screening factor between two ions immersed in the dipolar and quadrupolar fluids using PMF method. The result from the perturbation and fluctuation formula are compared with PMF method to test the
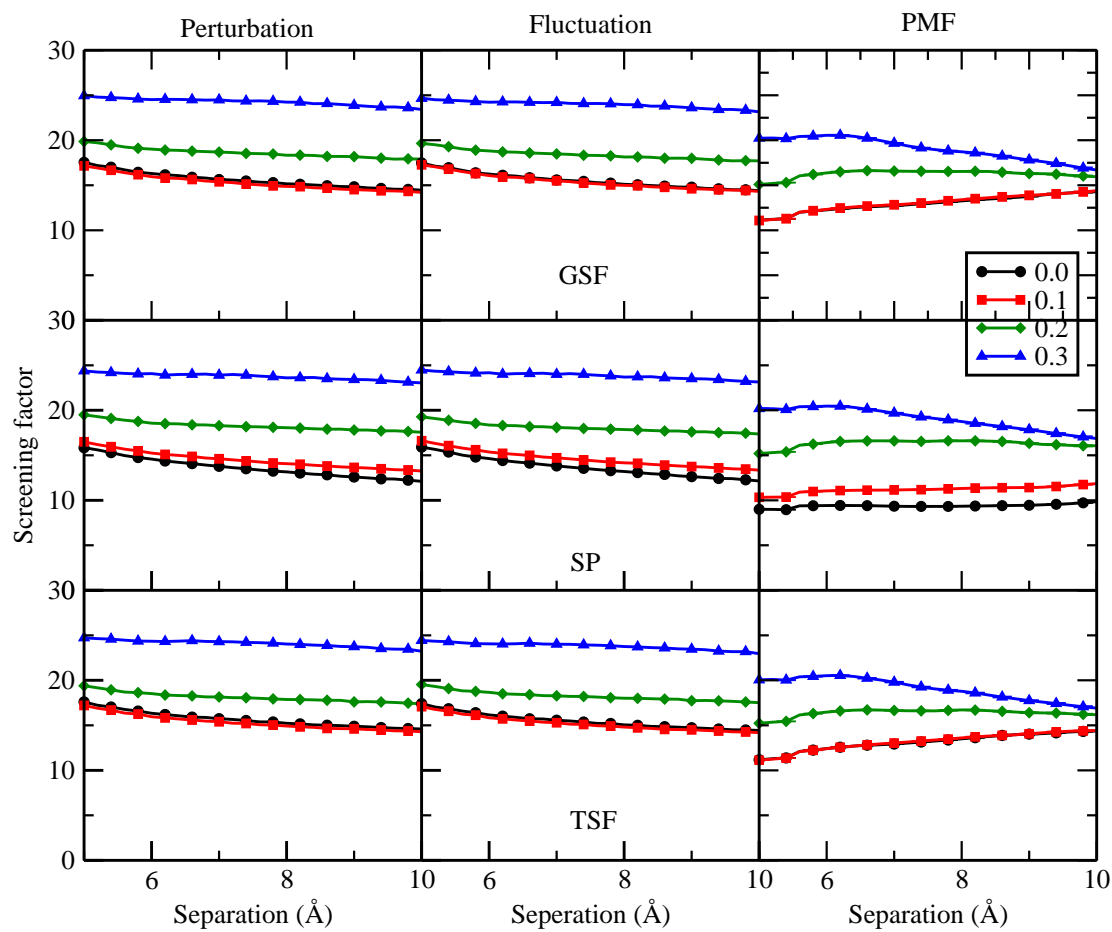
Figure 4.6.

accuracy of the simulation result.

For the dipolar fluid, the polarizability evaluated using the perturbation and fluctuation methods show excellent agreement with each other. The dielectric constant evaluated using polarizability and correction factor agree with the previous simulation results [60] for the damping parameter 0.25 - $0.3 \mathring{A}^{-1}$ and the electrostatic interaction methods, SP and GSF implemented in the simulation. Since the correction factor for TSF, $A_{\text{dipole}} = 1$, it produces dielectric constant more closer to previous simulation results [60] for all values damping parameter. This method also produces best dielectric constant for damping parameter 0.15 - $0.25 \mathring{A}^{-1}$. We have also found that correction formula (equation 4.28) is very sensitive, when the correction factor (A_{dipole}) much away from the 1 for the SP and GSF methods. Therefore it is better to choose damping parameter from 0.25 - $0.3 \mathring{A}^{-1}$ to evaluate dielectric constant using SP and GSF methods. The screening factor between ions is found to be closer to dielectric constant when the distance between the ions are far apart ($\sim 9 \mathring{A}$) and damping parameter 0.2 to $0.3 \mathring{A}^{-1}$.

The quadpolarizability evaluated from the both perturbation and fluctuation methods shows excellent agreement with each other for the case of quadrupolar fluid. The susceptibility is calculated from the quadpolarizability and correction factor tends to produce same result for all; SP, GSF, and TSF, methods. Similarly the screening factor calculated using susceptibility and geometrical factor shows excellent agreement with the result obtained from the PMF method.

APPENDIX A

RADIAL FUNCTIONS FOR REAL-SPACE ELECTROSTATIC METHODS

A.1   Smith's $B_l(r)$ functions for damped-charge distributions

The following summarizes Smith's $B_l(r)$ functions and includes formulas given in his appendix.[83] The first function $B_0(r)$ is defined by

$$B_0(r) = \frac{\text{erfc}(\alpha r)}{r} = \frac{2}{\sqrt{\pi} r} \int_{\alpha r}^{\infty} e^{-s^2} ds. \tag{A.1}$$

The first derivative of this function is

$$\frac{dB_0(r)}{dr} = -\frac{1}{r^2} \text{erfc}(\alpha r) - \frac{2\alpha}{r\sqrt{\pi}} e^{-\alpha^2 r^2} \tag{A.2}$$

which can be used to define a function $B_1(r)$:

$$B_1(r) = -\frac{1}{r} \frac{dB_0(r)}{dr} \tag{A.3}$$

In general, the recurrence relation,

$$B_l(r) = -\frac{1}{r} \frac{dB_{l-1}(r)}{dr} = \frac{1}{r^2} \left[(2l-1)B_{l-1}(r) + \frac{(2\alpha^2)^l}{\alpha\sqrt{\pi}} e^{-\alpha^2 r^2} \right], \tag{A.4}$$

is very useful for building up higher derivatives. As noted by Smith, it is possible to approximate the $B_l(r)$ functions,

$$B_l(r) = \frac{(2l)!}{l!2^l r^{2l+1}} - \frac{(2\alpha^2)^{l+1}}{(2l+1)\alpha\sqrt{\pi}} + \mathrm{O}(r). \qquad (A.5)$$

A.2 The r-dependent factors for TSF electrostatics

Using the shifted damped functions $f_n(r)$ defined by:

$$f_n(r) = B_0(r) - \sum_{m=0}^{n+1} \frac{(r - r_c)^m}{m!} B_0^{(m)}(r_c), \tag{A.6}$$

where the superscript (m) denotes the mth derivative. In this Appendix, we provide formulas for successive derivatives of this function. (If there is no damping, then $B_0(r)$ is replaced by $1/r$.) First, we find:

$$\frac{\partial f_n}{\partial r_\alpha} = \hat{r}_\alpha \frac{df_n}{dr}. \tag{A.7}$$

This formula clearly brings in derivatives of Smith's $B_0(r)$ function, and we define higher-order derivatives as follows:

$$g_n(r) = \frac{df_n}{dr} = B_0^{(1)}(r) - \sum_{m=0}^{n} \frac{(r - r_c)^m}{m!} B_0^{(m+1)}(r_c) \tag{A.8}$$

$$h_n(r) = \frac{d^2 f_n}{dr^2} = B_0^{(2)}(r) - \sum_{m=0}^{n-1} \frac{(r - r_c)^m}{m!} B_0^{(m+2)}(r_c) \tag{A.9}$$

$$s_n(r) = \frac{d^3 f_n}{dr^3} = B_0^{(3)}(r) - \sum_{m=0}^{n-2} \frac{(r - r_c)^m}{m!} B_0^{(m+3)}(r_c) \tag{A.10}$$

$$t_n(r) = \frac{d^4 f_n}{dr^4} = B_0^{(4)}(r) - \sum_{m=0}^{n-3} \frac{(r - r_c)^m}{m!} B_0^{(m+4)}(r_c) \tag{A.11}$$

$$u_n(r) = \frac{d^5 f_n}{dr^5} = B_0^{(5)}(r) - \sum_{m=0}^{n-4} \frac{(r - r_c)^m}{m!} B_0^{(m+5)}(r_c). \tag{A.12}$$

We note that the last function needed (for quadrupole-quadrupole interactions) is

$$u_4(r) = B_0^{(5)}(r) - B_0^{(5)}(r_c). \tag{A.13}$$

The functions $f_n(r)$ to $u_n(r)$ can be computed recursively and stored on a grid for values of r from 0 to r_c. Using these functions, we find

$$\frac{\partial f_n}{\partial r_\alpha} = r_\alpha \frac{g_n}{r} \tag{A.14}$$

$$\frac{\partial^2 f_n}{\partial r_\alpha \partial r_\beta} = \delta_{\alpha\beta} \frac{g_n}{r} + r_\alpha r_\beta \left(-\frac{g_n}{r^3} + \frac{h_n}{r^2} \right) \tag{A.15}$$

$$\frac{\partial^3 f_n}{\partial r_\alpha \partial r_\beta \partial r_\gamma} = (\delta_{\alpha\beta} r_\gamma + \delta_{\alpha\gamma} r_\beta + \delta_{\beta\gamma} r_\alpha) \left(-\frac{g_n}{r^3} + \frac{h_n}{r^2} \right)$$
$$+ r_\alpha r_\beta r_\gamma \left(\frac{3g_n}{r^5} - \frac{3h_n}{r^4} + \frac{s_n}{r^3} \right) \tag{A.16}$$

$$\frac{\partial^4 f_n}{\partial r_\alpha \partial r_\beta \partial r_\gamma \partial r_\delta} = (\delta_{\alpha\beta} \delta_{\gamma\delta} + \delta_{\alpha\gamma} \delta_{\beta\delta} + \delta_{\beta\gamma} \delta_{\alpha\delta}) \left(-\frac{g_n}{r^3} + \frac{h_n}{r^2} \right)$$
$$+ (\delta_{\alpha\beta} r_\gamma r_\delta + 5 \text{ permutations}) \left(\frac{3g_n}{r^5} - \frac{3h_n}{r^4} + \frac{s_n}{r^3} \right)$$
$$+ r_\alpha r_\beta r_\gamma r_\delta \left(-\frac{15g_n}{r^7} + \frac{15h_n}{r^6} - \frac{6s_n}{r^5} + \frac{t_n}{r^4} \right) \tag{A.17}$$

$$\frac{\partial^5 f_n}{\partial r_\alpha \partial r_\beta \partial r_\gamma \partial r_\delta \partial r_\epsilon} = (\delta_{\alpha\beta} \delta_{\gamma\delta} r_\epsilon + 14 \text{ permutations}) \left(\frac{3g_n}{r^5} - \frac{3h_n}{r^4} + \frac{s_n}{r^3} \right)$$
$$+ (\delta_{\alpha\beta} r_\gamma r_\delta r_\epsilon + 9 \text{ permutations}) \left(-\frac{15g_n}{r^7} + \frac{15h_n}{r^7} - \frac{6s_n}{r^5} + \frac{t_n}{r^4} \right)$$
$$+ r_\alpha r_\beta r_\gamma r_\delta r_\epsilon \left(\frac{105g_n}{r^9} - \frac{105h_n}{r^8} + \frac{45s_n}{r^7} - \frac{10t_n}{r^6} + \frac{u_n}{r^5} \right)$$

$$\tag{A.18}$$

A.3 The r-dependent factors for GSF electrostatics

In Gradient-shifted force electrostatics, the kernel is not expanded, and the expansion is carried out on the individual terms in the multipole interaction energies. For damped charges, this still brings multiple derivatives of the Smith's $B_0(r)$ function into the algebra. To denote these terms, we generalize the notation of the previous appendix. For either $f(r) = 1/r$ (undamped) or $f(r) = B_0(r)$ (damped),

$$g(r) = \frac{df}{dr} \qquad\qquad = -\frac{1}{r^2} \quad \text{or} \quad -rB_1(r) \tag{A.19}$$

$$h(r) = \frac{dg}{dr} = \frac{d^2 f}{dr^2} = \frac{2}{r^3} \quad \text{or} \quad -B_1(r) + r^2 B_2(r) \tag{A.20}$$

$$s(r) = \frac{dh}{dr} = \frac{d^3 f}{dr^3} = -\frac{6}{r^4} \quad \text{or} \quad 3rB_2(r) - r^3 B_3(r) \tag{A.21}$$

$$t(r) = \frac{ds}{dr} = \frac{d^4 f}{dr^4} = \frac{24}{r^5} \quad \text{or} \quad 3B_2(r) - 6r^2 B_3(r) + r^4 B_4(r) \tag{A.22}$$

$$u(r) = \frac{dt}{dr} = \frac{d^5 f}{dr^5} = -\frac{120}{r^6} \quad \text{or} \quad -15rB_3(r) + 10r^3 B_4(r) - r^5 B_5(r). \tag{A.23}$$

For undamped charges, Table I lists these derivatives under the Bare Coulomb column. Equations A.14 to A.18 are still correct for GSF electrostatics if the subscript n is eliminated.

APPENDIX B

POINT MULTIPOLES, FIELD, AND FIELD GRADIENT

B.1 Point-multipolar interactions with a spatially-varying electric field

We can treat objects a, b, and c containing embedded collections of charges. When we define the primitive moments, we sum over that collections of charges using a local coordinate system within each object. The point charge, dipole, and quadrupole for object a are given by C_a, $\mathbf{D}_a$, and Q_a, respectively. These are the primitive multipoles which can be expressed as a distribution of charges,

$$C_a = \sum_{k\,\text{in}\,a} q_k, \tag{B.1}$$

$$D_{a\alpha} = \sum_{k\,\text{in}\,a} q_k r_{k\alpha}, \tag{B.2}$$

$$Q_{a\alpha\beta} = \frac{1}{2} \sum_{k\,\text{in}\,a} q_k r_{k\alpha} r_{k\beta}. \tag{B.3}$$

Note that the definition of the primitive quadrupole here differs from the standard traceless form, and contains an additional Taylor-series based factor of $1/2$. In Paper 1, we derived the forces and torques each object exerts on the others.

Here we must also consider an external electric field that varies in space: $\mathbf{E}(\mathbf{r})$. Each of the local charges q_k in object a will then experience a slightly different field. This electric field can be expanded in a Taylor series around the local origin of each object. A different Taylor series expansion is carried out for each object.

For a particular charge q_k, the electric field at that site's position is given by:

$$E_\gamma + \nabla_\delta E_\gamma r_{k\delta} + \frac{1}{2}\nabla_\delta \nabla_\varepsilon E_\gamma r_{k\delta} r_{k\varepsilon} + ... \tag{B.4}$$

Note that the electric field is always evaluated at the origin of the objects, and treating each object using point multipoles simplifies this greatly.

To find the force exerted on object a by the electric field, one takes the electric field expression, and multiplies it by q_k, and then sum over all charges in a:

$$F_\gamma = \sum_{k \text{ in } a} q_k \{ E_\gamma + \nabla_\delta E_\gamma r_{k\delta} + \frac{1}{2}\nabla_\delta \nabla_\varepsilon E_\gamma r_{k\delta} r_{k\varepsilon} + ... \} \tag{B.5}$$

$$= C_a E_\gamma + D_{a\delta} \nabla_\delta E_\gamma + Q_{a\delta\varepsilon} \nabla_\delta \nabla_\varepsilon E_\gamma + ... \tag{B.6}$$

Similarly, the torque exerted by the field on a can be expressed as

$$\tau_\alpha = \sum_{k \text{ in } a} (\mathbf{r}_k \times q_k \mathbf{E})_\alpha \tag{B.7}$$

$$= \sum_{k \text{ in } a} \epsilon_{\alpha\beta\gamma} q_k r_{k\beta} E_\gamma(\mathbf{r}_k) \tag{B.8}$$

$$= \epsilon_{\alpha\beta\gamma} D_\beta E_\gamma + 2\epsilon_{\alpha\beta\gamma} Q_{\beta\delta} \nabla_\delta E_\gamma + ... \tag{B.9}$$

The last term is essentially identical with form derived by Torres del Castillo and Méndez Garrido,[?] although their derivation utilized a traceless form of the quadrupole that is different than the primitive definition in use here. We note that the Levi-Civita symbol can be eliminated by utilizing the matrix cross product in

TABLE B.1

Potential energy (U), force ($\mathbf{F}$), and torque (τ) expressions for a multipolar site embedded in an electric field with spatial variations, $\mathbf{E}(\mathbf{r})$.

	Charge	Dipole	Quadrupole
U	$C\phi(\mathbf{r})$	$-\mathbf{D} \cdot \mathbf{E}(\mathbf{r})$	$-\mathsf{Q} : \nabla\mathbf{E}(\mathbf{r})$
$\mathbf{F}$	$C\mathbf{E}(\mathbf{r})$	$+\mathbf{D} \cdot \nabla\mathbf{E}(\mathbf{r})$	$+\mathsf{Q} : \nabla\nabla\mathbf{E}(\mathbf{r})$
τ		$\mathbf{D} \times \mathbf{E}(\mathbf{r})$	$+2\mathsf{Q} \times \nabla\mathbf{E}(\mathbf{r})$

an identical form as in Ref. Smith98:

$$[\mathsf{A} \times \mathsf{B}]_\alpha = \sum_\beta [\mathsf{A}_{\alpha+1,\beta}\mathsf{B}_{\alpha+2,\beta} - \mathsf{A}_{\alpha+2,\beta}\mathsf{B}_{\alpha+1,\beta}] \tag{B.10}$$

where $\alpha + 1$ and $\alpha + 2$ are regarded as cyclic permuations of the matrix indices. In table B.1 we give compact expressions for how the multipole sites interact with an external field that has exhibits spatial variations.

B.2 Gradient of the field due to quadrupolar polarization

In this section, we will discuss the gradient of the field produced by quadrupolar polarization. For this purpose, we consider a distribution of charge $\rho(r)$ which gives rise to an electric field $\vec{E}(r)$ and gradient of the field $\vec{\nabla}\vec{E}(r)$ throughout space. The total gradient of the electric field over volume due to the all charges within the sphere of radius R is given by (cf. Jackson equation 4.14):

$$\int_{r<R} \vec{\nabla}\vec{E} \, d^3r = -\int_{r=R} R^2 \vec{E} \, \hat{n} \, d\Omega \tag{B.11}$$

where $d\Omega$ is the solid angle and $\hat{n}$ is the normal vector of the surface of the sphere which is equal to $sin[\theta]cos[\phi]\hat{x} + sin[\theta]sin[\phi]\hat{y} + cos[\theta]\hat{z}$ in spherical coordinates. For the charge density $\rho(r')$, the total gradient of the electric field can be written as (cf. Jackson equation 4.16),

$$\int_{r<R} \vec{\nabla}\vec{E} \, d^3r = -\int_{r=R} R^2 \, \vec{\nabla}\Phi \, \hat{n} \, d\Omega = -\frac{1}{4\pi \, \epsilon_o} \int_{r=R} R^2 \, \vec{\nabla} \left(\int \frac{\rho(r')}{|\vec{r} - \vec{r'}|} \, d^3r' \right) \hat{n} \, d\Omega \tag{B.12}$$

The radial function in the equation (B.12) can be expressed in terms of spherical harmonics as (cf. Jackson equation 3.70),

$$\frac{1}{|\vec{r} - \vec{r'}|} = 4\pi \sum_{l=0}^{\infty} \sum_{m=-l}^{m=l} \frac{1}{2l+1} \frac{r_<^l}{r_>^{l+1}} \, Y^*_{lm}(\theta', \phi') \, Y_{lm}(\theta, \phi) \tag{B.13}$$

127

If the sphere completely encloses the charge density then $r_< = r'$ and $r_> = R$.

Substituting equation (B.13) into (B.12) we get,

$$\int_{r<R} \vec{\nabla}\vec{E}\ d^3r = -\frac{R^2}{\epsilon_o} \int_{r=R} \vec{\nabla} \left(\int \rho(r') \sum_{l=0}^{\infty} \sum_{m=-l}^{m=l} \frac{1}{2l+1} \frac{r'^l}{R^{l+1}} Y^*_{lm}(\theta',\phi')\ Y_{lm}(\theta,\phi)\ d^3r' \right) \hat{n}\ d\Omega$$

$$= -\frac{R^2}{\epsilon_o} \sum_{l=0}^{\infty} \sum_{m=-l}^{m=l} \frac{1}{2l+1} \int \rho(r')\ r'^l\ Y^*_{lm}(\theta',\phi') \left(\int_{r=R} \vec{\nabla} \left(R^{-(l+1)}\ Y_{lm}(\theta,\phi) \right) \hat{n}\ d\Omega \right) d^3r'$$

$$\text{(B.14)}$$

The gradient of the product of radial function and spherical harmonics is given by (cf. Arfken, p.811 eq. 16.94):

$$\vec{\nabla}\left[f(r)\ Y_{lm}(\theta,\phi)\right] = -\left(\frac{l+1}{2l+1}\right)^{1/2} \left[\frac{\partial}{\partial r} - \frac{l}{r}\right] f(r)\ Y_{l,l+1,m}(\theta,\phi)$$

$$+ \left(\frac{l}{2l+1}\right)^{1/2} \left[\frac{\partial}{\partial r} + \frac{l}{r}\right] f(r)\ Y_{l,l-1,m}(\theta,\phi).$$

$$\text{(B.15)}$$

Using equation (B.15) we get,

$$\vec{\nabla}\left(R^{-(l+1)}\ Y_{lm}(\theta,\phi)\right) = [(l+1)(2l+1)]^{1/2}\ Y_{l,l+1,m}(\theta,\phi)\ \frac{1}{R^{l+2}}, \qquad \text{(B.16)}$$

where $Y_{l,l+1,m}(\theta,\phi)$ is the vector spherical harmonics which can be expressed in terms of spherical harmonics as shown in below (cf. Arfkan p.811),

$$Y_{l,l+1,m}(\theta,\phi) = \sum_{m_1,m_2} C(l+1,1,l|m_1,m_2,m)\ Y_{l+1}{}^{m_1}(\theta,\phi)\ \hat{e}_{m_2}, \qquad \text{(B.17)}$$

where $C(l+1, 1, l|m_1, m_2, m)$ is a Clebsch-Gordan coefficient and $\hat{e}_{m_2}$ is a spherical tensor of rank 1 which can be expressed in terms of Cartesian coordinates,

$$\hat{e}_{+1} = -\frac{\hat{x} + i\hat{y}}{\sqrt{2}}, \quad \hat{e}_0 = \hat{z}, \quad and \quad \hat{e}_{-1} = \frac{\hat{x} - i\hat{y}}{\sqrt{2}} \tag{B.18}$$

The normal vector $\hat{n}$ can be expressed in terms of spherical tensor of rank 1 as shown in below,

$$\hat{n} = \sqrt{\frac{4\pi}{3}} \left(-Y_1^{-1}\hat{e}_1 - Y_1^1\hat{e}_{-1} + Y_1^0\hat{e}_0 \right) \tag{B.19}$$

The surface integral of the product of $\hat{n}$ and $Y_{l+1}{}^{m_1}(\theta, \phi)$ gives,

$$
\begin{aligned}
\int \hat{n}\, Y_{l+1}{}^{m_1}\, d\Omega &= \int \sqrt{\frac{4\pi}{3}} \left(-Y_1^{-1}\hat{e}_1 - Y_1^1\hat{e}_{-1} + Y_1^0\hat{e}_0 \right) Y_{l+1}{}^{m_1}\, d\Omega \\
&= \int \sqrt{\frac{4\pi}{3}} \left(Y_1^{1*}\hat{e}_1 + Y_1^{-1*}\hat{e}_{-1} + Y_1^{0*}\hat{e}_0 \right) Y_{l+1}{}^{m_1}\, d\Omega \\
&= \sqrt{\frac{4\pi}{3}} \left(\delta_{l+1,1}\, \delta_{1,m_1}\, \hat{e}_1 + \delta_{l+1,1}\, \delta_{-1,m_1}\, \hat{e}_{-1} + \delta_{l+1,1}\, \delta_{0,m_1}\, \hat{e}_0 \right),
\end{aligned}
$$
$$\tag{B.20}$$

where $Y_l^{-m} = (-1)^m Y_l^{m*}$ and $\int Y_l^{m*} Y_{l'}{}^{m'}\, d\Omega = \delta_{ll'}\delta_{mm'}$. Non-vanishing values of equation B.20 require $l = 0$, therefore the value of $m = 0$. Since the values of m_1 are -1, 1, and 0 then m_2 takes the values 1, -1, and 0, respectively provided that $m = m_1 + m_2$. Equation B.14 can therefore be modified,

$$
\begin{aligned}
\int_{r<R} \vec{\nabla}\vec{E}\, d^3r = &-\sqrt{\frac{4\pi}{3}} \frac{1}{\epsilon_o} \int \rho(r')\, Y^*{}_{00}(\theta', \phi')[C(1,1,0|-1,1,0)\, \hat{e}_{-1}\hat{e}_1 \\
&+ C(1,1,0|-1,1,0)\, \hat{e}_1\hat{e}_{-1} + C(1,1,0|0,0,0)\, \hat{e}_0\hat{e}_0]\, d^3r'.
\end{aligned}
\tag{B.21}
$$

After substituting $Y^*{}_{00} = \frac{1}{\sqrt{4\pi}}$ and using the values of the Clebsch-Gorden coefficients: $C(1,1,0|-1,1,0) = \frac{1}{\sqrt{3}}$, $C(1,1,0|-1,1,0) = \frac{1}{\sqrt{3}}$ and $C(1,1,0|0,0,0) =$

$-\frac{1}{\sqrt{3}}$ in equation B.21 we obtain,

$$
\begin{aligned}
\int_{r<R} \vec{\nabla}\vec{E}\, d^3r &= -\sqrt{\frac{4\pi}{3}}\, \frac{1}{\epsilon_o} \int \rho(r')\, d^3r'\, (\hat{e}_{-1}\hat{e}_1 + \hat{e}_1\hat{e}_{-1} - \hat{e}_0\hat{e}_0) \\
&= -\sqrt{\frac{4\pi}{3}}\, \frac{1}{\epsilon_o}\, C_{total}\, (\hat{e}_{-1}\hat{e}_1 + \hat{e}_1\hat{e}_{-1} - \hat{e}_0\hat{e}_0)\,.
\end{aligned}
\tag{B.22}
$$

Equation (B.22) gives the total gradient of the field over a sphere due to the distribution of the charges. For quadrupolar fluids the total charge within a sphere is zero, therefore $\int_{r<R} \vec{\nabla}\vec{E}\, d^3r = 0$. Hence the quadrupolar polarization produces zero net gradient of the field inside the sphere.

B.3 Applied field or field gradient

To satisfy the condition $\nabla . E = 0$, within the box of molecules we have taken electrostatic potential in the following form

$$\phi(x, y, z) = -g_o \left(\frac{1}{2}(a_1\ b_1 - \frac{cos\psi}{3})\ x^2 + \frac{1}{2}(a_2\ b_2 - \frac{cos\psi}{3})\ y^2 + \frac{1}{2}(a_3\ b_3 - \frac{cos\psi}{3})\ z^2 \right.$$
$$\left. + \frac{(a_1\ b_2 + a_2\ b_1)}{2} x\ y + \frac{(a_1\ b_3 + a_3\ b_1)}{2} x\ z + \frac{(a_2\ b_3 + a_3\ b_2)}{2} y\ z \right),$$

$$(B.23)$$

where $a = (a_1, a_2, a_3)$ and $b = (b_1, b_2, b_3)$ are basis vectors determine coefficients in x, y, and z direction. And g_o and ψ are overall strength of the potential and angle between basis vectors respectively. The electric field derived from the above potential is,

$$\mathbf{E} = \frac{\mathbf{g_o}}{\mathbf{2}} \begin{pmatrix} 2(a_1\ b_1 - \frac{cos\psi}{3})\ x\ + (a_1\ b_2\ + a_2\ b_1)\ y + (a_1\ b_3\ + a_3\ b_1)\ z \\ (a_2\ b_1\ + a_1\ b_2)\ x + 2(a_2\ b_2\ - \frac{cos\psi}{3})\ y + (a_2\ b_3\ + a_3\ b_3)\ z \\ (a_3\ b_1\ + a_3\ b_2)\ x + (a_3\ b_2\ + a_2\ b_3)y + 2(a_3\ b_3\ - \frac{cos\psi}{3})\ z \end{pmatrix}.$$

The gradient of the applied field derived from the potential can be written in the following form,

$$\nabla \mathbf{E} = \frac{\mathbf{g_o}}{\mathbf{2}} \begin{pmatrix} 2(a_1\ b_1 - \frac{cos\psi}{3}) & (a_1\ b_2\ + a_2\ b_1) & (a_1\ b_3\ + a_3\ b_1)\ z \\ (a_2\ b_1\ + a_1\ b_2) & 2(a_2\ b_2\ - \frac{cos\psi}{3}) & (a_2\ b_3\ + a_3\ b_3)\ z \\ (a_3\ b_1\ + a_3\ b_2) & (a_3\ b_2\ + a_2\ b_3) & 2(a_3\ b_3\ - \frac{cos\psi}{3})\ z \end{pmatrix}.$$

BIBLIOGRAPHY

1. See supplementary material document no. _____ for body-frame expressions and converged energy constants.

2. D. Adams. Computer simulation of highly polar liquids: The hard sphere plus point dipole potential. *Molecular Physics*, 40(5):1261–1271, 1980. doi: 10.1080/00268978000102261.

3. D. Adams and E. Adams. Static dielectric properties of the stockmayer fluid from computer simulation. *Molecular Physics*, 42(4):907–926, 1981. doi: 10. 1080/00268978100100701.

4. D. Adu-Gyamfi. On the electric quadrupole density of an isotropic non-polar fluid. *Physica A: Statistical Mechanics and its Applications*, 93(3):553 – 558, 1978. ISSN 0378-4371. doi: http://dx.doi.org/10.1016/0378-4371(78) 90175-9. URL `http://www.sciencedirect.com/science/article/pii/0378437178901759`.

5. D. Adu-Gyamfi. On the average moments of a polar molecule in a non-uniform electric field. *Physica A: Statistical Mechanics and its Applications*, 108(1):205 – 210, 1981. ISSN 0378-4371. doi: http://dx.doi. org/10.1016/0378-4371(81)90174-6. URL `http://www.sciencedirect.com/science/article/pii/0378437181901746`.

6. A. Aguado and P. A. Madden. Ewald summation of electrostatic multipole interactions up to the quadrupolar level. *J. Chem. Phys.*, 119(14):7471–7483, 2003. doi: 10.1063/1.1605941.

7. M. P. Allen. Introduction to molecular dynamics simulation, 2004.

8. M. P. Allen and G. Germano. Expressions for forces and torques in molecular simulations using rigid bodies. 104(20-21):3225–3235, 2006. doi: 10.1080/00268970601075238. URL http://www.tandfonline.com/doi/abs/10.1080/00268970601075238.

9. M. P. Allen and D. J. Tildesley. *Computer Simulation of Liquids*. Clarendon Press, New York, NY, USA, 1989. ISBN 0-19-855645-4.

10. D. Beck, R. Armen, and V. Daggett. Cutoff size need not strongly influence molecular dynamics results for solvated polypeptides. *Biochemistry*, 44(2):609–616, 2005. ISSN 0006-2960. URL Http://Pubs3.Acs.Org/Acs/Journals/Doilookup?In_Doi=10.1021/Bi0486381.

11. Y. Chen and J. Weeks. Local molecular field theory for effective attractions between like charged objects in systems with strong coulomb interactions. 103:7560–7565, 2006. doi: DOI10.1073/pnas.0600282103.

12. Y. Chen, C. Kaur, and J. Weeks. Connecting systems with short and long ranged interactions: Local molecular field theory for ionic fluids. 108:19874–19884, 2004. doi: DOI10.1021/jp0469261.

13. S. M. Chitanvis. A continuum solvation theory of quadrupolar fluids. *The Journal of Chemical Physics*, 104(22):9065–9074, 1996. doi: http://dx.

doi.org/10.1063/1.471615. URL `http://scitation.aip.org/content/aip/journal/jcp/104/22/10.1063/1.471615`.

14. S. Chowdhuri, M.-L. Tan, and T. Ichiye. Dynamical properties of the soft sticky dipole-quadrupole-octupole water model: A molecular dynamics study. 125(14):144513–8, 2006. URL `Http://Link.Aip.Org/Link/?jcp/125/144513/1`.

15. T. Darden, D. York, and L. Pedersen. Particle mesh ewald: An nlog(n) method for ewald sums in large systems. *The Journal of Chemical Physics*, 98(12), 1993.

16. S. W. de Leeuw, J. W. Perram, and E. R. Smith. Simulation of electostatic systems in periodic boundary conditions. I. Lattice sums and dielectric constants. *Proc. R. Soc. London Ser. A*, 373(1752):27–56, 1980.

17. N. A. Denesyuk and J. D. Weeks. A new approach for efficient simulation of Coulomb interactions in ionic fluids. 128, 2008.

18. Z. Dirk, S. Bernd, and M. K. Stefan. Enhancement of the wolf damped coulomb potential: static, dynamic, and dielectric properties of liquid water from molecular simulation. *The Journal of Physical Chemistry B*, 106(41): 10725–10732, 2002. doi: 10.1021/jp025949h. URL `http://dx.doi.org/10.1021/jp025949h`.

19. A. Dullweber, B. Leimkuhler, and R. McLachlan. Symplectic splitting methods for rigid body molecular dynamics. 107(15):5840–5851, 1997.

20. N. J. English. Effect of electrostatics techniques on the estimation of thermal

conductivity via equilibrium molecular dynamics simulation: application to methane hydrate. 106:1887–1898, 2008. doi: DOI10.1080/00268970802360348.

21. R. M. Ernst, L. Wu, C.-h. Liu, S. R. Nagel, and M. E. Neubert. Quadrupolar susceptibility of complex fluids. *Phys. Rev. B*, 45:667–672, Jan 1992. doi: 10.1103/PhysRevB.45.667. URL `http://link.aps.org/doi/10.1103/PhysRevB.45.667`.

22. U. Essmann, L. Perera, M. L. Berkowitz, T. Darden, H. Lee, and L. G. Pedersen. A smooth particle mesh ewald method. *The Journal of Chemical Physics*, 103(19), 1995.

23. C. J. Fennell and J. D. Gezelter. Is the ewald summation still necessary? pairwise alternatives to the accepted standard for long-range electrostatics. *The Journal of Chemical Physics*, 124(23):234104, 2006. doi: http://dx.doi.org/10.1063/1.2206581. URL `http://scitation.aip.org/content/aip/journal/jcp/124/23/10.1063/1.2206581`.

24. K. A. Forrest, T. Pham, K. McLaughlin, J. L. Belof, A. C. Stern, M. J. Zaworotko, and B. Space. Simulation of the mechanism of gas sorption in a metal–organic framework with open metal sites: Molecular hydrogen in pcn-61. 116(29):15538–15549, 2012. doi: 10.1021/jp306084t. URL `http://dx.doi.org/10.1021/jp306084t`.

25. I. Fukuda. Zero-multipole summation method for efficiently estimating electrostatic interactions in molecular system. 139(17):174107, 2013. doi: http://dx.doi.org/10.1063/1.4827055. URL `http://scitation.aip.org/content/aip/journal/jcp/139/17/10.1063/1.4827055`.

26. I. Fukuda, Y. Yonezawa, and H. Nakamura. Molecular dynamics scheme for precise estimation of electrostatic interaction via zero-dipole summation principle. 134(16):164107, 2011. doi: http://dx.doi.org/10.1063/1.3582791. URL `http://scitation.aip.org/content/aip/journal/jcp/134/16/10.1063/1.3582791`.

27. I. Fukuda, N. Kamiya, Y. Yonezawa, and H. Nakamura. Simple and accurate scheme to compute electrostatic interaction: Zero-dipole summation technique for molecular system and application to bulk water. 137(5):054314, 2012. doi: http://dx.doi.org/10.1063/1.4739789. URL `http://scitation.aip.org/content/aip/journal/jcp/137/5/10.1063/1.4739789`.

28. J. D. Gezelter, M. Lamichhane, P. Louden, J. Michalka, S. Niedhart, T. Lin, C. F. V. II, C. J. Fennell, M. A. Meineke, S. Kuang, K. Stocker, J. Marr, X. Sun, C. Li, K. Daily, and Y. Zheng. Openmd-2.3: Molecular dynamics in the open. Available at `http://openmd.org`.

29. P. A. Golubkov and R. Ren. Generalized coarse-grained model based on point multipole and Gay-Berne potentials. 125:064103, 2006.

30. J. S. Hansen, T. B. Schroder, and J. C. Dyre. Simplistic Coulomb forces in molecular dynamics: Comparing the Wolf and shifted-force approximations. 116:5738–5743, 2012. doi: DOI10.1021/jp300750g.

31. R. W. Hockney and J. W. Eastwood. *Computer simulation using particles.* CRC Press, 1988.

32. H. W. Horn, W. C. Swope, J. W. Pitera, J. D. Madura, T. J. Dick, G. L. Hura, and T. Head-Gordon. Development of an improved four-site water

model for biomolecular simulations: TIP4P-Ew. 120(20):9665–9678, 2004. doi: 10.1063/1.1683075.

33. P. H. Hünenberger and J. A. McCammon. Ewald artifacts in computer simulations of ionic solvation and ion – ion interaction: A continuum electrostatics study. *J. Chem. Phys.*, 110(4):1856–1872, 1999.

34. P. H. Hünenberger and J. A. McCammon. Effect of artificial periodicity in simulations of biomolecules under ewald boundary conditions: a continuum electrostatics study. *Biophys. Chem.*, 78:69–88, 1999.

35. T. Ichiye and M.-L. Tan. Soft sticky dipole-quadrupole-octupole potential energy function for liquid water: An approximate moment expansion. 124(13): 134504–10, 2006. URL `Http://Link.Aip.Org/Link/?jcp/124/134504/1`.

36. R. W. Impey, P. A. Madden, and I. R. McDonald. Spectroscopic and transport properties of water: Model calculations and the interpretation of experimental results. 46(3):513–539, 1982.

37. S. Izvekov, J. M. J. Swanson, and G. A. Voth. Coarse-graining in interaction space: A systematic approach for replacing long-range electrostatics with short-range potentials. 112:4711–4724, 2008. doi: DOI10.1021/jp710339n.

38. J. D. Jackson. *Classical Electrodynamics Third Edition*. Wiley, third edition, Aug. 1998. ISBN 047130932X. URL `http://www.amazon.com/exec/obidos/redirect?tag=citeulike07-20&path=ASIN/047130932X`.

39. J. Jeon and H. J. Kim. A continuum theory of solvation in quadrupolar solvents. i. formulation. *The Journal of Chemical Physics*, 119(16):8606–8625,

2003. doi: http://dx.doi.org/10.1063/1.1605376. URL `http://scitation.aip.org/content/aip/journal/jcp/119/16/10.1063/1.1605376`.

40. J. Jeon and H. J. Kim. A continuum theory of solvation in quadrupolar solvents. ii. solvation free energetics, dynamics, and solvatochromism. *The Journal of Chemical Physics*, 119(16):8626–8635, 2003. doi: http://dx.doi.org/10.1063/1.1605377. URL `http://scitation.aip.org/content/aip/journal/jcp/119/16/10.1063/1.1605377`.

41. S. K. Kannam, B. D. Todd, J. S. Hansen, and P. J. Daivis. How fast does water flow in carbon nanotubes? 138(9):094701, 2013. doi: 10.1063/1.4793396. URL `http://link.aip.org/link/?JCP/138/094701/1`.

42. S. M. Kast, K. F. Schmidt, and B. Schilling. Integral equation theory for correcting truncation errors in molecular simulations. 367:398–404, 2003.

43. J. G. Kirkwood. The dielectric polarization of polar liquids. *The Journal of Chemical Physics*, 7(10):911–919, 1939. doi: http://dx.doi.org/10.1063/1.1750343. URL `http://scitation.aip.org/content/aip/journal/jcp/7/10/10.1063/1.1750343`.

44. M. Lamichhane, J. D. Gezelter, and K. E. Newman. Real space electrostatics for multipoles. i. development of methods. *The Journal of Chemical Physics*, 141(13):134109, 2014. doi: http://dx.doi.org/10.1063/1.4896627. URL `http://scitation.aip.org/content/aip/journal/jcp/141/13/10.1063/1.4896627`.

45. D. E. Logan. On the dielectric theory of fluids. *Molecular Physics*, 44(6):

1271–1295, 1981. doi: 10.1080/00268978100103181. URL `http://dx.doi.org/10.1080/00268978100103181`.

46. D. E. Logan. On the dielectric theory of fluids. *Molecular Physics*, 46(2): 271–285, 1982. doi: 10.1080/00268978200101251. URL `http://dx.doi.org/10.1080/00268978200101251`.

47. D. E. Logan. On the dielectric theory of fluids. *Molecular Physics*, 46(6): 1155–1194, 1982. doi: 10.1080/00268978200101871. URL `http://dx.doi.org/10.1080/00268978200101871`.

48. P. Louden, R. Schoenborn, and C. P. Lawrence. Molecular dynamics simulations of the condensation coefficient of water. *Fluid Phase Equilibria*, 349(0): 83–86, 2013. doi: http://dx.doi.org/10.1016/j.fluid.2013.04.006. URL `http://www.sciencedirect.com/science/article/pii/S037838121300174X`.

49. J. M. Luttinger and L. Tisza. Theory of dipole interaction in crystals. *Phys. Rev.*, 70:954–964, Dec 1946. doi: 10.1103/PhysRev.70.954. URL `http://link.aps.org/doi/10.1103/PhysRev.70.954`.

50. J. M. Luttinger and L. Tisza. Errata: Theory of dipole interaction in crystals [phys. rev. 70, 954 (1946)]. *Phys. Rev.*, 72:257–257, Aug 1947. doi: 10.1103/PhysRev.72.257. URL `http://link.aps.org/doi/10.1103/PhysRev.72.257`.

51. B. A. Luty and W. F. van Gunsteren. Calculating electrostatic interactions using the particle-particle particle-mesh method with nonperiodic long-range interactions. *J. Phys. Chem.*, 100(7):2581–2587, 1996.

52. B. A. Luty, M. E. Davis, I. G. Tironi, and W. F. V. Gunsteren. A comparison of particle-particle, particle-mesh and ewald methods for calculating electrostatic interactions in periodic molecular systems. *Molecular Simulation*, 14(1):11–20, 1994. doi: 10.1080/08927029408022004. URL `http://dx.doi.org/10.1080/08927029408022004`.

53. B. A. Luty, I. G. Tironi, and W. F. van Gunsteren. Latticesum methods for calculating electrostatic interactions in molecular simulations. *The Journal of Chemical Physics*, 103(8), 1995.

54. Y. Ma and S. H. Garofalini. Modified wolf electrostatic summation: Incorporating an empirical charge overlap. *Mol. Simul.*, 31(11):739–748, 2005.

55. M.Born and T. V. Karman. *Physik*, Z(13):297, 1912.

56. B. W. McCann and O. Acevedo. Pairwise alternatives to Ewald summation for calculating long-range electrostatics in ionic liquids. 9:944–950, 2013. doi: DOI10.1021/ct300961e.

57. N. Metropolis, A. W. Rosenbluth, M. N. Rosenbluth, A. H. Teller, and E. Teller. Equation of state calculations by fast computing machines. *The Journal of Chemical Physics*, 21(6), 1953.

58. O. Nagai and T. Nakamura. Quadrupole interaction in crystals. *Progress of Theoretical Physics*, 24(2):432–454, 1960. doi: 10.1143/PTP.24.432. URL `http://ptp.oxfordjournals.org/content/24/2/432.abstract`.

59. O. Nagai and T. Nakamura. Quadrupole interaction in crystals. *Progress of Theoretical Physics*, 30(3):412, 1963. doi: 10.1143/PTP.30.412a. URL `http://ptp.oxfordjournals.org/content/30/3/412.1.short`.

60. M. Neumann. Dipole moment fluctuation formulas in computer simulations of polar systems. *Molecular Physics*, 50(4):841–858, 1983. doi: 10.1080/00268978300102721.

61. M. Neumann. The dielectric constant of water. Computer simulations with the MCY potential. 82(12):5663–5672, 1985.

62. M. Neumann and O. Steinhauser. On the calculation of the dielectric constant using the ewald-kornfeld tensor. *Chemical Physics Letters*, 95(4–5):417 – 422, 1983. ISSN 0009-2614. doi: http://dx.doi.org/10.1016/0009-2614(83)80585-5.

63. M. Neumann, O. Steinhauser, and G. S. Pawley. Consistent calculation of the static and frequency-dependent dielectric constant in computer simulations. 52(1):97–113, 1984.

64. L. Onsager. Electric moments of molecules in liquids. *Journal of the American Chemical Society*, 58(8):1486–1493, 1936. doi: 10.1021/ja01299a050. URL http://dx.doi.org/10.1021/ja01299a050.

65. M. Orsi and J. W. Essex. The ELBA Force Field for Coarse-Grain Modeling of Lipid Membranes. *PLOS ONE*, 6(12):e28637, 2011. ISSN 1932-6203.

66. M. Orsi, J. Michel, and J. W. Essex. Coarse-grain modelling of DMPC and DOPC lipid bilayers. *J. Phys. - Cond. Matt.*, 22(15):155106, 2010. ISSN 0953-8984.

67. J. W. Perram, H. G. Petersen, and S. W. D. Leeuw. An algorithm for the simulation of condensed matter which grows as the 3/2 power of the number of particles. *Molecular Physics*, 65(4):875–893, 1988.

141

doi: 10.1080/00268978800101471. URL `http://dx.doi.org/10.1080/00268978800101471`.

68. J. W. Ponder, C. Wu, P. Ren, V. S. Pande, J. D. Chodera, M. J. Schnieders, I. Haque, D. L. Mobley, D. S. Lambrecht, R. A. DiStasio, Jr, M. Head-Gordon, G. N. I. Clark, M. E. Johnson, and T. Head-Gordon. Current status of the AMOEBA polarizable force field. 114(8):2549–64, 2010. doi: 10.1021/jp910674d.

69. S. Price, A. Stone, and M. Alderton. Explicit formulae for the electrostatic energy, forces and torques between a pair of molecules of arbitrary symmetry. 52(4):987–1001, 1984. doi: 10.1080/00268978400101721. URL `http://www.tandfonline.com/doi/abs/10.1080/00268978400101721`.

70. G. Rajagopal and R. Needs. An optimized ewald method for long-ranged potentials. *Journal of Computational Physics*, 115(2):399 – 405, 1994. ISSN 0021-9991. doi: http://dx.doi.org/10.1006/jcph.1994.1205. URL `http://www.sciencedirect.com/science/article/pii/S0021999184712058`.

71. P. Ren, C. Wu, and J. W. Ponder. Polarizable atomic multipole-based molecular mechanics for organic molecules. 7(10):3143–3161, 2011. doi: 10.1021/ct200304d.

72. J. E. Roberts and J. Schnitker. How the unit cell surface charge distriubution affects the energetics of ion-solvent interactions in simulations. *J. Chem. Phys.*, 101(6):5024–5031, 1994.

73. J. E. Roberts and J. Schnitker. Boundary conditions in sumulations of aqueous ionic solutions: A systematic study. *J. Phys. Chem.*, 99:1322–1331, 1995.

74. J. M. Rodgers, C. Kaur, Y.-G. Chen, and J. D. Weeks. Attraction between like-charged walls: Short-ranged simulations using local molecular field theory. *Phys. Rev. Lett.*, 97:097801, Aug 2006. doi: 10.1103/PhysRevLett.97.097801. URL `http://link.aps.org/doi/10.1103/PhysRevLett.97.097801`.

75. Z. A. Rycerz and P. W. M. Jacobs. Ewald summation in the molecular dynamics simulation of large ionic systems. *Molecular Simulation*, 8(3-5):197–213, 1992. doi: 10.1080/08927029208022476. URL `http://dx.doi.org/10.1080/08927029208022476`.

76. J. A. Sauer. Magnetic energy constants of dipolar lattices. *Phys. Rev.*, 57: 142–146, 1940. doi: 10.1103/PhysRev.57.142. URL `http://link.aps.org/doi/10.1103/PhysRev.57.142`.

77. M. J. Schnieders, N. A. Baker, P. Ren, and J. W. Ponder. Polarizable atomic multipole solutes in a poisson-boltzmann continuum. 126(12):124114, 2007. doi: 10.1063/1.2714528. URL `http://link.aip.org/link/?JCP/126/124114/1`.

78. W. Shi and D. R. Luebke. Enhanced gas absorption in the ionic liquid 1-n-hexyl-3-methylimidazolium bis(trifluoromethylsulfonyl)amide ([hmim][Tf2N]) confined in silica slit pores: A molecular simulation study. *Langmuir*, 29(18): 5563–5572, 2013. doi: 10.1021/la400226g.

79. J. Shimada, H. Kaneko, and T. Takada. Efficient calculations of coulombic interactions in biomolecular simulations with periodic boundary conditions. *Journal of Computational Chemistry*, 14(7):867–878, 1993. ISSN 1096-987X. doi: 10.1002/jcc.540140712. URL `http://dx.doi.org/10.1002/jcc.540140712`.

80. R. I. Slavchov. Quadrupole terms in the maxwell equations: Debye-hckel theory in quadrupolarizable solvent and self-salting-out of electrolytes. *The Journal of Chemical Physics*, 140(16):164510, 2014. doi: http://dx.doi.org/10.1063/1.4871661. URL `http://scitation.aip.org/content/aip/journal/jcp/140/16/10.1063/1.4871661`.

81. R. I. Slavchov and T. I. Ivanov. Quadrupole terms in the maxwell equations: Born energy, partial molar volume, and entropy of ions. *The Journal of Chemical Physics*, 140(7):074503, 2014. doi: http://dx.doi.org/10.1063/1.4865878. URL `http://scitation.aip.org/content/aip/journal/jcp/140/7/10.1063/1.4865878`.

82. W. Smith. Point multipoles in the Ewald summation. *CCP5 Information Quarterly*, 4:13–25, 1982.

83. W. Smith. Point multipoles in the Ewald summation (revisited). *CCP5 Information Quarterly*, 46:18–30, 1998.

84. H. A. Stern and S. E. Feller. Calculation of the dielectric permittivity profile for a nonuniform system: Application to a lipid bilayer simulation. *The Journal of Chemical Physics*, 118(7):3401–3412, 2003. doi: http://dx.doi.org/10.1063/1.1537244. URL `http://scitation.aip.org/content/aip/journal/jcp/118/7/10.1063/1.1537244`.

85. H. A. Stern and S. E. Feller. Calculation of the dielectric permittivity profile for a nonuniform system: Application to a lipid bilayer simulation. *The Journal of Chemical Physics*, 118(7):3401–3412, 2003. doi: http://dx.doi.org/10.1063/1.1537244. URL `http://scitation.aip.org/content/aip/journal/jcp/118/7/10.1063/1.1537244`.

86. J. A. Te and T. Ichiye. Understanding structural effects of multipole moments on aqueous solvation of ions using the soft-sticky dipole-quadrupole-octupole water model. 499(4-6):219–225, 2010. ISSN 0009-2614. doi: 10.1016/j.cplett. 2010.09.043.

87. J. A. Te and T. Ichiye. Temperature and pressure dependence of the optimized soft-sticky dipole-quadrupole-octupole water model. 132(11):114511, 2010. ISSN 0021-9606. doi: 10.1063/1.3359432.

88. J. A. Te, M.-L. Tan, and T. Ichiye. Solvation of glucose, trehalose, and sucrose by the soft-sticky dipole-quadrupole-octupole water model. 491(4-6):218–223, 2010. ISSN 0009-2614. doi: 10.1016/j.cplett.2010.04.020.

89. T. Tokumasu, M.-H. Meurisse, N. Fillot, and P. Vergne. A molecular dynamics study of a nanoscale liquid bridge under shear. *Tribology International*, 59: 10–16, 2013. doi: DOI10.1016/j.triboint.2012.08.009.

90. A. Y. Toukmaji and J. A. B. Jr. Ewald summation techniques in perspective: a survey. *Computer Physics Communications*, 95(23):73 – 92, 1996. ISSN 0010-4655. doi: http://dx.doi.org/10.1016/0010-4655(96)00016-1. URL `http://www.sciencedirect.com/science/article/pii/0010465596000161`.

91. D. Trzesniak, A.-P. E. Kunz, and W. F. van Gunsteren. A comparison of methods to compute the potential of mean force. *ChemPhysChem*, 8(1):162–169, 2007. ISSN 1439-7641. doi: 10.1002/cphc.200600527. URL `http://dx.doi.org/10.1002/cphc.200600527`.

92. W. Weber, P. H. Hünenberger, and J. A. McCammon. Molecular dynamics simulations of a polyalanine octapeptide under ewald boundary conditions:

Influence of artificial periodicity on peptide conformation. *J. Phys. Chem. B*, 104(15):3668–3675, 2000. doi: 10.1021/jp9937757. URL `http://dx.doi.org/10.1021/jp9937757`.

93. D. Wolf. Reconstruction of nacl surfaces from a dipolar solution to the madelung problem. 68(22):3315–3318, 1992.

94. D. Wolf. Simulation of ionic surfaces from an absolutely convergent solution of the madelung problem. In D. Landau, K. Mon, and H.-B. Schüttler, editors, *Computer Simulation Studies in Condensed-Matter Physics VIII*, volume 80 of *Springer Proceedings in Physics*, pages 57–68. Springer Berlin Heidelberg, 1995. ISBN 978-3-642-79993-8. doi: 10.1007/978-3-642-79991-4_6. URL `http://dx.doi.org/10.1007/978-3-642-79991-4_6`.

95. D. Wolf, P. Keblinski, S. R. Phillpot, and J. Eggebrecht. Exact method for the simulation of coulombic systems by spherically truncated, pairwise r1 summation. *The Journal of Chemical Physics*, 110(17), 1999.

96. X. Wu and B. R. Brooks. Isotropic periodic sum: A method for the calculation of long-range interactions. 122(4):044107, 2005. doi: 10.1063/1.1836733. URL `Http://Link.Aip.Org/Link/?jcp/122/044107/1`.